Optical clearing and deep-tissue fluorescence imaging using fructose

Meng-Tsen Ke

Table of contents

Abstract

Three-dimensional fluorescence imaging is important for a comprehensive and quantitative understanding of neuronal circuitry in the brain. However, intrinsic opacity and inhomogeneity of the refractive index in most tissues have prevented the effective light penetration and emission that is necessary for high-resolution optical imaging. Optical clearing methods have been proposed to reduce the sample opacity. However, problems like fluorescent protein quenching, sample expansion/shrinkage, long operation time, and loss of detailed morphology are often encountered when using existing methods. Therefore, a fluorescent protein-friendly, speedy, and morphology-preserving optical clearing strategy has been desired for studying brain-wide neuronal circuitry.

This thesis describes a novel tissue optical clearing agent named SeeDB, which is a high refractive index aqueous optical clearing agent composed of fructose and thiol. SeeDB method was compared with previous optical clearing methods and gave a full description of how it changed the optical properties of the biological sample. Combined with two-photon microscopy and a customized objective lens with a long working distance, SeeDB allows for the imaging of the adult mouse brain through the dorsal to the ventral surface. SeeDB was also used to describe the near-complete wiring diagram of 'sister' mitral cells associated with a common glomerulus in the mouse olfactory bulb. Diverse dendritic wiring patterns among sister mitral cells provide an anatomical basis for non-redundant odor coding by these neurons.

Clearing and imaging techniques that preserve tissue architecture integrity enables three-dimensional description of the brain during development or in pathology. Furthermore, with versatile genetic tools and high-resolution imaging, SeeDB can contribute to not only long-range, but also local circuitry and facilitate the studies in brain anatomy.

1. Introduction

1.1. Optical imaging

Light microscopy is an advantageous strategy to investigate biological samples because it provides a non-invasive approach to scan through the sample with depth-resolved images. Compared with other imaging methods, such as Computed Tomography (CT) and magnetic resonance imaging (MRI), light microscopy provides higher resolution and contrast for cellular and subcellular information [1,2,3,4,5]. However, due to the thickness and the volume of biological samples, it has been difficult and challenging to use traditional light microscopy methods to get a three-dimensional picture from an intact sample. The major challenges in tissue imaging is light scattering, because biological samples are complex and composed of highly heterogeneous materials [2,3]. Light scattering is the deflection of a light beam from its original direction, which causes the light rays to miss the focus and reduce signals (**Figure 1**) [6]. As described in Rayleigh theory, the intensity of scattering is directly dependent on the size of particles encountered in the light path and the average distance between scatting events. The main feature of Rayleigh scattering is its wavelength dependency. For small objects, it varies with the inverse fourth power of the wavelength of the illuminating light [7,8]. In the conventional optical imaging technique, such as confocal microscopy, which depends on one photon absorption process, imaging depth of tissues is limited to the very superficial region (under 100 μm). Using near-infrared wavelength range (700 to 1000 nm), two-photon excited fluorescence laser scanning microscopy (2PLSM) can penetrate deeper into scattering tissue because scattering decrease as wavelength goes longer. For this reason, scattering and out-of-focus absorption are smaller in the two-photon excitation process [2,3,5].

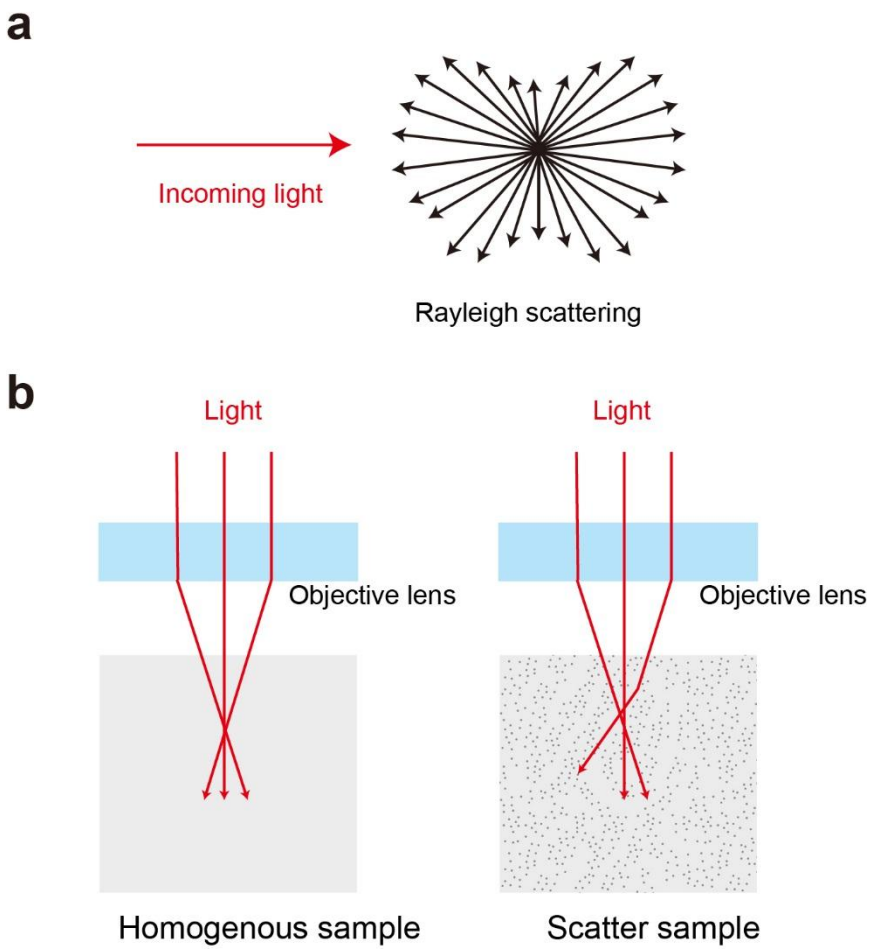

Figure 1. Illustrations for light scattering (**a**) Rayleigh scattering of incident light off a particle. (**b**) Light scattering in tissue imaging. In transparent samples as illustrated in the left panel, all the light from the source reaches the correct focal plane, therefore generates clear images with strong contrast. In biological samples, scattering arises due to the mismatch at the boundary of two distinct structures, e.g. between cell membrane and cytoplasm. Even with small angles, light eventually fails to converge on the correct focal plane and generate out-of-focus emissions. Such out-of-focus signals decrease the signal-to-noise ratio and degrades image quality.

1.2. Light scattering in tissue

Except for some special organisms, such as jellyfish and larval zebra fish, biological samples are opaque. Sample opacity is caused by both light absorption and scattering. For most biological tissue, absorption of light is smaller compared to scattering [8], because absorption in biological samples arises primarily from hemoglobin and melanin. Scattering in tissue is caused by inhomogeneities in refractive index, for instance, the refractive index mismatch at the boundary of cell membrane and cytoplasm. The refractive index of nucleus and other organelles in living cells fall on a range of 1.38-1.41, however, that of the cytoplasm is usually in the range 1.35-1.37 (**Table 1**). Scattering of light is especially problematic when imaging tissues of more than several hundred microns thick because the intensity of unscattered photon reaching to the focal plane decrease exponentially with depth [9]. Even with two-photon microscopy, the maximum imaging depth is limited around 300 μm in fixed tissue. In order to reduce the dominant factor affecting light propagation, the sample being imaged must be highly transparent and homogenous. One of possible solutions is reducing the light scattering in tissues to improve image quality and depth.

1.3. Mechanisms of tissue optical clearing

Tissue optical clearing permits delivery of light deep into the tissue and improves the capabilities of light-based examination, because scattering of light in tissue can be reduced by controlling tissue optical properties. Numerous techniques have been developed for the reduction of refractive index (RI) mismatch. Main strategies are tissue maceration and refractive index matching **(Figure 2**). In the former, tissue maceration uses chemicals such as potassium hydroxide or trypsin [10,11] to reduce scatters. As a result, optical clearing often brings out tissue damages. In the latter, the

Table 1. Refractive index (RI) of different tissues and cellular compartments [7,12,13,14].

Tissue type/ Cell region	Mean RI
Mouse brain slice (fixed)	1.37
Rat brain slice (fixed)	1.36
Rat brain slice (unfixed)	1.37
Human brain slice (fixed)	1.36
Whole-blood	1.38
Red blood cell	1.62
Blood plasma	1.34
Nucleus	1.39
Mitochondria	1.40
Cell membrane (lipid bilayer)	1.39 -1.47
Cytoplasm	1.37
Lipids	1.48

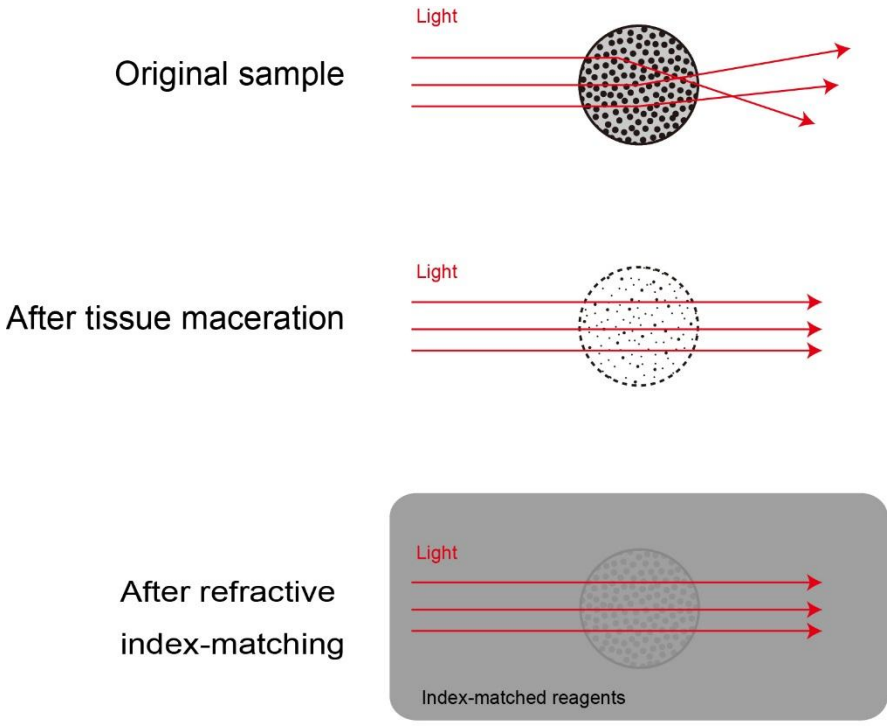

Figure 2. Illustrations for main strategies of optical clearing. Biological samples contain strong scatters such as lipids and nuclei, when the light transmits through the sample, deflection occurs where the reflective index mismatches, thus the light is dispersed. By removing scatters (e.g. lipids) inside the cells, light scattering can be reduced. Alternatively, index-matching can have similar effect of optical clearing by simply immersing the sample in to high reflective index solutions. After refractive index-matching, the refractive index is the same for the object and the surrounding media, and light passes through the object without scattering and diffraction.

basic idea for refractive index matching is the replacement of interstitial or intracellular fluid with a chemical reagent that matches scatters in tissue [15,16]. After optical clearing, samples are left intact. Compared with tissue maceration, refractive index matching provides a gentler and less damaging approach for optical clearing.

1.4. Current optical clearing methods

After the idea of optical clearing is proposed, over 100 years ago, several groups have been developing the optical clearing reagent for biological applications. Optical clearing agents with high refractive index (**Table 2**) are attempting to penetrate into the inter- and intra-cellular spaces to match the refractive index of the scatter (e.g., lipids, nucleus) and surrounding media.

1.4.1. Organic solvent-based optical clearing agents

High-index solvents, such as BABB (Murray's clear; a 2:1 mixture of benzyl alcohol and benzyl benzoate; RI = 1.56), methyl salicylate (RI = 1.52) have previously been used as clearing agent after antibody staining. Methyl salicyate has been used for mounting paraffin sections for years to increase the maximal depth of image acquisition. The most commonly used solvent-based optical clearing method is BABB, which is a 1:2 or 1:1 mixture of benzyl alcohol and benzyl benzoate [17]. By changing the ratio of the two benzoic component, the RI can be adjusted between 1.53 and 1.57. However, these organic solvents with benzene ring are insoluble in water thus can only be applied after careful tissue dehydration. After incubating with ethanol and hexane, there is a noticeable decline in fluorescent proteins [18]. Although less damaging clearing method has been developed with tetrahydrofuran (dehydration agent) and dibenzyl ether (index-matching agent; RI = 1.56), organic-solvent based techniques still have limitations such as short half-life of fluorescent proteins and noticeable morphological changes in tissues.

Table 2. Refractive indices (RI) of various solutions. Mounting media and most optical clearing agents are high refractive index agents. However, Sca*l*e method uses urea to remove the lipid membranes, the dominant scatters in the tissue, rather homogenize it with high RI agent. Although the refractive index is an important parameter, a high-index solution does not necessarily clear the tissue samples.

Reagent	**RI**
Water	1.337
Sca*l*eB4	1.379
Sca*l*eU2	1.382
Sca*l*eA2	1.383
ProLong Gold (Invitrogen)	1.398
60% (w/v) sucrose	1.425
SlowFade Gold (Invitrogen)	1.429
FocusClear (CelExplorer Labs)	1.460
100% glycerol	1.475
80% (v/v) 2,2'-thiodiethanol (TDE)	1.484
SeeDB (80.2 % w/w, 115% w/v fructose)	1.490
SeeDB37 (84.4 % w/w, 130% w/v fructose)	1.502
BABB	1.542
Saturated ZnI_2	1.620

1.4.2. Water-based optical clearing agents

Besides solvent-based optical clearing solutions, some water-based reagent with high refractive index can also be used for mounting and clearing, such as sucrose solution, FocusClear (RI = 1.46), glycerol (RI = 1.47), and 2,2'-thiodiethanol (TDE, RI = 1.52).

FocusClear is a commercially available clearing agent with non-toxic aqueous composition. Because of the limited penetration rate of FocusClear, it is often used in slices and small invertebrate brain samples and allows the visualization of the tissue down to 350 μm under confocal microscopy [19,20,21]. Although FocusClear does not require dehydration, the incubation makes the tissue shrink ~20% per dimension in mouse brain sections [22]. Sugars are also reported for optical clearing [23,24,25]. 60% w/v sucrose solution (RI = 1.425) has been used for optical clearing of thick brain tissues [26]. Although the blood vessel patterns are imaged down to 1.2 mm in depth, 60% sucrose treatment allows only modest transparency to mouse brain samples [27]. Glycerol is often used as mounting media for microscopy by embedding the sections in glycerol-PBS mixture (50-90% glycerol) for preservation and allows visualization of the slice for 100-150 μm in depth. For optical clearing, glycerol has been reported to be an effective component for *in vivo* skin optical clearing by dermal injection [28]. TDE is a water soluble reagent with high refractive index. By mixing in different ration with water, the refractive index can be ranging from 1.33 (0% TDE) to 1.52 (100% TDE) to adjust the average refractive index inside the sample [29]. Due to low penetration rate, these water-based optical clearing agents are generally limited to small samples or thin slices with a imaging depth of 500-1000 μm, which is not enough for generating complete three-dimensional neuronal map of whole mouse brain.

1.4.3. Other scatter removal techniques

Recently, two new optical clearing methods were reported for large-scale neuronal imaging, which are based on the combination of tissue maceration and index matching.

A novel optical clearing agent named Sca*l*e was reported (RI=1.38), which uses urea and detergent to render brain samples to make them transparent. Because fluorescent proteins are stable in the urea solution, Sca*l*e method is able to image fluorescent proteins deep inside the tissues at millimeter scale [27]. However, sca*l*e method requires a long incubation time for clearing and leads to tissue deformations. In addition, a large expansion in sample volume compromises the detailed cellular morphology as well as the imaging depth. In many situations where the working distance of an objective lens is a limiting factor, sample expansion hampers deep-tissue imaging with extended depth. Furthermore, because urea causes partial denaturation of cellular proteins, the Sca*l*e-treated samples are very fragile and difficult to handle.

More recently, an optical clearing technique CLARITY is reported [30,31]. CLARITY creates a stable tissue-hydrogel hybrid that stand to subsequent removal of lipids and exogenous scatters within the tissue. Scatters are solubilized with ionic detergents and then actively transported out of the tissue by electrophoresis. The strategy is powerful and advantageous for antibody staining of thick samples because the penetration barrier (e.g., lipids) is removed from the tissue. However, CLARITY requires complicated procedures and long operation time (2 weeks). Custom built set-ups (the electrophoretic tissue clearing chamber) and fine adjustments in electrophoresis conditions are laborious and difficult.

1.5. Scope of this thesis

The quenching obstacles in organic solvent-based agent and the long operation time problems in water-based agents brought the idea of seeking a simple and quick optical clearing method for fluorescently-labeled samples. In this thesis, I present a study to establish and evaluate a novel optical clearing reagent named SeeDB and compare its effectiveness with current methods. With this new technique, I relieve the limitations reported in previous methods, including imaging depth, incubation time, sample fragility, and quenching of fluorescent proteins. Combined with two-photon microscopy, SeeDB allowed us to image fixed mouse brains at the millimeter-scale level. We also used SeeDB to describe the detailed wiring diagram of mitral cells associated with a common glomerulus in the olfactory bulb. The protocol for SeeDB is quick, easy, inexpensive, and safe, and requires no special equipment; the compatibility of SeeDB with fluorescent proteins and various neuronal tracers in fixed tissues is advantageous for comprehensive and quantitative analyses of neuronal circuitry. SeeDB could be a useful tool for a broad range of studies in neuroscience and developmental biology.

2. Materials and Methods

2.1. Optical clearing

2.1.1. Optical Clearing using SeeDB

SeeDB protocol is only applied to fixed samples. When the samples were fragile or specific imaging orientation was desired in imaging, samples were first embedded into 1% or 2% agarose in PBS (**Figure 3a**) and then trimmed out excess portion of gel (**Figure 3b**, **3c**). For effective delivery, samples were soaked in 50 ml conical tube containing 20-30 mL of clearing solution and settled on an overhead tube rotator (~4 rpm, for whole-mount samples, **Figure 3e**) or on a seesaw shaker (~17 rpm, for slices, **Figure 3f**). All of the SeeDB variants started with 20% (w/v) fructose solution, and gradually changed to 40% 60%, 80%, 100% and finally in SeeDB (80.2% w/w, 115% w/v) or SeeDB37 (84.4% w/w, 130% w/v). Every fructose solutions contained 0.5% α-thioglycerol to inhibit Maillard reaction. Samples could be stored in SeeDB (at 25°C) or SeeDB37 (at 37°C) for up to one week.

2.1.1.1. SeeDB

All of the clearing solutions were prepared in 50 ml conical tubes freshly, and stored at room temperature (25°C). Samples were serially incubated in 20-30 mL of 20%, 40%, and 60% (w/v; dissolved in distilled water) fructose, each step for 8 hours (± 4 hours). Samples were then moved to 80% and 100% (w/v; dissolved in distilled water) fructose each step for 12 hours (± 6 hours). Finally samples were incubated in SeeDB (80.2% w/w, 115% w/v fructose, mixing 20.25g fructose with 5 ml distilled water to prepare ~18 ml solution) for 24 hours and kept in SeeDB until imaging. Above steps were carried out with rotation (~4 rpm, for whole-mount samples) or on a seesaw shaker (~17 rpm, for slices) at room temperature (25°C).

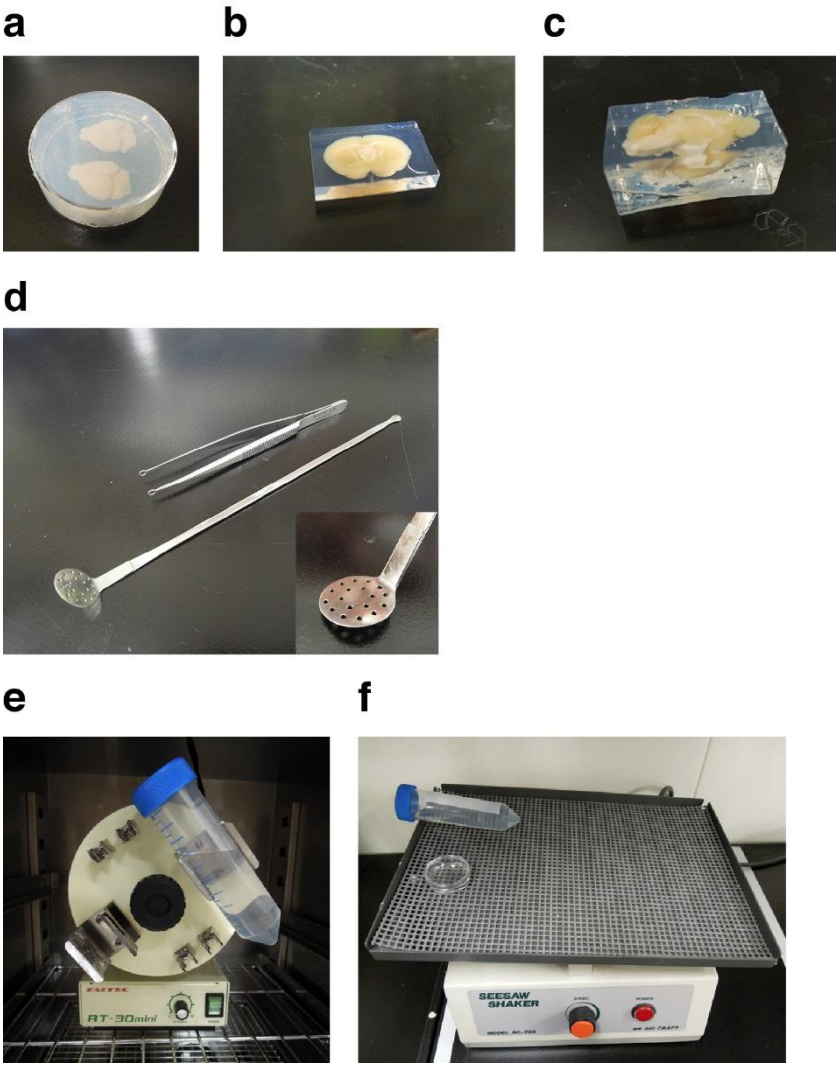

Figure 3. Tools and instruments for SeeDB method. (**a**) Brain samples embedded in 1% agarose gel. (**b**, **c**) For efficient penetration of SeeDB, it is important to trim away extra portion or slice to minimize sample size before clearing. (**d**) Moria perforated spoon (15 mm head) and ring forceps (3 mm head) for handling whole-mount brain samples. (**e**) An overhead rotator, used for whole-mount samples clearing in conical tubes. (**f**) A seesaw shaker, used for sliced and fragile samples clearing in conical tubes or in Patri dishes.

2.1.1.2. SeeDB37

SeeDB37 protocol is an extension of standard SeeDB protocol. In SeeDB37 (84.4 w/w, 130% w/v fructose) the refractive index of the media is 1.502 at 37°C. This is useful for more aged or myelinated samples. For adult mouse brains, SeeDB37 protocol was more effective to improve the transparency.

All of the clearing solutions were prepared in 50 ml conical tubes freshly, and all solutions except SeeDB37 were stored at room temperature. SeeDB37 should be stored at 37°C incubator to prevent fructose precipitation. Fixed samples were serially incubated in 20-30 mL of 20%, 40%, and 60% (w/v; dissolved in distilled water) fructose, each for 8 hours (± 4 hours). Samples were then moved to 80% and 100% (w/v; dissolved in distilled water) fructose each step for 12 hours (± 6 hours). And then incubated in SeeDB (80.2% w/w, 115% w/v fructose; mixing 20.25g fructose with 5 ml distilled water to prepare ~18 ml solution) for 24 (± 12 hours) hours. Finally, samples were moved to SeeDB37 (84.4% w/w, 130% w/v fructose; mixing 27g fructose with 5 ml distilled water to prepare ~ 20 ml solution) and kept in SeeDB37 at 37°C until imaging. All the steps before SeeDB37 were the same as standard SeeDB protocol and carried out with a rotation (~4 rpm, for whole-mount samples) at room temperature (25°C). After moving to SeeDB37, all the tools including rotator were shifted to 37°C incubator.

2.1.1.3. SeeDB37ht

SeeDB37ht protocol is designed for large and/or lipid-rich samples. The most important part of SeeDB optical clearing is to equibriate the sample gradually with the concentrated fructose solutions. However, highly concentrated fructose solutions are extremely viscous. In order to improve the penetration of fructose into the sample, the incubation temperature was increased to 50°C in this protocol. Fixed samples were serially incubated in 20-30 mL of 20%, 40%, 60%, and 80% (w/v; dissolved in

distilled water) fructose, each for 2-4 hours at 50°C. Samples were then moved 100% (w/v; dissolved in distilled water) fructose for 12 hours (± 6 hours) at 50°C. And then incubated in SeeDB (80.2% w/w, 115% w/v fructose; mixing 20.25g fructose with 5 ml distilled water to prepare ~18 ml solution) for 24 hours (± 12 hours) at 50°C. Finally, samples were moved to SeeDB37 (84.4% w/w, 130 w/v fructose; mixing 27g fructose with 5 ml distilled water to prepare ~ 20 ml solution) for 24 hours (± 12 hours) at 50°C, and then kept in SeeDB37 at 37°C until imaging. All the steps were carried out with a rotation (~4 rpm, for whole-mount samples) at 50°C. Although penetration efficiency is improved, some fluorescent proteins are partially quenched and the sample subjects to mild expansions.

2.1.1.4. SeeDBp

SeeDBp is a modified protocol for samples that show enlargements in standard SeeDB protocol, such as neonatal brains. In SeeDBp, the inclusion of 0.1× PBS minimizes sample expansions during optical clearing. Agarose embedding is preferred for protecting neonatal brain samples.

Fixed samples were serially incubated in 20-30 mL of 20%, 40%, and 60% (w/v; dissolved in 0.1× PBS) fructose, each step for 8 hours (± 4 hours). Samples were then moved to 80% (w/v; dissolved in 0.1× PBS) and 100% (w/v; dissolved in distilled water) fructose for 12 hours (± 6 hours) in each step. Finally, samples were incubated in SeeDB (80.2% w/w, 115% w/v fructose; mixing 20.25g fructose with 5 ml distilled water to prepare ~18 ml solution) for 24 hours and kept in SeeDB until imaging. All the steps above were carried out with a rotator (~4 rpm, for whole-mount samples) or a seesaw shaker (~17 rpm, for slices) at room temperature (25°C).

2.1.2. Optical clearing with Sca*l*eA2 and Sca*l*eU2 [27]

Fixed samples were transferred to an excess volume of Sca*l*eA2 (4 M urea, 10% w/v glycerol, and 0.1% Triton X-100) or Sca*l*eU2 (4M urea, 30% w/v glycerol, and

0.1% Triton X-100) and incubated at room temperature with gentle shaking for 21 days.

2.1.3 .Optical clearing with sucrose [26]

Fixed samples were incubated in 2% (v/v) Triton X-100 in PBS for 24 hours. Samples were then serially incubated in 15%, 30%, 45%, and 60% sucrose in 2% Triton X-100-PBS.

2.1.4. Optical clearing with BABB [17]

Fixed samples were serially incubated in 50%, 80%, and 100% ethanol, each for 8 hours. Next, they were incubated in 100% ethanol for 12 hours, and further placed in Hexane for 12 hours. Finally, the samples were incubated in BABB solution (Benzyl Alcohol : Benzyl Benzoate = 1 : 2) with gentle shaking for 24 hours.

2.1.5. Optical clearing with dibenzyl ether [32]

Fixed samples were serially incubated in 50%, 80%, and 100% tetrahydrofuran, each for 8 hours. This was followed by two 12-hour incubations in 100% tetrahydrofuran. Samples were then cleared in dibenzyl ether with gentle shaking for 24 hours.

2.2. Light microscopy

2.2.1. Point-spread-function analysis [33]

Fluorescent microspheres (Yellow-green fluorescent FluoSpheres, diameter = 0.5 μm, Invitrogen) were embedded in 1% agarose and the agarose block was equilibrated in SeeDB as described above. Two-photon xyz images of fluorescent beads at different depths were acquired at 920 nm excitation, as above. Gaussian fitting was used to obtain the full width at half-maximum values for x and z axes.

2.2.2. Confocal imaging using an inverted microscope

The cleared brain was dipped in a hand-made glass-bottomed chamber filled with SeeDB, Sca*l*eA2, BABB, or dibenzyl ether. Confocal images were taken with an inverted confocal microscope (Olympus, FV1000 built on IX81). Images were taken with 4× (Olympus, UPLSAPO 4X, NA = 0.16, WD = 13 mm), 10× (Olympus, UPLSAPO10X2, NA = 0.40, WD = 3.1 mm), or 20× (Olympus, UPLSAPO20X, NA=0.75, WD = 0.6 mm) objectives. A He-Ne laser (633 nm) was used for visualizing AlexaFluor 647-dextran. EYFP was visualized with an Ar laser (488 nm). AlexaFluor 647 and DAPI were visualized with a He-Ne laser (633 nm) and an LD405 nm laser, respectively.

2.2.3. Two-photon imaging using an upright microscope

For imaging agarose-embedded SeeDB-cleared brain samples, the agarose block was trimmed and the sample was placed on a Petri dish. Non-embedded samples were placed in a hand-made chamber with SeeDB. A coverslip or a custom-made glass-bottomed Petri dish was placed on top of it, and H_2O (for UMPLFLN 10XW and XLPL25XWMP), 34% glycerol (plus H_2O, v/v, refractive index = 1.38; for XLPN25XSVMP), 80% 2,2'-thiodiethanol (plus H_2O, v/v, refractive index = 1.48, for a 25× customized objective lens), or 90% 2,2'-thiodiethanol (for imaging SeeDB37-cleared samples with the customized objective lens) were used for immersion. SeeDB should was not suitable for immersion; its viscosity caused an uneven refraction index distribution due to evaporation of water from the surface of SeeDB during imaging and can impair image quality. Samples cleared with SeeDB37 were incubated at 37°C during imaging. For imaging Sca*l*eA2-treated samples, the samples were placed on the bottom of a plastic dish in 0.3% agarose, and Sca*l*eA2 was used for immersion. An upright multiphoton microscope (Olympus, FV1000MPE) was used for two-photon imaging. A 10× objective lens (Olympus,

UMPLFLN 10XW, NA = 0.30, WD = 3.3 mm, water immersion), a 25× objective lens (Olympus, XLPL25XWMP, NA = 1.05, WD = 2.0 mm, water immersion), a 25× objective lens (Olympus, XLPN25XSVMP, NA = 1.0, WD = 4.0 mm, designed for refractive index 1.38), a 25× objective lens (Olympus, XLSLPLN25XSVMP, NA = 0.9, WD = 8.0 mm, designed for refractive index 1.38), or a customized 25× objective lens (Olympus, NA = 0.9, WD = 8.0 mm, designed for refractive index 1.48) was used for imaging. MaiTai DeepSee (Spectra-Physics) or InSight DeepSee Dual (Spectra-Physics) was used for two-photon excitation of EYFP at 920 or 950 nm, respectively, and the fluorescence signals were quantified with a non-descanned GaAsP PMT. For the 25× objective lens, correction collars were used to achieve best brightness and resolution. Laser power was manually adjusted to give constant fluorescence intensities at all depths. Imaging and stitching of tiled images were carried out with a motorized stage (Sigma Koki) and Fluoview FV10-ASW software (Olympus). For visualizing projection images and three-dimensional reconstructions, Neurolucida software (MBF Bioscience) was used.

2.2.4. *In vivo* two-photon imaging

Anesthetized mice were head-fixed under a microscope. An upright multiphoton microscope (Olympus, FV1000MPE) was used for imaging with a water immersion 25× objective lens (Olympus, XLPLN25XWMP, NA = 1.05, WD = 2.0). AlexaFluor 488 dextran was excited at 920 nm using MaiTai DeepSee (Spectra-Physics).

2.3. Neuronal tracing and histochemistry

2.3.1. *In vivo* electroporation of fluorescent dextran dyes [34]

For single-glomerulus labeling, *OMP-GFP* or *Thy1-YFP-G* mice were used. Mice (P21-28) were injected with Nembutal (Dainippon Sumitomo Pharma) (50

mg/kg body weight), RIMADYL (Pfizer) and Dexamethasone (Kyoritsu Seiyaku). Anesthetized mice were kept on a heating pad set at 35℃. The skull overlying the dorsal olfactory bulb was carefully removed keeping the dura mater intact. A pulled glass pipette (outer tip diameter = 5-10 μm) was backfilled with AlexaFluor 488 or 647-dextran (10 kDa, Invitrogen) diluted in PBS at 0.5%. Under a fluorescence stereo microscope (Leica M205C) the pipette was moved into the glomerular layer of the olfactory bulb using a micromanipulator (Narishige). Pulsed positive current (1 μA, 0.5 sec ON / 1.5 sec OFF cycle) was applied for 5 min using an iontophoresis current generator (STOELTING). After current injection, the dura was overlaid with Kwik-Sil (WPI) and sealed with a coverslip. Three hours later, the mice were analyzed by *in vivo* two-photon imaging and/or sacrificed for optical clearing.

2.3.2. DiI labeling

Excised mouse brain samples (P5 and P7) were fixed with 4% PFA in PBS at 4℃ overnight. DiI labeling was performed as described previously. A small incision was made with a scalpel in the lateral olfactory tract, and a small DiI C_{18} crystal (Invitrogen) was placed into the incision. The brain sample was then incubated in 2% or 4% PFA in PBS at 37℃ for 5-21 days. The samples were then cleared with SeeDB. Cleared whole-mount samples were imaged using an inverted confocal microscope (Olympus, FV1000) with a He-Ne laser (543 nm).

2.3.3. Immunohistochemistry of sections

Brain samples cleared with Sca*l*eA2 were restored in PBS overnight and then post-fixed in 4% PFA in PBS overnight. Samples cleared with SeeDB were serially incubated in 80%, 60%, 40%, and 20% fructose, each for 8 hours, and then in PBS overnight. Restored samples were cryoprotected with 30% sucrose overnight and embedded in O.C.T. compound (Sakura). Coronal sections 20 μm-thick were cut with a cryostat (Leica). Cryosections were fixed with 4% PFA in PBS for 15 minutes.

Sections were then blocked with 2% donkey serum for 1 hour and then incubated with rabbit anti-Gephyrin antibodies (Abcam, ab25784) at 1:100 or with mouse anti-MAP2 antibodies (Sigma, M9942) at 1:200 overnight at 4°C. After three washes with PBS, sections were incubated with Alexa647-conjugated secondary antibodies at 1:250 for 1 hour. DAPI was used for nuclear counterstaining. Images were acquired with a confocal microscope (Olympus, FV1000).

2.3.4. Whole-mount immunohistochemistry [35]

Dissected brain samples of P21 *OMP-GFP* knock-in mice were fixed in 4% PFA overnight. Samples were then permeabilized in 10% BSA in PBST (1% Triton-X 100 in PBS) overnight at 4°C. Next, the samples were incubated with chicken anti-Tyrosine Hydroxylase (anti-TH; Abcam, ab76442, 1:250) in 10% BSA in PBST for 48 hours at 4°C. After three successive 30-minute washes in PBST, samples were incubated with Goat anti-chicken Alexa 647 (Invitrogen, 1:250) in 10% BSA in PBST for 24 hours at 4°C. Samples were then washed three times in PBST. Finally, the samples were cleared with SeeDB and imaged using confocal microscopy.

2.4. Quantifications of light transmittance and fluorescence

2.4.1. Quantification of fluorescence intensities of brain sections.

To evaluate stability of fluorescent proteins in tissues, we used brain sections of *Thy1-YFP-G* mouse line, and mice electroporated with fluorescent proteins (ECFP, EGFP, EYFP, and tdTomato). Cryosections (20-μm thick) on glass slides were fixed with 4% PFA in PBS for 15 minutes and rinsed in PBS. Sections were then incubated in various optical clearing agents at room temperature. For BABB and dibenzyl ether, sections were air-dried before incubation. An inverted fluorescent microscope (Leica, DMI6000B) with a cooled CCD camera were used to evaluate quenching of fluorescent proteins in the clearing agents. The sections were imaged in the same area

over a period of time. Fluorescence intensity was standardized to intensity in PBS (100%).

2.4.2. Measurement of light transmittance

Light transmittance of clearing agents and cleared brain tissues was determined using a spectrophotometer (Beckman DU730). The light scattering of adult brain was non-homogeneous due to presence of myelinated structures; therefore, we used P21 mouse hemi-brains for transmittance measurements. Because sample expansion alone can reduce light scattering, we used samples with a defined thickness for clearing and then compared their transmittance values.

2.4.3. Measurement of sample size changes

For the measurement of sample expansion/shrinkage, the mouse brain samples (P3 or P21) were cut along the midline, and hemi-forebrains were excised. Photos were taken of samples placed on a glass dish with the midplane on the bottom. Based on top view photos, the area of the midplane was determined using MetaMorph software (Molecular Devices). The linear expansion value was determined by the square root of the area size changes.

2.5 *In utero* electroporation

pCAG-EGFP vector (2μg/μl) was used for *in utero* electroporation to label callosal axons. pCAG-loxP-Neo-loxP-EYFP (2 μg/μl) and pCAG-Cre (0.02-0.2 ng/ul) were co-electroporated to sparsely label the callosal projection neurons. To evaluate stability of fluorescent proteins, pCAG-ECFP/EGFP/EYFP/tdTomato were electroporated into the cerebral cortex. *In vivo* electroporation was performed as described previously. Pregnant ICR mice were anesthetized with Nembutal and the uterine horns carrying embryos were exposed through a midline abdominal incision. At E15, 1 μl of plasmid solutions (2 μg/μl) diluted in PBS were injected into the

lateral ventricle of the embryos using a micropipette made from a glass capillary. Subsequently, electric pulses (driving pulses at 32V for 50 msec at 950 msec intervals) were delivered 5 times with forceps-type electrodes and a CUY21EX electroporator (BEX). The uterine horns were then placed back into the abdominal cavity before suturing the abdominal wall and skin. Electroporated mice developed normally and were dissected at P7. FastGreen is commonly used to visualize DNA solutions for in utero electroporation, but it caused strong background fluorescence after SeeDB treatment, hindering fluorescence imaging. Therefore, we used 0.05% AlexaFluor 647-dextran (MW = 10kD) or 0.01% AlexaFluor 647 Hydrazide to visualize DNA solutions in blue, when necessary.

2.6. Reconstruction of mitral cell dendrites

Confocal images of mitral cells were analyzed using Neurolucida software (MBF Bioscience). Dendrites were manually traced in 3D space. To quantify coverage area of a mitral cell, the z-projected images were analyzed. Coverage area was defined as the area within a distance of 100 μm from lateral dendrites of a mitral cell. Overlapping areas were quantified using Metamorph software (Molecular Devices). To determine the radius of glomeruli, the area of glomeruli in z-projected images were measured. And then the radius was given as $(\text{area}/\pi)^{1/2}$.

2.7. Statistical analysis

Prism5 software (GraphPad) was used for statistical analysis. Mann-Whitney's U-test was used in **Figure 16**, based on large sample numbers and non-normal distributions. Data are indicated as mean ± s.d. or mean ± s.e.m.

3. Results

3.1. Optical clearing with high refractive index solution

Based on previous studies, I consider that the preferred solution for optical clearing of fluorescent protein labelled biological tissues is a water soluble reagent with high refractive index. In addition, the liquid should be colorless, non-erosive, and chemically stable. I also sought for a reagent that is able to penetrate the tissue without destroying the cellular structures. To evaluate the potential in optical clearing of high refractive index solutions, I focused on two groups of chemicals known to have high refractive index: iodides and sugars.

3.1.1. Evaluations for clearing potential

Zinc iodide is a stable salt that provides a wide range of choices in refractive index (from 1.378 to 1.619), have been used in optical flow diagnosis [36]. In terms of penetration efficiency, which is an important factor for immersing optical clearing, zinc iodide solution is ideal, because of its small size. When compared with other high refractive index solutions, zinc iodide solutions are highly fluid even when they are saturated (RI ~1.619). The samples were treated with zinc iodide by serially incubating with increasing concentration of zinc iodide solution and finally soaked them in 60% zinc iodide (RI ~ 1.495). Owing to the high osmotic pressure, however, the brains subjected to severe shrinkage. Although the refractive index was largely elevated, the samples were not transparent as expected (**Figure 5a**).

Previously, high-concentration sucrose solutions have been used to reduce light scattering of the brain and invertebrate samples. Glucose, fructose, and sorbitol have been reported to reversibly alter the optical properties of skin, and reduce the light scattering [23,37]. So I considered sugars are good candidates for optical clearing. Among various sugar solutions tested, I found fructose solution to be a potential

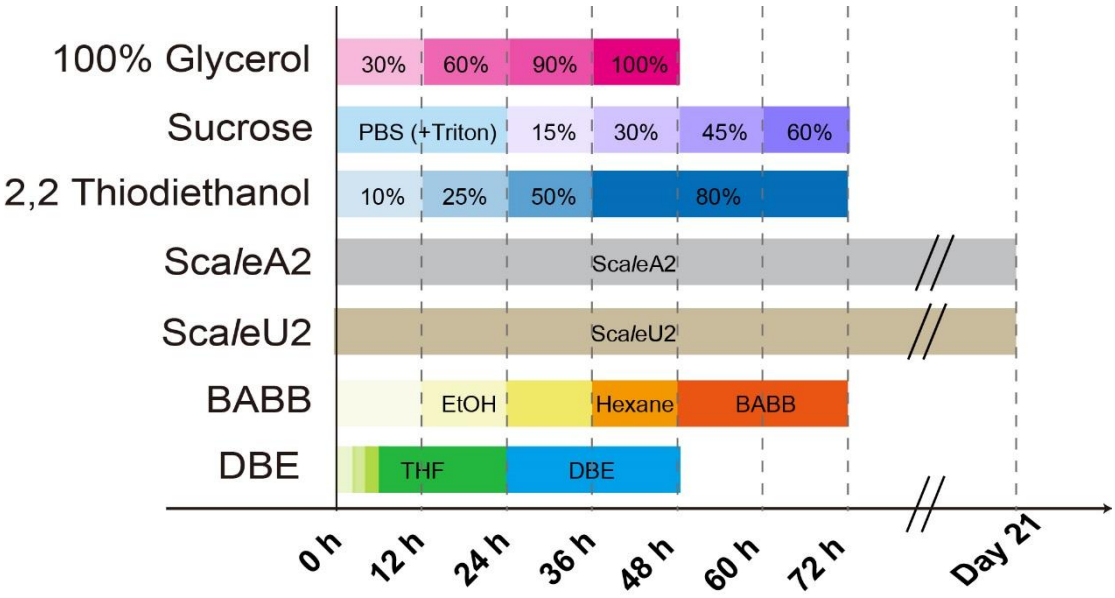

Figure 4 Schematic diagram for optical clearing methods. Abbreviations: PBS, phosphate buffered solution; BABB, benzyl alcohol-benzyl benzoate; EtOH, ethanol; DBE, dibenzyl ether; THF, tetrahydrofuran.

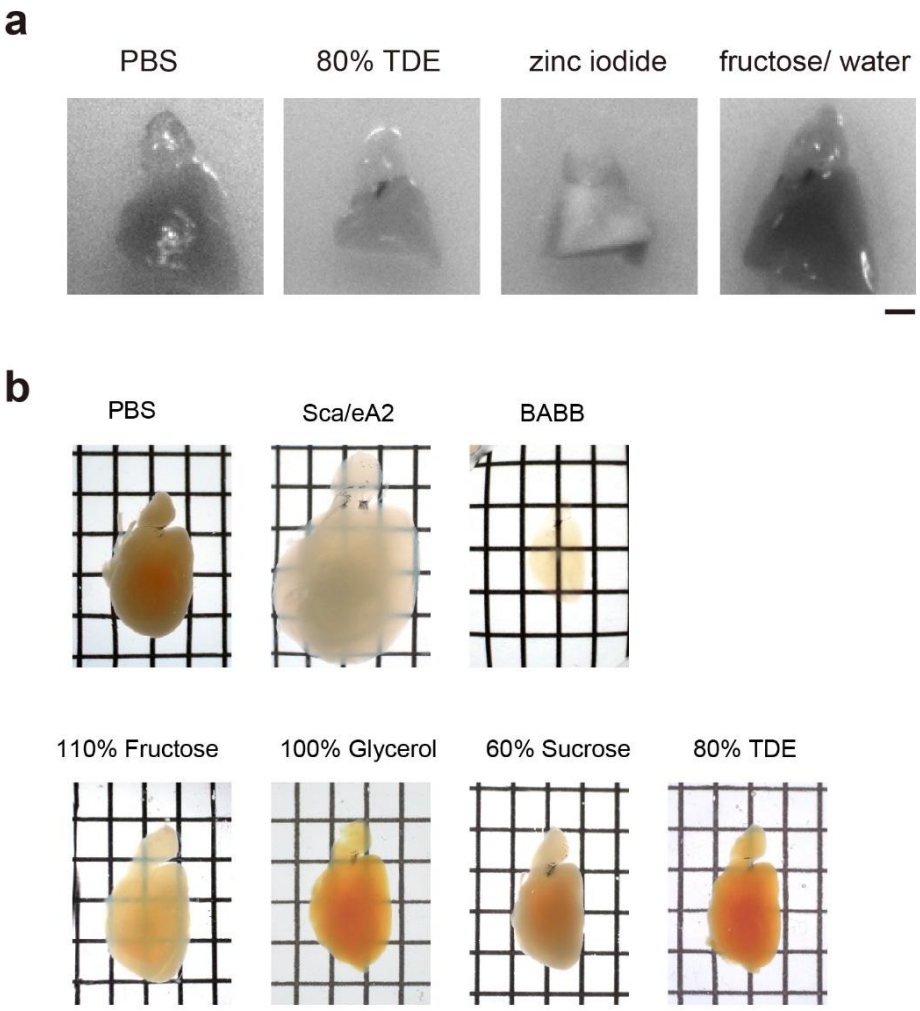
a
PBS
80% TDE
zinc iodide
fructose/ water
b
PBS
Sca/eA2
BABB
110% Fructose
100% Glycerol
60% Sucrose
80% TDE
c
80% TDE
Sca/eA2
fructose/ water

Figure 5. Optical clearing of adult mouse brain with various high RI regents. (**a**) Adult mouse hemi-brains were incubated with reagents of interest. After series of incubation for 2 to 3 days for full penetration of each candidate solution, brain samples were taken out from the solutions for photographing. In fructose/water and 80% TDE treated samples, the volume of cleared samples was kept; however, in zinc iodide solution, samples were severely shrank and harden like that treated with BABB. Scale bar represents 1 mm. (**b**) Transmission images of cleared mouse hemi-brain. Adult mouse hemi-brains were used for evaluating potential optical clearing reagent. Serial incubation in fructose solutions (finally in 110% fructose solution) can effectively clear the sample without evident morphological changes as seen for Sca*l*eA2 or BABB-cleared samples. On the other hand, serial incubation in glycerol and TDE only resulted in moderate transparency like previous 60% sucrose method. Grids are 2.6 × 3.2 mm. (**c**) Fluorescent imaging of mitral cell layer from the olfactory bulb of *Thy1-YFP-G line* transgenic mice. Adult brain samples were cleared with a gradient of fructose/water (2-day incubation), 80% TDE (3-day incubation), or Sca*l*eA2 (3-week incubation), respectively. After clearing, the intact mouse olfactory bulbs were imaged with confocal microscopy from the dorsal surface of the bulb at the mitral cell layer (depth ~250 μm) with the same laser intensity. Scale bar represents 100 μm. Abbreviations: PBS, phosphate buffered solution; BABB, benzyl alcohol-benzyl benzoate; TDE, 2,2'-thiodiethanol

clearing agent. Compared with other sugars, fructose is more soluble in water **(Table 3**). Fructose can dissolve approximately double the amount of sucrose, thus higher refractive index can be obtained from fructose solution. The refractive index of previously reported optical clearing agent, 60% sucrose solution (w/w) reaches 1.425 at 25℃. In contrast, the refractive index of a saturated fructose/water solution reaches 1.490 at 25℃ (80.2% w/w, 115% w/v) and 1.502 at 37℃ (84.4% w/w, 130% w/v). When gradually incubating the brain samples with increasing concentration of fructose/water solutions for 3 days, samples were cleared and maintained the original volume without obvious swelling found for Sca*l*e-cleared brains or shrinkage for BABB-cleared ones (**Figure 5b**). Accordingly I considered the fructose/water solution to be a potential clearing agent and decided to further compare the optical clearing efficiency of fructose/water solutions with current fluorescent protein-friendly clearing agent.

I further confirmed the stability of fluorescent proteins in the intact olfactory bulb by imaging the mitral cells transgenically labeled with EYFP (**Figure 5c**). After serial incubation of intact *Thy1-YFP-G* line mouse brain in fructose/water solutions, the olfactory bulb was imaged with confocal microscopy from the dorsal surface. Under the same instrumental settings, images of the mitral cell layer were compared with two known optical clearing agent, 80% TDE and Sca*l*eA2. All samples provided clear images on the mitral cell layer. However, the sample cleared by fructose/water solution provided brighter EYFP signals than 80% TDE or Sca*l*eA2-cleared samples, indicating that the fluorescent proteins were best preserved in fructose solutions.

Then I evaluated sample expansions and shrinkages based on day-by-day images of the brain samples **(Figure 6a**). The optical clearing procedure took at least 21 days for Sca*l*eA2, in contrast, the clearing for fructose/water took only 2 to 3 days. I further extended the incubation time of fructose/water to compare the long-term effect of

Table 3. Solubility of various sugars [38].

Name	Molecular weight	Solubility (grams per 100 ml water at 25^{o}C)
D-Fructose	108.16	375
D-galactose	108.16	68.3
D-glucose	108.16	83
Lactose	360.31	21.6
Maltose	360.31	108
D-Mannose	108.16	248
Raffinose	594.52	14
Sucrose	342.2	215
D-xylose	159.13	117

immersion (**Figure 6 a**). During the 3-week-incubation, I noticed the brain samples subjected ~5% shrinkage at the first stage, which is possibly originated from the combinational effect of high osmotic pressure and insufficient mixing (~5 ml of solution was used for fructose/water). Hence the procedures were modified in later experiments to minimize the shrinkage seen in fructose/water solution.

Similar to Sca*l*e method, fructose/water treatment is also reversible. After 3-day incubation in PBS, brain samples were nearly fully recovered in sample volume and appearance. In contrast, the recovery of Sca*l*eA2-treated brains was limited. Samples recovered from Sca*l*eA2 treatment were still 110% expanded (**Figure 6b**).

3.1.2. Fructose/water solution can be a potent optical clearing agent

In previous assay, I evaluated fructose/water solution as a potential optical clearing agent. First, fructose/water treatment can effectively penetrate the tissue and provide similar transparency as Sca*l*eA2 treated samples in 2 to 3 days, which was shorter than 21-day treatment needed for Sca*l*eA2 (**Figure 6b**). Second, biological tissues were physically and chemically stable in fructose/water solution. From the fluorescent images and quantitative analysis of samples volume, fructose/water treatment could be a better choice of optical clearing because the damages were minor than other methods (**Figure 5b** and **6b**). In these assay, I treated paraformaldehyde-fixed mouse brains with a serial incubation in increasing concentration of fructose/water solutions from 20% to 110% (w/v) to gradually replace the fluids in the tissue. For the trial, I separated the incubation procedure into 5 steps (20%, 40%, 60%, 80%, and 110% fructose/water; w/v) and used 5 ml solution for each clearing step. However, the small volume of clearing solution was found to result in minor sample shrinkage (~ 5%) (**Figure 6**). In addition to the variances in sample volume, I found there were brown pigments accumulations after 21-day incubation in 110% fructose/water (w/v) solution; therefore I improved these two

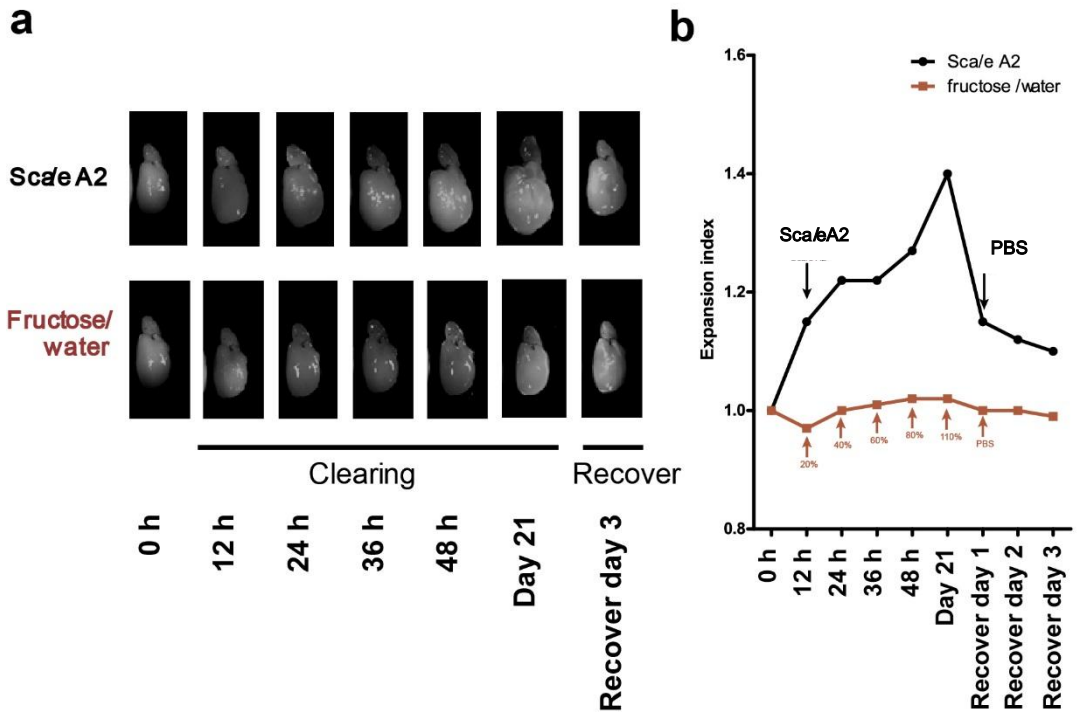

Figure 6. Evaluating the potential of fructose/water solution as an optical clearing agent. (**a**) Adult mouse hemi-brain samples were treated with Sca*l*eA2 and serial fructose solutions (20%, 40% 60%, 80%, and 100% w/v fructose/water). Samples were taken out from the solutions and photographed by top light with black background to calculate the projected area of each sample. Fructose/water-treated samples showed relatively constant sample volume than Sca*l*eA2-treated samples. When the samples were incubating back to PBS, the reversed samples showed similar appearance as that before fructose/water treatment. (**b**) Quantitative analysis of results in (**a**). Optical clearing of Sca*l*eA2 resulted an expansion index of 1.4, standing for 140% sample expansion per dimension. Although the clearing is reversible, the expansion index on recovery day 3 was 1.1, meaning the recovery rate was limited to around 90% after 3-day PBS incubation. In contrast, the sample volumes in fructose/water solutions were relatively constant, with an expansion index close to 1.0 during clearing and recovery process.

points in later experiments to establish a better protocol for clear samples with fructose.

3.2. Formularization of SeeDB: a water-based optical clearing agent using fructose and thiol

3.2.1. Tricks for improving the transparency

To solve the problem in sample volume, I first tried to optimize the penetration of the fructose solutions. Slow diffusion of clearing agents through tissue is an obstacle for optical clearing. As for penetration enhancer, I tried chemical and physical factors to increase the penetration. In order to increase the penetration rate chemically, we applied detergents such as Tritox X-100 to permeabilized the sample. However, adding 0.1 or 0.5% Triton X-100 to fructose/water solutions resulted in sample expainsion (~120% for adult mouse hemi-brain).

Alternatively, I sought for physical strategies. The viscosity of a fructose solution goes higher as the percentage of fructose increases, which hinders penetration. First, I physically improved the penetration by increasing the volume of the clearing solutions form 5 ml to 20 ml and carried out the incubation procedure on an overhead rotator. Large volume and constant mixing helped to improve the transparency, especially in adult mouse brain samples.

I also tried to increase the fluidity by raising the incubation temperature. However, at the high temperature condition (37℃), we found that the brown pigments and the autofluorescence in the brains samples were enhanced (**Figure 7**, left). These side-products are originated form non-enzymatic reaction known as Maillard reaction [39]. Fructose and other reducing sugars undergo the Maillard reaction with amino group of proteins and amino acids, producing insoluble melanoidin pigments (e.g., aldehyde-amine polymers with brown color and fluorescence). These melanoidin

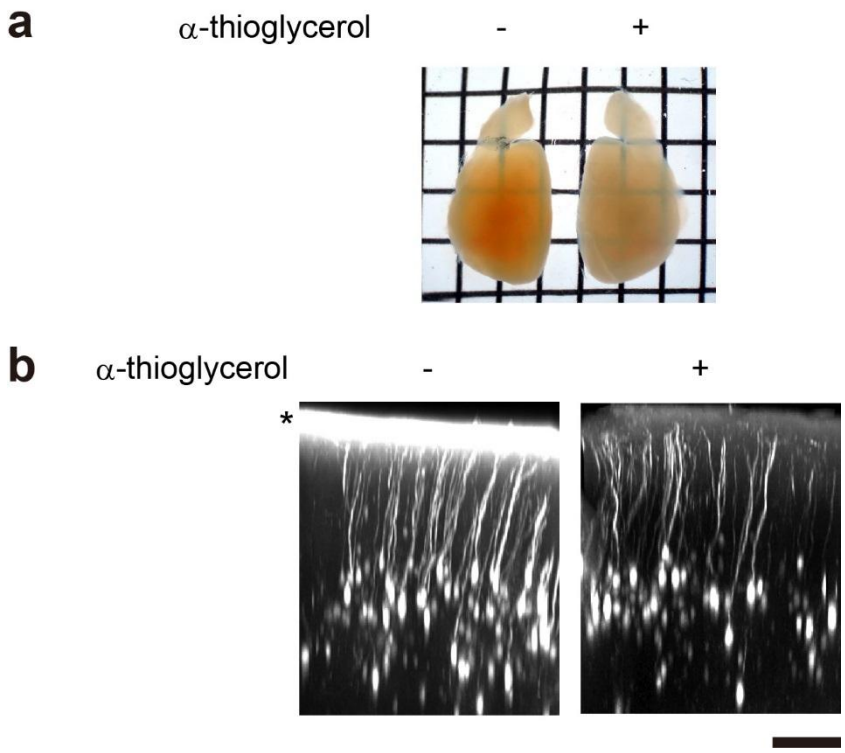

Figure 7. Effects of α-thioglycerol. (**a**) Adult *Thy1-YFP-H line* mouse brains were serially treated with increasing concentration of fructose, namely 20%, 40%, 60%, 80%, and 110% at room temperature for 3 days for optical clearing. Then incubated in 100% fructose solution at 37℃ for 5 days with or without 0.5% α-thioglycerol to examine the effect of α-thioglycerol. With α-thioglycerol protection, browning effect of Maillard reaction was reduced. Grids are 2.6 × 3.2 mm. (**b**) The same set of brain samples shown in (**a**) was imaged from the surface of the cerebral cortex using confocal microscopy. The reconstructed x-z images of the cerebral cortices were shown. Accumulation of autofluorescence in the surface area (*) was prevented by addition of 0.5% α-thioglycerol. Scale bar represents 200 μm.

pigments interfere the imaging by decreasing the signal-to-noise ratio. They are initially generated from the surface, and then gradually invade the entire sample, finally result in an intransparent sample with strong autofluorescence. High temperature accelerates the kinetics in Maillard reaction [40,41]. It has been demonstrated that Maillard reaction will not start until free sulfurs in the environment are totally consumed [42,43]. Sulfurcompounds such as thiourea and 2-mercaptoethanol can react with midproduct of Maillard reaction and divert it to a non-reactive product, which is the one cannot be converted into melanoidin pigments. Because 2-Mercaptoethanol is considered toxic and irritative, a thiol, α-thiglycerol was used in following assays as Maillard reaction inhibitor.

To estimate the effect of thiol, I took adult *Thy1-YFP-H* line mouse brains, in which yellow fluorescent protein (YFP) are expressed at high levels in motor and sensory neurons, as well as subsets of central nervous system neurons. I serially treated one and the other hemi-brains of the same mice in increasing concentration of fructose solutions (20%, 40%, 60%, 80%, and 110% w/v) at room temperature for 3 days. Then the cleared samples were moved to 37℃ incubator for 5 days with various concentrations of α-thioglycerol for assaying suitable dose. 0.5% of α-thioglycerol was found to be effective in reducing brown pigments and autofluorescence in the surface area (**Figure 7**). When the concentration was raised to 2%, brain samples showed swelling during the treatment because excessive thiol cleaves the disulfide bounds and disrupts structure of proteins. Hence the concentration of α-thioglycerol was determined as 0.5% (v/v) in each fructose solution.

To further optimize the refractive index, fructose solution used in the final step was raised to the saturated concentration (80.2% w/w, 115% w/v) at room temperature (25℃) with a refractive index of 1.490. The optimized solution was termed as SeeDB (See Deep Brain), which refers to a saturated solution of fructose in water (80.2% w/w, 115% w/v) with 0.5% α-thioglycerol. As summarized in schematic

diagram in Figure 8, for SeeDB treatment, the procedure was spilt into 6 steps. I treated paraformaldehyde-fixed embryo and brain samples serially with 20%, 40%, 60%, 80%, and 100% w/v fructose solutions and finally in SeeDB at room temperature (25℃). Samples were enclosed in a 50 ml conical tube on an overhead rotator to be freely mixed with fructose solution. From step 1 to 3, I incubated the samples with 20 ml of 20%, 40%, and 60% of fructose solution for 8 hours in each step. Then I incubated the sample with 80% and 100% fructose (w/v) solution for 12 hours for each step. Finally I equilibrated them in SeeDB for 24 hours. The entire procedure took approximately three days, which is much quicker than optical clearing with Sca*l*e method, which takes three weeks (Sca*l*eA2) to 6 months (Sca*l*eU2) for clearing a mouse brain.

I also compared the volume changes during optical clearing of this optimized SeeDB protocol. The volumetric change of SeeDB-treated samples was within 3% per dimension (**Figure 8**). Together with transmission images of adult mouse hemi-brains in Figure 9, I confirmed that the clearing efficiency of SeeDB was better than other water-based optical clearing solutions.

3.2.2. Clearing efficiency of SeeDB

To evaluate tissue transparency, I quantified light transmittance in P21 mouse hemi-forebrain samples (**Figure 10**). Myelinated structures in adult brain caused non-homogeneous scattering and generate large variations in measurements. In contrast, P21 mouse brain samples showed more homogeneous scattering. I therefore acquired the quantitative data form P21 mouse hemi-forebrains using spectrophotometer. Brain samples treated with SeeDB were more permissive to light than those treated with 60% sucrose or Sca*l*eA2 for 3 days. The transmission curves were comparable between those treated with Sca*l*eA2 for 21 days and those treated with SeeDB for 3 days under the wavelength range of 400-950 nm (**Figure 10b**).

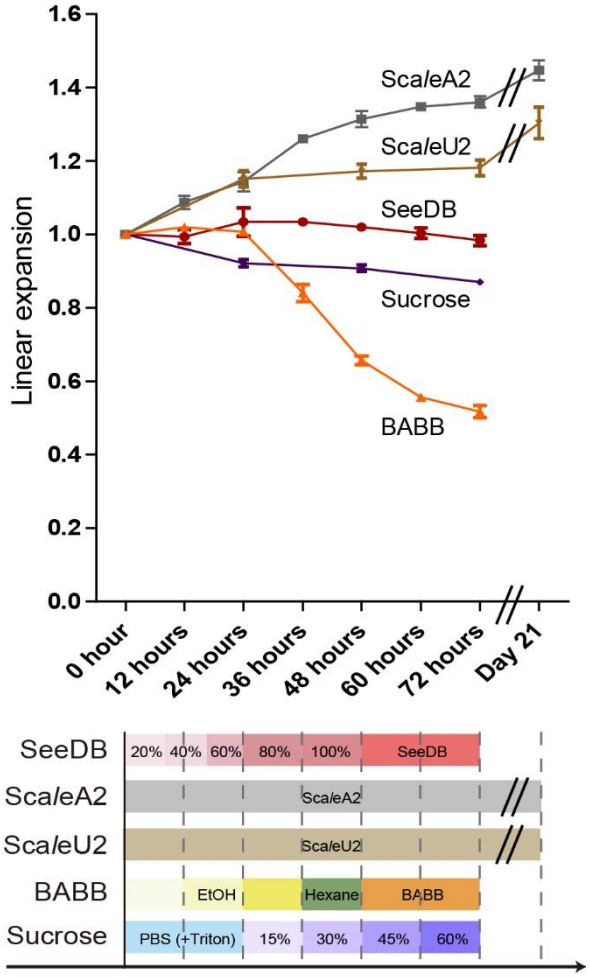

Figure 8. Quantitative analysis of sample volumes during optical clearing procedure. Adult mouse brains were treated with various optical clearing agents following the procedure shown in the schematic diagram. Hemi-brain samples with the midplane on the bottom were photographed from the lateral side every 12 hours for first 72 hours. An additional image of Sca*l*e-treated samples were taken on day 21. Based on top view photos, the area size (expansion for the two-dimension) can be calculated and then transfer into linear expansion value by the square root of the area size. Error bars indicate s.e.m. (n = 3 hemi-forebrains each).

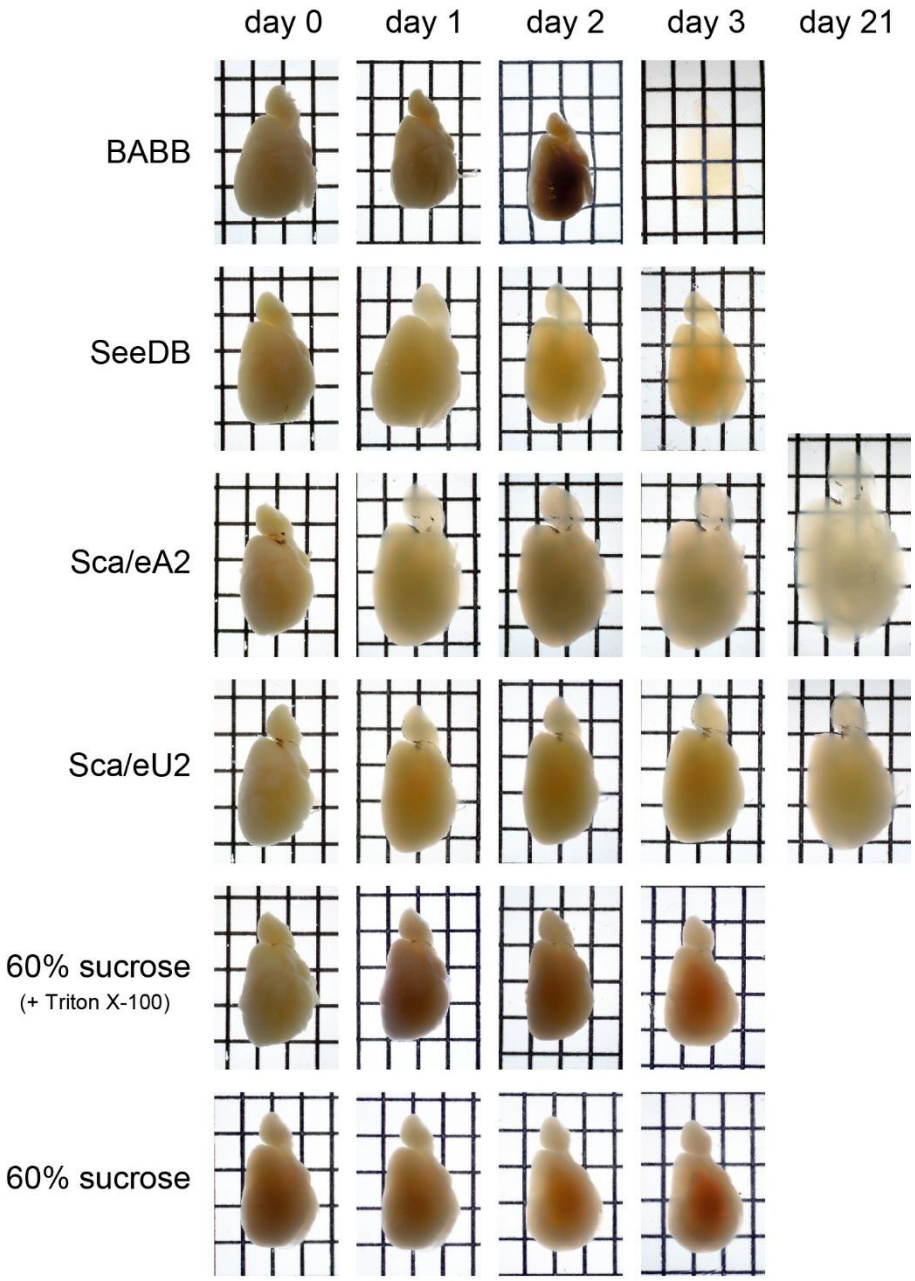

Figure 9. Transmission images of adult mouse hemi-brain samples cleared with various optical clearing agents following the procedure shown in Figure 8. Grids are 2.6 × 3.2 mm.

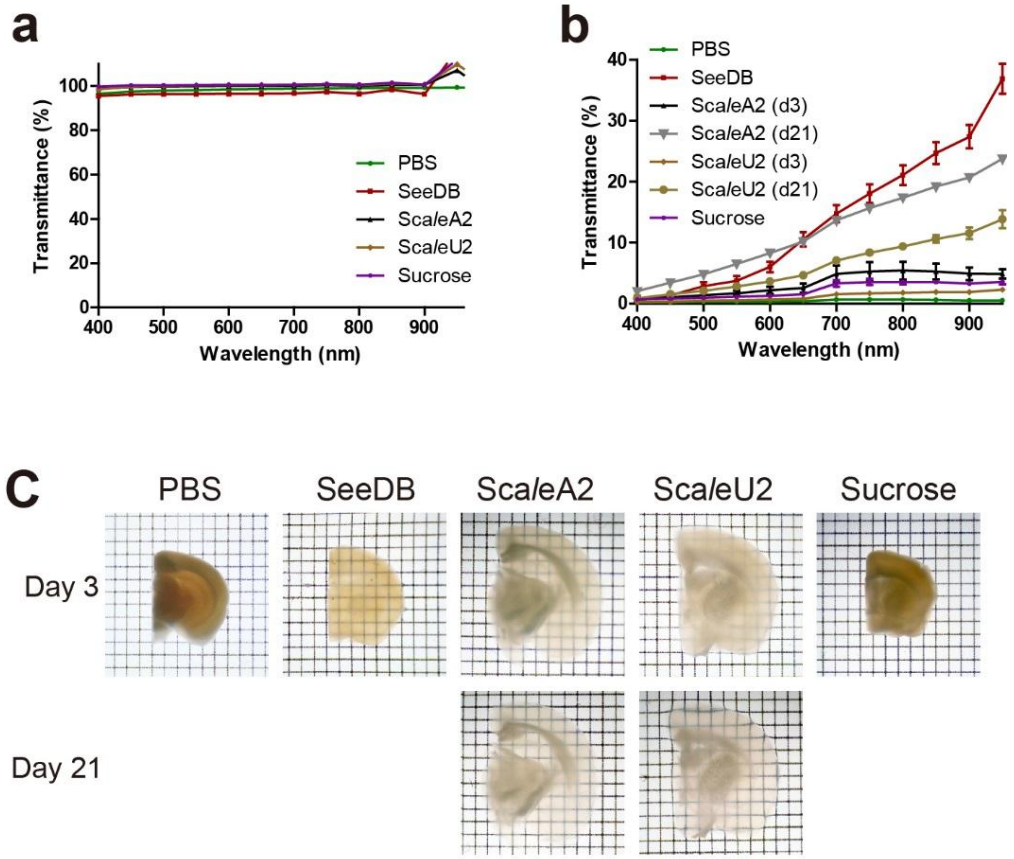

Figure 10. Quantification for optical clearing efficiency in SeeDB and other optical clearing agents. (**a**) Transmittance curves of various clearing agents, at 400 nm to 950 nm (mean ± s.e.m., n = 3). (**b**) Transmittance curves of mouse brain samples (P21) cleared with various clearing agents. Intact mouse hemi-brain samples were used for the measurement. Transmittance was measured along the thickest part of medial-lateral axis of the hemi-brain samples (5.13 ± 0.19 mm, mean ± s.d., before clearing, n = 3). Transparency of SeeDB-treated sample were significantly increased (**c**) Adult brain slices (P66, 1.5 mm thick) were cleared with various clearing agents (transmission images). After optical clearing, both gray and white matter were fully cleared with SeeDB, although the white matter was still opaque when cleared with Sca*l*eA2 for 21 days. Sucrose treatment provided only partial clearing of the brain slice, and both gray and white matter were opaque. Grids are 1 × 1 mm.

However, under infrared light (700-950 nm) SeeDB-cleared samples were substantially more permissive than Scale-*c*leared ones. Although morphological changes are reduce by Sca*l*eU2 treatment in Sca*l*e technique, the transparency of the cleared samples was compromised (**Figure 9** and **Figure 10b**).

Optical clearing of fixed brain tissue are typically evaluated with gray matter, however, the white matter scatters much stronger because it is highly myelinated and rich in lipids. To evaluate the optical clearing effect specifically on these two distinct areas, adult mouse brain slices were examined. I used 1.5 mm-thick adult (P66) forebrain slices to analyze the optical property changes by various clearing agents (**Figure 10c**). After optical clearing, both gray and white matter were fully cleared with SeeDB. In contrast, 21-day incubation of Sca*l*eA2 was not able to fully clear the white matter of the brain because the refractive index of Sca*l*eA2 (~1.38) is lower than that of lipid in the myelinated structures. Treatment of 60% Sucrose provided only partial clearing of the brain slice.

3.2.3. Alternative solution for neonatal brain samples: SeeDBp

When I tried to apply standard SeeDB protocol to various types of mouse brain samples, 125% linear expansion was observed in SeeDB-cleared neonatal brains (**Figure 11a**). Therefore I revisited the sample expansion issue and adjusted the osmotic pressure of fructose solutions with salts. After screening various salts, I found that addition of 0.1× PBS in the 20-80% fructose solutions could minimize the volumetric changes without compromising optical clearing efficiency (**Figure 11c** and **12a, middle**). The inclusion of 0.1× PBS was limited to the first 4 steps, because excessive salts in 100% fructose solution resulted in sample shrinkage. Hence the last 2 steps of SeeDBp protocol used the same condition as in SeeDB protocol, in which 100% w/v fructose solution and SeeDB were dissolved in distilled water. When

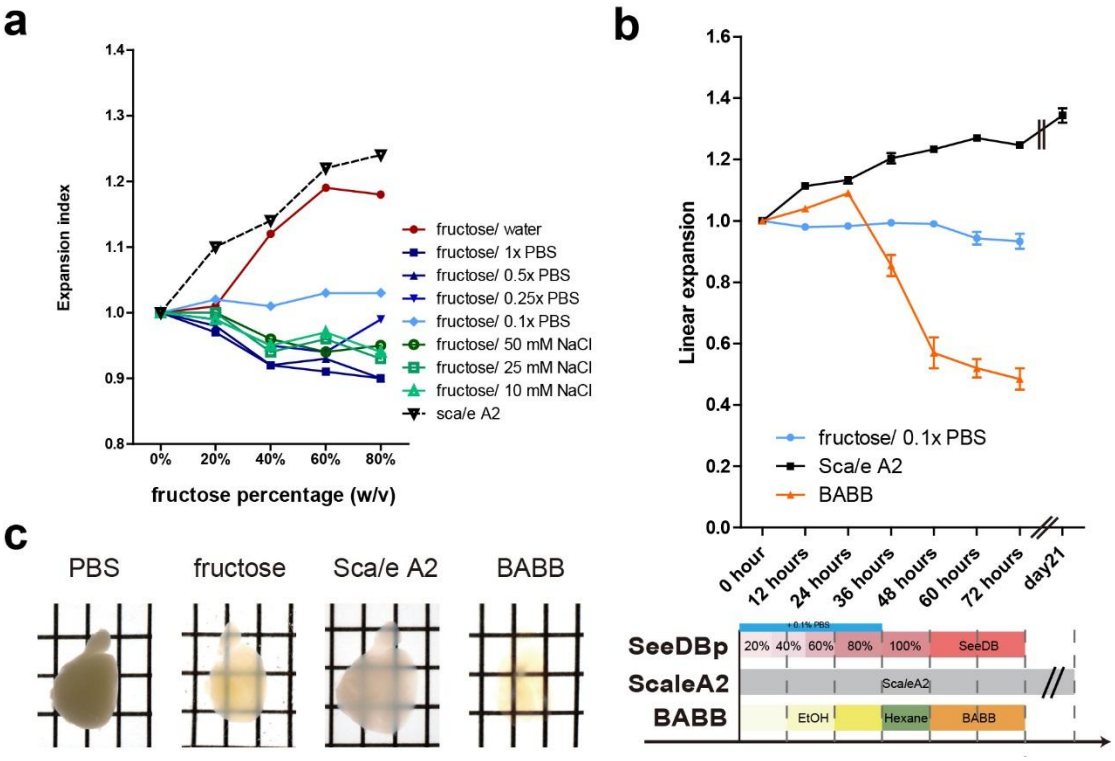

Figure 11. Optimized clearing condition (SeeDBp) for neonatal brain samples. (**a**) Neonatal brain samples swelled during optical clearing with standard SeeDB protocol (up to 125% linear expansion). Recipe for neonatals was optimized with additional 0.1× PBS included in the 20-80% (w/v) fructose solutions. The adjustment minimized the sample volume changes seen in SeeDB protocol without compromising optical clarity. (**b**) Sample expansion/shrinkage during the optical clearing in neonatal brains. P3 mouse forebrains were used for measurements (mean ± s.e.m., n = 3). Hemi-brain samples were treated with SeeDBp, Sca*l*eA2, and BABB following the schematic diagram shown in the bottom. (**c**) Transmission images of neonatal mouse forebrains from (**b**). Grids are 2.6 × 3.2 mm.

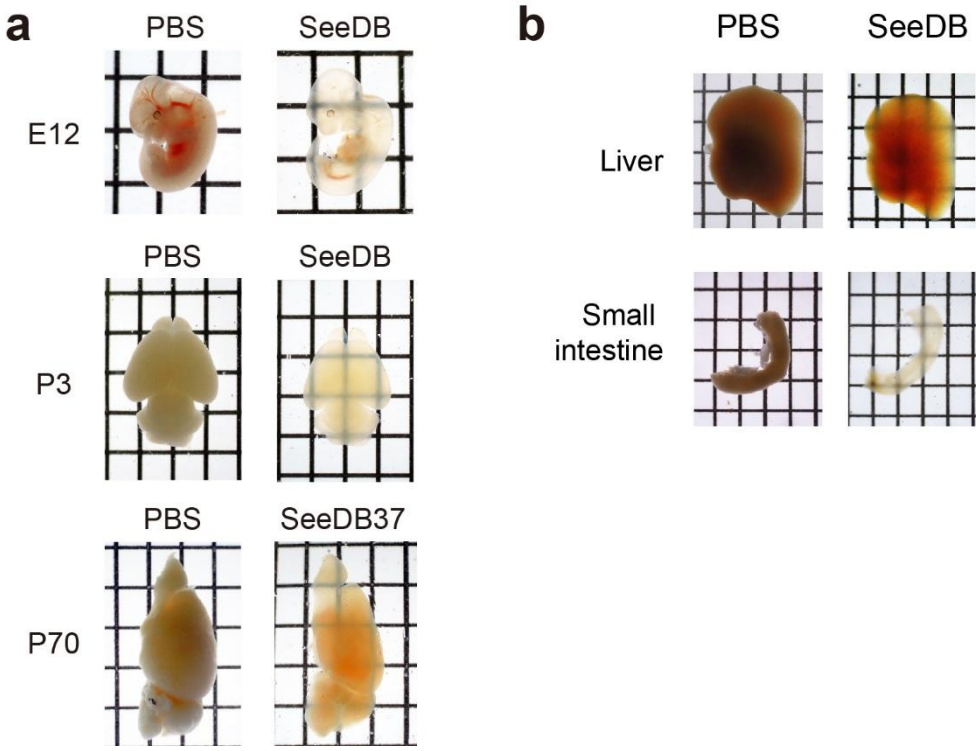

Figure 12. Optical clearing of various mouse tissues (**a**) Transmission images of mouse embryo and hemi-brains after treatment with SeeDB. Whole embryos (E12) were cleared with SeeDB using standard SeeDB protocol. Neonatal (P3) whole-brain samples were cleared with SeeDBp protocol. Adult hemi-brain samples (P70) were cleared with SeeDB37 protocol. (**b**) Transmission image of mouse liver and small intestine after 3-day treatment of standard SeeDB protocol. SeeDB method also worked for these tissues. Grids in (**a**) (**b**) are 2.6 × 3.2 mm.

handling fragile samples, it is ideal to embed the samples in 1% agarose gel prior to optical clearing, and use less vigorous shaking condition

3.2.4. Alternative solutions for aged brain samples: SeeDB37 and SeeDB37ht

For adult brain samples, optical clarity of samples could be further improved with SeeDB37 (84.4% w/w, 130% w/v, RI = 1.502), which is saturated fructose solution at 37℃. For this reason, SeeDB37 solution and SeeDB37-cleared samples had to be kept at 37℃ to prevent precipitation of fructose crystals. As shown in Figure 13, SeeDB37 protocol is an extension of standard SeeDB protocol, which appended 24-hour incubation of SeeDB37 at 37℃ after the treatment of SeeDB. In SeeDB37, the refractive index of the media is raised to 1.502, which was shown to be useful for aged or lipid-rich samples (e.g., the adult mouse brains) to improve transparency (**Figure 12a, bottom**).

The most important part of SeeDB optical clearing is to equibriate the sample gradually with increasing the concentrations of fructose solutions. However, a high concentration of fructose is extremely viscous. Therefore, it is difficult to clear a whole-mount mouse brain with SeeDB or SeeDB37 protocol because of limited penetration. Although it was possible to clear a whole-brain of young mice (P21-P28) with SeeDB37 protocol, optical clearing of whole-mount adult mouse brains was especially difficult and needed further improvement. In order to enhance the penetration of fructose into the sample, the incubation temperature was raised to increase the fluidity of fructose solutions, which was termed SeeDB37ht protocol. The composition of the solutions used in SeeDB37ht protocol was the same as that used in SeeDB37 protocol. However, the incubation time for each step was modified to minimize the swelling during the incubation at 50℃, a relatively high temperature condition. With SeeDB37ht protocol, optical clearing of whole brain from adult mice was possible, although some fluorescent proteins are partially quenched and the

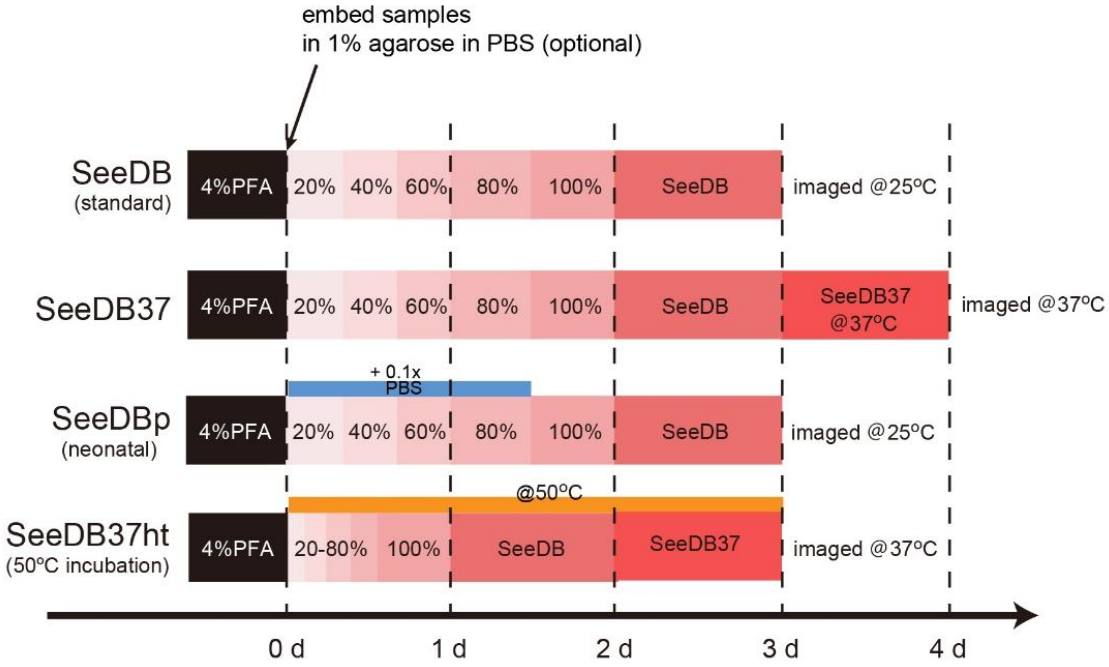

Figure 13. Schematic diagram of experimental procedure. Standard SeeDB is a general protocol for most kinds of brain samples. SeeDB37 is an extended version of standard SeeDB for aged brains with incubation in SeeDB37 at 37℃ to improve the clearing efficiency. SeeDB37ht protocol is designed for large and/or lipid-rich samples that is performed at 50°C. Other procedures are performed at room temperature (25℃). In SeeDBp protocol, for the clearing of neonatal mouse brains, 20-80% (w/v) fructose are prepared with 0.1× PBS instead of distilled water. Addition of 0.5% α-thioglycerol is recommended for all the fructose solutions.

sample volume is somewhat expanded.

SeeDB method worked not only for brain tissues, but also for other types of tissue, such liver and small intestine (**Figure 12b**). SeeDB method is a quick, easy and highly reproducible strategy for optical clearing of paraformaldehyde-fixed tissues. The entire procedure takes approximately 3 days. SeeDB works by matching the refractive index of media with that of the scatters inside a biological sample. Figure 13 summarizes all of the SeeDB variations. Standard SeeDB protocol provides general usage to most types of tissues, and it is suitable for the first trial of the optical clearing procedure. SeeDBp protocol contains optimized solutions with additional PBS, which is specialized for samples (e.g., neonatal mouse brains) that show sample swelling in standard SeeDB protocol. Alternative procedures, SeeDB37 and SeeDB37ht protocol are designed for large and/or lipid-rich samples. A Maillard reaction inhibitor, α-thioglycerol is included at 0.5% for all clearing solution of SeeDB method. However, because autofluorescence gradually accumulates, SeeDB-cleared samples had to be immediately imaged within a few days.

3.3. Chemical compatibilities of SeeDB

3.3.1. Fluorescent protein-friendly nature of SeeDB

Various tools have been developed for specific expression in cells or subcellular structures. For example, anterograde tracing with genetic markers provide valuable applications in tracing axonal projections. Fluorescent proteins also provide wide applications in transgenic labeling and viral tracing. Hence it is an important issue whether fluorescent proteins are preserved in optical clearing solutions.

Quenching kinetics of fluorescent proteins in tissues was difficult to evaluate. Optical clearing process in bulky tissues is also difficult to measure. For example, fluorescent protein intensity is impossible to measure from thick samples before clearing and the time scale is hard to define because incubation time for optical clearing can range from 3 days for SeeDB method to weeks for Sca*l*eA2. Moreover, in time lapse observation, fluorescent quenching also occurs by photobleaching. Alternatively, some groups used purified fluorescent proteins to quantify the stability of fluorescent proteins in optical clearing solutions. However, it is difficult to estimate the real fluorescent protein intensity in tissues because the fluorescent proteins are partially lost from the tissue in some optical clearing agent. Hence I used tissue sections to compare the quenching of fluorescent proteins in various optical clearing agents.

First, I verified the quenching of the cryosections of *Thy1-YFP-G* line transgenic mice expressing enhanced yellow fluorescent protein (EYFP) in the olfactory bulb. I fixed the sections with 4% paraformadehyde for 30 minutes and then washed the sections with PBS 3 times before starting treatments. For optical clearing method that requires dehydration (e.g., dibenzyl ether and BABB method), I air dried the sections for 30 minutes instead of alcohol dehydration; for other water-based methods, clearing solutions were directly mounted to the slices. Then, every section was imaged on the time point of 2, 8, and 24 hours with fluorescence microscopy.

Fluorescence intensity from each optical clearing condition was normalized with that treated with PBS (**Figure 14a**, graph). After 24-hour incubation in various clearing and mounting solutions, slices treated with SeeDB preserved most (~70%) fluorescent signals of EYFP. However, the fluorescence intensity decayed quickly when exposed to organic solvents, BABB and dibenzyl ether. SeeDB was also superior to other water-based optical clearing agent.

To further investigate the quenching dynamics of other fluorescent proteins, I took the mouse brain slices from that electroporated with various fluorescent proteins (ECFP, EGFP, EYFP, and tdTomato). The plasmids were introduced to embryonic mice aged E15, to deliver fluorescent protein in layer II/III neurons. Then the mice were fixed at P7 for cryosections. The same assay was used to verify the quenching with extended incubation time up to 72 hours (**Figure 14b**). Quantification data indicated that the fluorescent proteins were more stable in SeeDB. It generally preserved ~70% (relative to PBS control) of fluorescent signals, although the stability was slightly different depending on the fluophore.

3.3.2. SeeDB preserved detailed morphology and is suitable for quantitative analysis

To evaluate the changes in morphology during optical clearing, I sparsely labeled a small population of mitral cells in the olfactory bulb using fluorescent dextran tracers. For *in vivo* imaging, dextran Alexa 488 was selected for two-photon microscopy. After anesthesia and electroporation, a cranial window over the olfactory bulb was carefully made with a coverlip, and then subjected to *in vivo* imaging. *In vivo* images of the olfactory bulbs were acquired using a two-photon microscope with a 25× objective lens (Olympus, XLPLN25XWMP). For measuring morphological changes in the optical clearing process, dextran Alexa 647 was electroporated to the olfactory bub *in vivo*, and the mouse brains were fixed with transcardial perfusion

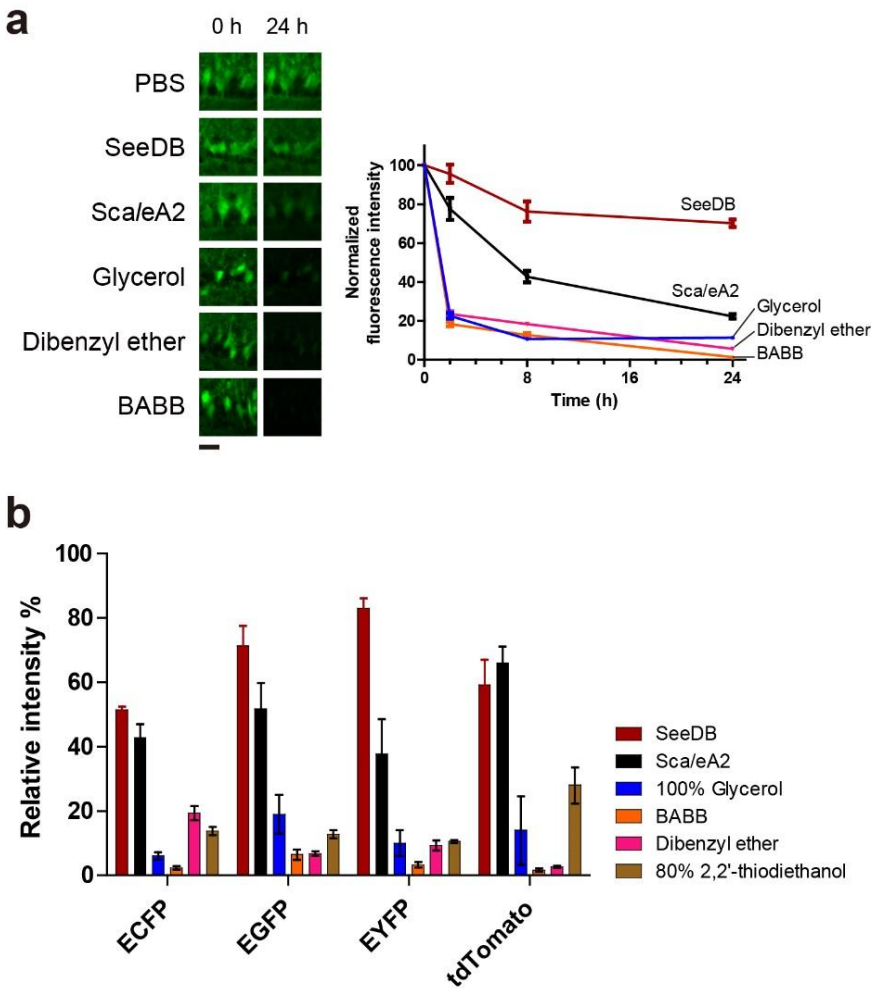

Figure 14 Stability of fluorescent proteins in tissues. (**a**) Fluorescence of EYFP before and after clearing with various agents. Cryosections of olfactory bulb from *Thy1-YFP-G* mouse were used for quantification. Scale bar represents 20 μm. Quantifications of fluorescence intensity for EYFP are shown on the right (mean ± s.e.m., 5 ROI for each). (**b**) Cryosections of mouse brains electroporated with various fluorescent proteins (ECFP, EGFP, EYFP, and tdTomato) were analyzed. Samples were cleared with various clearing agents. Quantification of fluorescence in tissue sections after optical clearing for 72 hours (% PBS samples) is shown. Data are mean ± s.e.m. for 5 ROIs. A representative result out of 3 independent experiments is shown.

after 3 hours. Optical clearing procedure followed the schematic diagram in Figure 7 and then the olfactory bulbs were imaged with a confocal microscope with a 20× objective lens (Olympus, UPLSAPO20X). After optical clearing with Sca*l*eA2, the dendrites of labeled mitral cells appeared highly serrated, most likely due to the anisotropic increase in sample volume (**Figure 15a**, right). In contrast, such morphological deformations were not observed in SeeDB-treated samples; the morphology of dendrites remained indistinguishable from those *in vivo* (**Figure 15a**, middle). In order to conduct quantitative measurements of dendrite tortuosity, we defined the tortuosity index (d/D) for segmented lateral dendrites of mitral cells at perisomatic site, branch point, end point, and end of the image field (red dots in schema of **Figure 15b**).

3.3.3. SeeDB is suitable for lipophilic dyes

Because SeeDB does not use detergents, the structure of the tissues was not altered and the plasma membrane should be maintained. For this reason, I considered that SeeDB method could be potentially suitable for lipophilic tracer dyes.

Lipophilic dyes (e.g., DiI, DiO, and their analogs) have been used to label various types of cell and enable cancer biologists to track a wide variety of tumor and immune cell functions both *in vitro* and *in vivo* [44,45,46]. Cell membranes provide a convenient conduit for loading live and fixed cells with lipophilic dyes, lateral diffusion of the dye within the membrane help the staining of the entire cell. These properties are also advantageous for anterograde and retrograde tracing of neurons. DiI-labeled motor neurons reportedly have remained viable for up to four weeks in culture and up to one year *in vivo* [47]. Because the trafficking of lipophilic dyes depends on lateral diffusion rather than active transportation [48], lipophilic dyes are the only choice to trace neurons in fixed tissues. In previous methods, organic

solvents or detergents have been used in optical clearing agents [49]. Because the membrane structures are washed out by these reagents during the incubation process, they are unsuitable for lipophilic tracers.

In Figure16, I present the DiI tracing of the olfactory neurons in the mouse brain. A crystal of DiI was inserted to a small incision on lateral olfactory tract (LOT) of fixed P5 or P7 mouse brain. After one-week incubation, the whole-brains were cleared with SeeDBp, and then imaged with confocal microscopy. From the LOT, the tracer was diffused through the axons of the mitral cells back to the cell bodies and dendrites (**Figure 16a**) and down to the axons projecting to the Piriform cortex (**Figure 16c**).

3.3.4. Cryosectioning and immunohistochemistry of SeeDB-treated samples

SeeDB methods are highly reversible; all SeeDB-cleared samples can be restored back to PBS. We carefully reversed the clearing procedures by incubating the cleared samples with decreasing concentrations of fructose solution to prevent deformation. The restoration is also important for long-term storage of SeeDB-cleared samples. SeeDB -cleared samples is not suitable for permanent preservation in the clearing solutions due to the non-enzymatic browning issue mentioned in precious section (**Figure 7**). For long-term storage after imaging, it should be recovered to PBS and kept in 4^{o}C. After restoration, samples can be subjected to cryosectioning or whole-mount histochemistry.

To test for the compatibility of SeeDB method and immunohistochemistry, brain samples (P21) cleared with SeeDB or Sca*l*eA2 were recovered in PBS and then made into cryosections. *Thy1-YFP line G* mouse were used to evaluate the preservation of the fluorescent protein losses during the clearing and recovery. The intact brain samples were cleared with SeeDB (3 days) or Sca*l*eA2 (21 days). Then, they were recovered in PBS by reversing the procedure for SeeDB-cleared brains. Sca*l*eA2-treated samples were directly incubated with PBS. Brain samples cleared

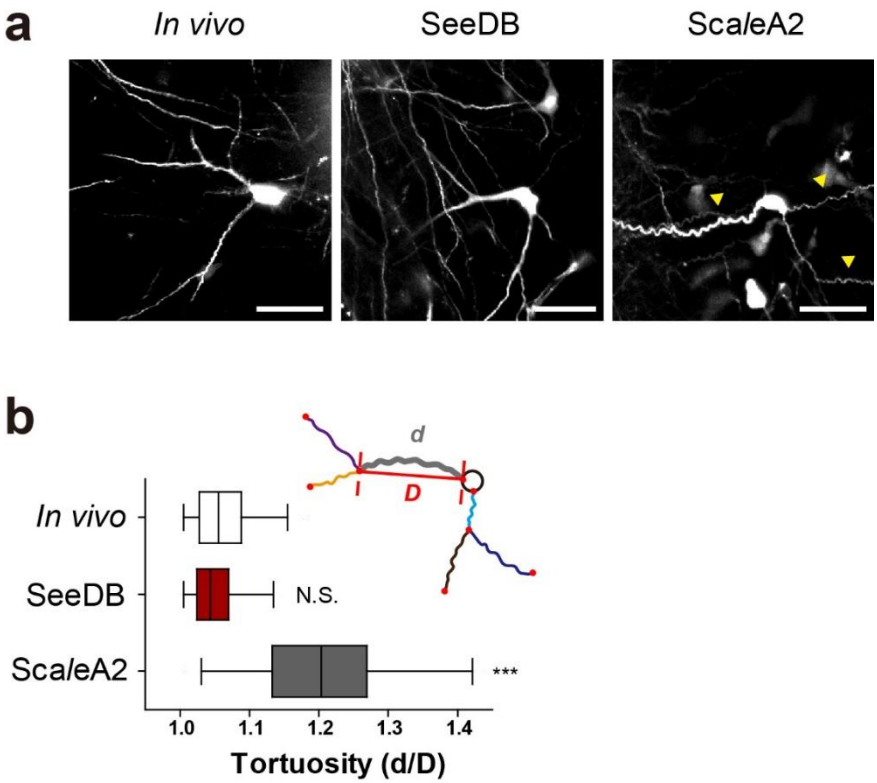

Figure 15. Morphological changes after optical clearing. (**a**) Somata and lateral dendrites of dextran tracer-labeled mitral cells in the olfactory bub before and after optical clearing using SeeDB (3 days) or Sca*l*eA2 (21 days). Small numbers of mitral cells in the olfactory bulb were labeled with dextran tracers. Somata and lateral dendrites of mitral cells were imaged. Whereas lateral dendrites *in vivo* and in SeeDB-treated samples had smooth appearance, those in Sca*l*eA2-treated samples appeared serrated (yellow arrowheads), suggesting morphological damage due to anisotropic sample volume changes. Scale bars represent 50 μm. (**b**) Quantification of dendrite deformation shown in (**a**). The ratio (*d*/*D*) was calculated as a tortuosity index. For each dendrite segment, the minimal distance between two ends (***D***) and length of actual trajectory (***d***) were determined Data are based on 93-167 dendrite segments from 35-46 neurons in 2-3 animals per group. Box plots represent lower quartile, median, and upper quartile. Bars indicate 5 percentile and 95 percentile. N.S., non-significant; *P**** < 0.001, compared with *in vivo* (One-tailed Mann-Whitney's U-test).

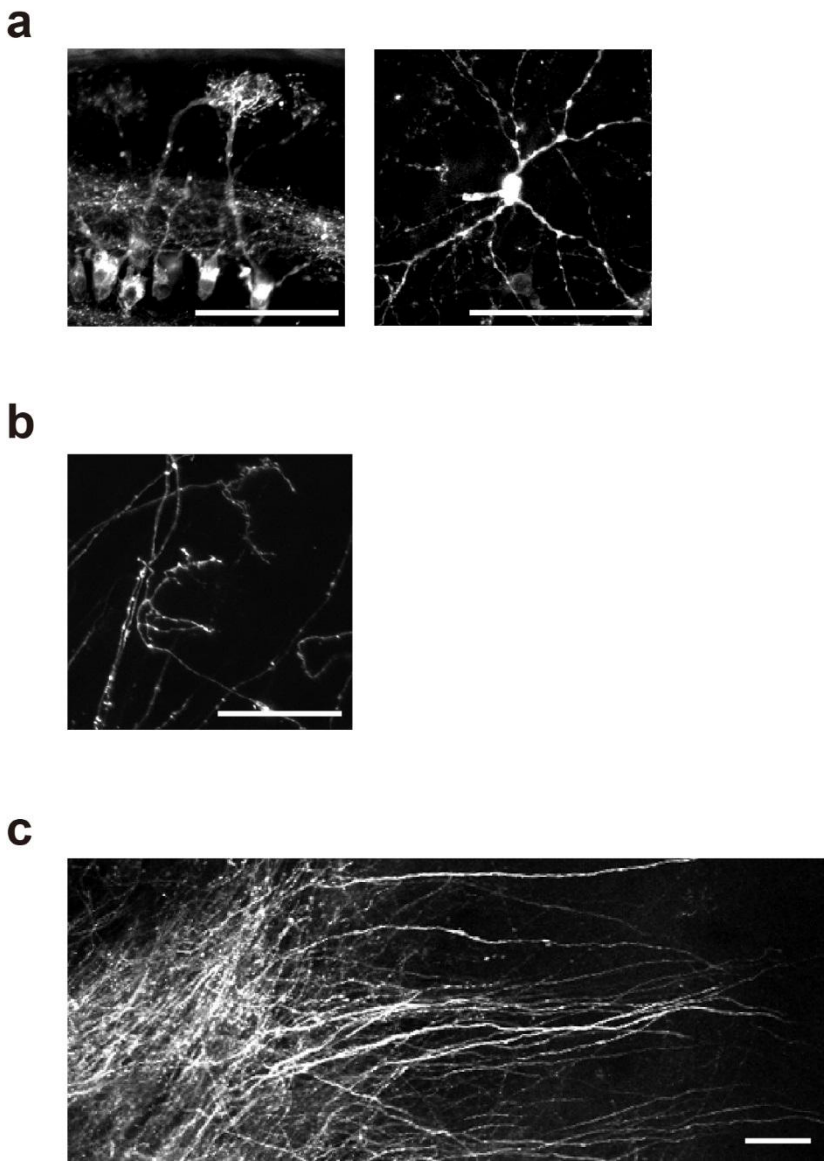

Figure 16. Confocal images of DiI labeled neurons. Whole-mount samples were used for imaging with a 20× objective lens (Olympus, UPLSAPO20X). Whole-brain samples were cleared using SeeDBp protocol. (**a**) Confocal stacked images of DiI-labeled mitral cells in the olfactory bulb (P5). Primary (left, 95 μm z-stack) and lateral (right, 30 μm z-stack) dendrites are shown. (**b**) Axons of olfactory sensory neurons (P7). (**c**) Mitral cell axons in the lateral olfactory tract (P7). Scale bars represent 100 μm.

with Sca*l*eA2 did not fully recover in size after 3-day incubation in PBS, as they remained ~110% of the original size and fragile (**Figure 6**), which made the sectioning very difficult. In contrast, the brains restored from SeeDB were able to fully recover and retain a firm structure. I then stained the sections with rabbit anti-Gephyrin (Abcam, ab25784), which is an inhibitory post-synaptic marker, or mouse anti-MAP2 (Sigma, M9942), which is a dendrite marker (**Figure 17**). Both antibodies recognized the fine structures on the neurons. Antigenicity was unchanged after clearing with SeeDB and subsequent retrieval in PBS. However, after clearing with Sca*l*eA2, artifactual globular staining was observed with anti-Gephyrin and no specific signals were observed with anti-MAP2. Possibly due to protein-losses during long optical clearing procedure in detergent-containing solution and conformational changes of epitopes, antigenicity was not fully preserved with Sca*l*eA2. From the EYFP signals, it is suggested that some of the fluorescent proteins were quenched or washed out during Sca*l*eA2 treatment. Therefore, stronger laser power was set to image EYFP in this sample. These results suggest that the conformations of cellular proteins are altered after Sca*l*eA2 treatment and recovery, but not seen in SeeDB treatment.

Whole-mount immunohistochemistry is a powerful technique for determining both the presence and the location of proteins within tissues [50]. Being able to examine the location of the signals three-dimensionally, whole-mount immunohistochemistry provides better interpretation of where proteins function. Due to the low penetration rate in whole-mount samples, the staining process can take weeks. Several methods have been reported to enhance the penetration efficiency in whole-mount immunostaining with the use of a common detergent, Triton X-100. For example, heating or shaking of the tissue, using enzymatic treatment (e.g., trypsin or proteinase K) to dissect the tissue, facilitate the penetration of the antibody [35].

I demonstrate an example of whole-mount staining in olfactory bulb. *OMP-GFP* knock-in mice was used for the staining. In this mouse line, GFPs are expressed specifically in mature olfactory sensory neurons. Olfactory sensory neurons expressing the same olfactory receptor are sorted together and converged on olfactory bulb forming spherical structures called glomerulus. *OMP-GFP* mice can be used to visualize the glomerular structures on the surface of the bulb. In order to penetrate the antibodies to the tissue, 1% Triton X-100 was added and the staining was performed on an overhead rotator. After immunostaining, dopaminergic short axon cells were labeled with anti-Tyrosine Hydroxylase antibody (anti-TH, Abcam, ab76442). The whole-mount sample was then cleared with SeeDB and imaged using confocal microscopy (**Figure 18**). With detergent and constant mixing, the tissue could be stained for a depth of 100-250 μm in mouse brain tissue after 4-day incubation of antibody.

In summary, because the minimal deformations occurred during the clearing process and high reversibility of SeeDB, this method is particularly advantageous for quantitative analyses of fine neuronal morphology and microcircuits. Many types of fluorescent probes are stably preserved in SeeDB, including: fluorescent proteins, dextrans or antibody-conjugated chemical dyes (e.g., Alexa Fluor Dyes), and lipophilic tracers (e.g., DiI). In addition, because the plasma membrane, epitopes, and ultrastructure remain intact during the SeeDB clearing, the restored samples are compatible with various histochemical procedures.

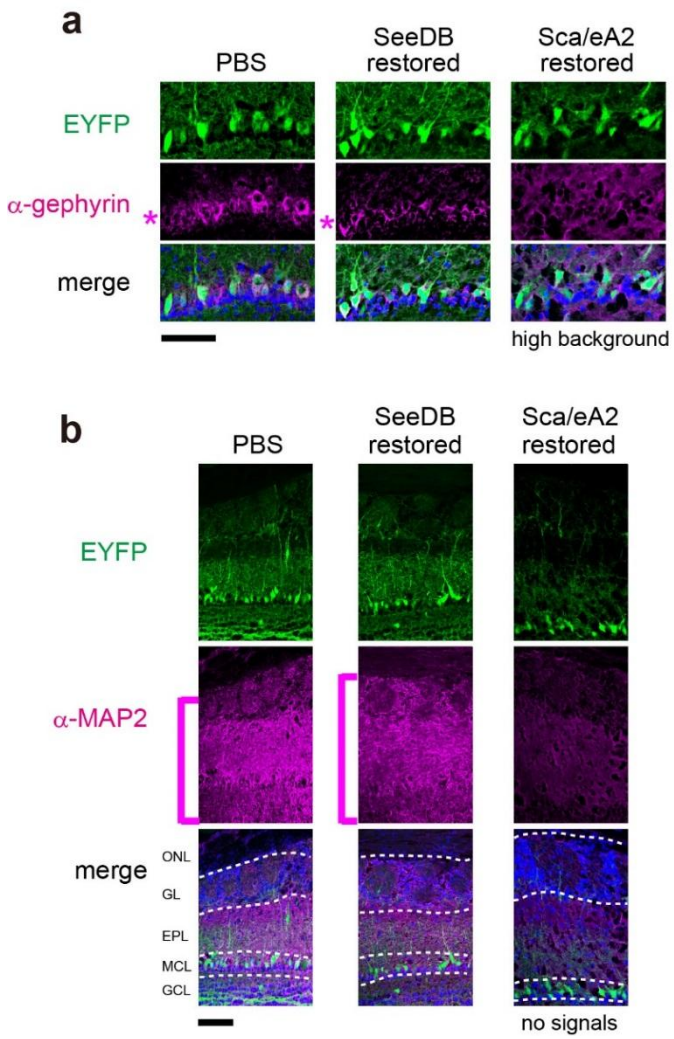

Figure 17. Compatibility with immunohistochemistry. Immunohistochemistry after optical clearing. Brain samples (P21) cleared with SeeDB or Sca*l*eA2 were recovered in PBS and then made into cryosections. (**a**) Cryosections were stained with rabbit anti-Gephyrin (Abcam, ab25784), which is an inhibitory post-synaptic marker. (**b**) Cryosections were stained with mouse anti-MAP2 (Sigma, M9942), which is a dendrite marker. For both antibodies, antigenicity was unchanged after clearing with SeeDB and retrieval. Whereas no specific signals were observed after clearing with Sca*l*eA2 and retrieval. Scale bars represent 20 μm. Abbreviations: ONL, olfactory nerve layer; GL, glomerular layer; EPL, external plexiform layer; MCL, mitral cell layer; GCL, granule cell layer.

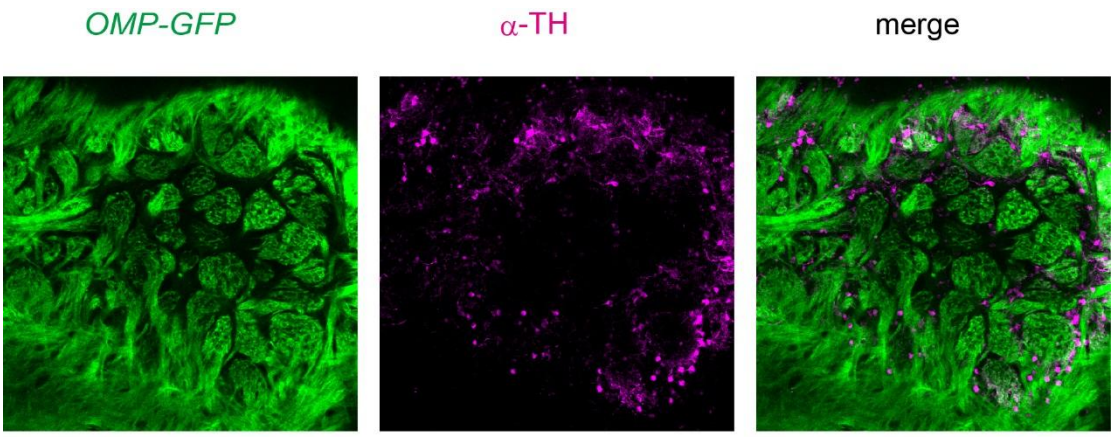

Figure 18. Optical clearing after whole-mount immunostaining. *OMP-GFP* knock-in mouse, which express GFP in olfactory sensory neurons, were used for immunostaining. Dopaminergic short axon cells were stained with anti-Tyrosine Hydroxylase (TH, Abcam, ab76442). After immunostaining, the whole-mount sample was cleared with SeeDB and imaged using confocal microscopy. A single confocal image at a depth of 75 μm (after calibration) from the surface. Scale bars, 100 μm.

3.4. Deep-tissue fluorescent imaging

Three-dimensional imaging of fluorescently labeled biological samples is difficult to achieve because of the sample opacity. In general, the laser beams and the fluorescence emission are unable to pass through tissue more than 100 μm thick. With recent advances in multiphoton imaging systems, infrared lasers enhance the penetration, achieving greater imaging depth than conventional confocal microscopy. Although previous optical clearing methods yield more clear images, the resolution and imaging depth for a fluorescent protein-labeled tissue have been restricted by the inability of the optical clearing agent to preserve the probes. In previous experiments, I demonstrated the fluorescent proteins were better preserved with SeeDB method (**Figure 14** and **17**). I next evaluated the maximum light-accessible depth in SeeDB-cleared samples by imaging fluorescence-labeled neurons using confocal and two-photon microscopy with the comparison of previously reported Sca*l*e method.

3.4.1. Confocal imaging

Confocal imaging is currently commonly used in observing fluorescently labeled samples. For high-resolution volumetric imaging, tissues should be cleared to allow laser excitation and emission for signal detection. In thick tissues, out-of-focus noises will interfere with signals emitting from the focal plane, resulting in blurred images. I compared optical clarity and fluorescence intensity for SeeDB-cleared (3 days) and Sca*l*eA2-treated (21 days) brain samples using confocal microscopy. For evaluating fluorescent protein intensity in whole-mount samples, an adult (P70) *Thy1-YFP line H* mice was fixed with 4% FPA and spilt into two hemispheres. One hemisphere was cleared with SeeDB, while the other was cleared with Sca*l*eA2. YFP-expressing brain samples were imaged using a 10× air objective lens (Olympus, UPLSAPO10X2, Numerical Aperture = 0.40, Working Distance = 3.1 mm) for three-dimensional

reconstructions (**Figure 19**). I obtained images in both samples from the surface of the cerebral cortex to the hippocampus, although the *apparent* depth (e.g., 1500 μm for SeeDB-cleared sample; 2600 μmm for Sca*l*eA2-cleared sample) of image was quite different between two samples due to refractive index differences and sample volume changes. Calibration for imaging depth is essential for compensating the misestimation from commercial objective lenses. When a commercial objective lens is used for imaging SeeDB or SeeDB37-cleared samples, there will be a refractive index difference between the immersion medium recommended by the manufacturer (air, water, glycerol, or oil) and that in the samples (SeeDB; refractive index 1.49). Hence the depth in the cleared specimen will be misestimated from the refractive index mismatch. In order to obtain the correct z position in the specimen, the *real* depth is calculated by multiplying the depth by n_{SeeDB} and then dividing by $n_{objective}$, where n represents refractive index. For example, when using water-immersion lens (refractive index 1.33), acquired *apparent* depth of 1,500 μm should be calibrated by multiplying 1.49 and then divided by 1.33 to obtain the *real* depth of 2,235 μm. The swelling of the sample should also be considered, from the quantification shown in Figure 8, because of the 150% linear expansion in Sca*l*eA2-treated (21 days) samples, the calibrated depth has to be divided by 1.5 to get the *real* depth. As a result, the *real* depth in the reconstructed images for SeeDB and Sca*l*eA2-cleared brains were both about 2.3 mm.

3.4.2. Two-photon imaging with commercial objective lens

In two-photon microscopy, excitation is generated by focusing pulsed infrared laser through the microscope optics. The laser beam is focused to increase the probability of two photons to simultaneously stimulate a single fluorophore. Because the laser focal point is the only location along the optical path where the photons are dense enough to generate two-photon excitation, out-of-focus absorption and photodamage are less seen than in a conventional confocal microscopy. More

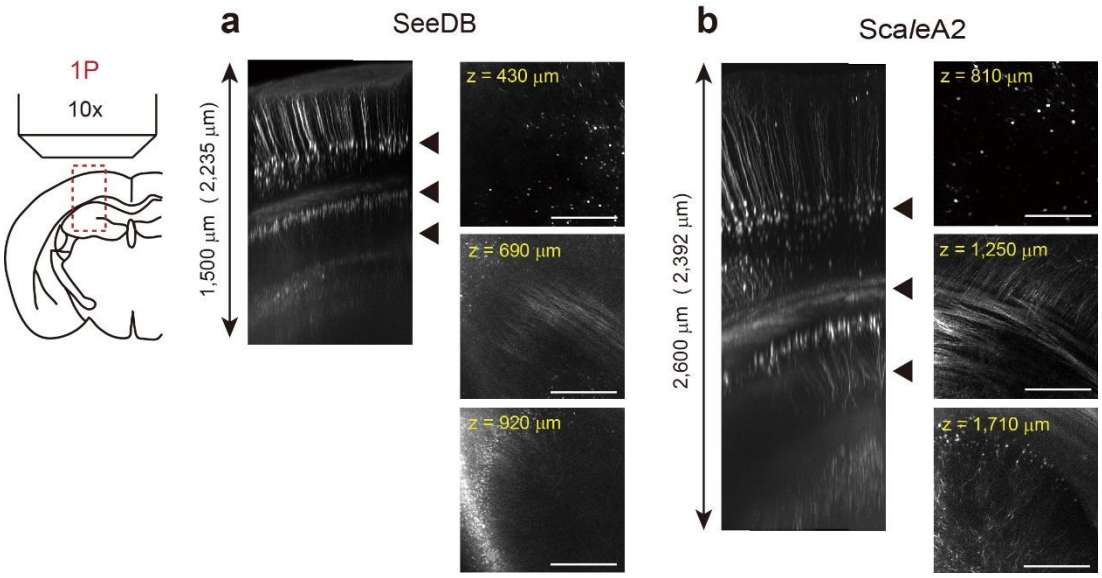

Figure 19. Fluorescence imaging of adult *Thy1-YFP-H* transgenic mouse brain. (**a, b**) Confocal imaging of mouse brain (P70) cleared with SeeDB (**a**) and Sca*l*eA2 (**b**). Confocal images were taken from the surface of the cerebral cortex to the hippocampus using a 10× air objective lens (Olympus, UPLSAPO10X2, NA=0.40, WD = 3.1 mm). Reconstructions along z-axis are shown on the left, and representative x-y images (indicated by arrowheads) are shown on the right. Because this objective lens is for non-immersion use (refractive index = 1.0), the axial scale is shortened in SeeDB (1.49) or Sca*l*eA2 (1.38) due to differences in refractive index. The *real* depth of the SeeDB-treated sample is 1,500 × 1.49 = 2,235 [μm]. Because Sca*l*eA2 induces ~150% linear expansion, the *real* depth of the Sca*l*eA2-treated sample is 2,600 / 1.5 × 1.38 = 2,390 [μm]. Calibrated *real* depth in samples is shown in parenthesis. The maximal imaging depth achieved by the confocal microscope was similar between SeeDB (**a**) and Sca*l*eA2 (**b**). Because EYFP signal intensity was weaker in Sca*l*eA2 samples, a stronger laser power was used to take the image in (**b**). Scale bars in (**a**) and (**b**) are 500μm.

importantly, infrared laser is less scattered. To obtain a comprehensive reconstruction from an intact sample, initially a 10× objective lens was used (Olympus, UMPLFLNW, 10XW, NA = 0.30, WD = 3.3 mm, water immersion). I imaged SeeDB-cleared mouse brain samples using two-photon microscopy to acquire images from YFP-expressing olfactory bulb (**Figure 20**). The olfactory secondary neurons, mitral cells are labeled with YFP in *Thy1-YFP line G* mice. The entire olfactory bulb was fully imaged from the medial side to cover the medial-lateral axis within the working distance (3.3 mm) of the objective lens. Then I generated a three-dimensional reconstruction (**Figure 20**, left) from 2×2 quadratic prisms.

Although 10x objective lens provides wide field imaging, low NA objective lens is not suitable to acquire bright and high resolution images. I next sought for a commercially available long-WD objective lens (Olympus, XLPLN25XSVMP, NA = 1.0, WD = 4.0 mm, designed for refractive index 1.38) for two-photon microscopy. With this 25× objective lens, SeeDB-cleared brains could be imaged up to a depths of approximately 4 mm (limited by WD) from the dorsal surface of the brain (**Figure 21**). In order to find the maximum accessible depth in SeeDB-cleared brains, another commercially available long-WD objective lens (Olympus, XLSLPLN25XSVMP, NA = 0.9, WD = 8.0 mm, designed for refractive index 1.38) was also applied to acquire deep-tissue imaging (**Figure 22**). With 8 mm working distance, I was able to image through the dorsoventral axis (6 mm in P21 animal) of a whole mouse cerebral cortex. However, these objective lenses are designed for the refractive index of water (RI~ 1.33) or Sca*l*eA2 (RI~ 1.38), as the z-plane went deeper, the image resolution and brightness was reduced in deep regions in SeeDB due to spherical aberrations.

3.4.2. Customized objective lens for SeeDB

To obtain high-resolution three-dimensional fluorescence images, achieving high transparency in the sample is not enough. The optic system should also be taken into

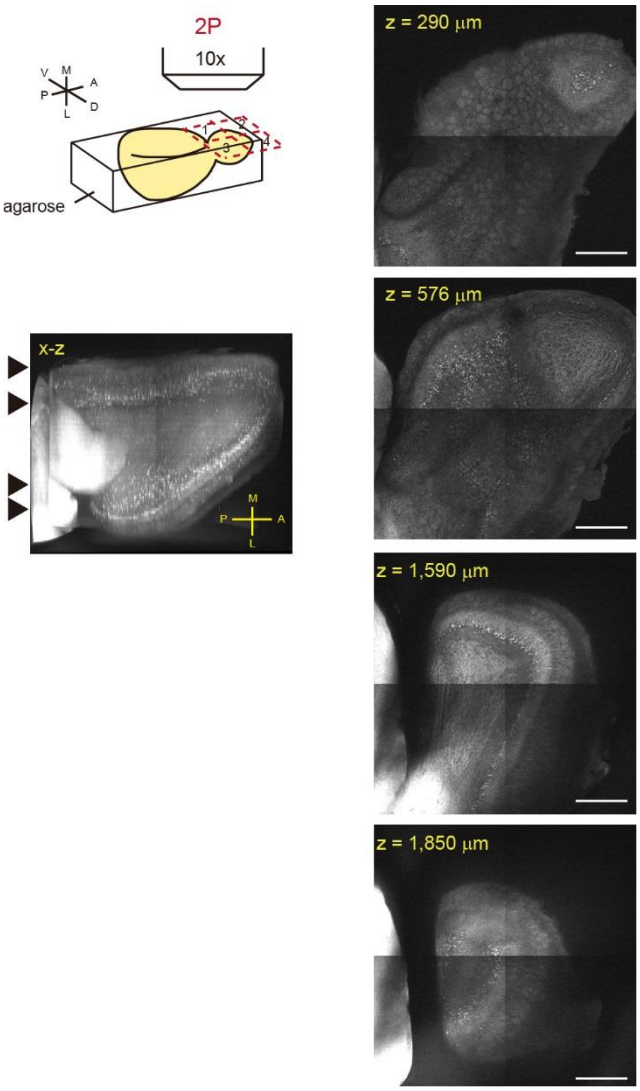

Figure 20. Imaging of the entire olfactory bulb using two-photon microscopy. Forebrain of *Thy1-YFP-G* mouse (P21) was cleared with SeeDB and imaged for the olfactory bulb from the medial side. In order to fix the imaging direction for the upright microscopy, we embedded the brain with 1% agarose, which did not interfere with two-photon excitation. Using a 10× objective lens (Olympus, UMPLFLN 10XW, NA = 0.30, WD = 3.3 mm, water immersion), the entire olfactory bulb could be included within 2×2 quadratic prisms. The images were then tiled for each z-plane to reconstruct the entire olfactory bulb (Left). Representative z-planes at the depth indicated by black arrow heads. Scale bars represent 500 μm. Abbreviations: A, anterior; P, posterior; M, medial; L, lateral.

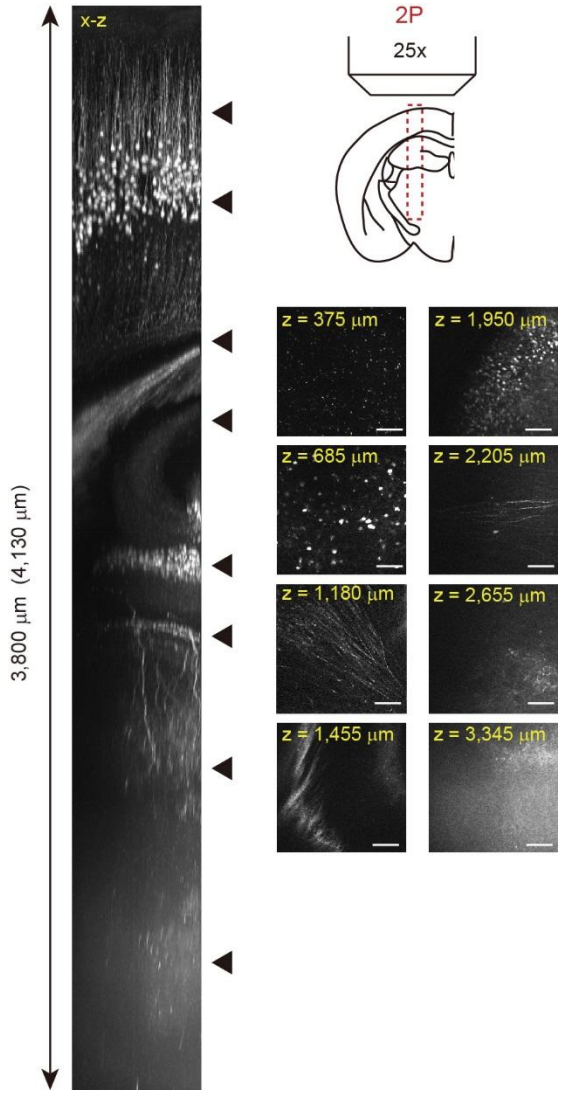

Figure 21. Adult hemi-brain samples (P70) cleared with SeeDB were imaged using a commercially available objective lens with long WD. A 25× objective lens (Olympus, XLPLN25XSVMP, NA = 1.0, WD = 4.0 mm, designed for refractive index 1.38) was used for two-photon microscopy. Imaging depth was limited by the WD. Spherical aberration caused by refractive index mismatch (1.38 of objective lens vs. 1.49 of SeeDB-cleared sample) decreases the brightness of the images. Scale bars represent 100 μm.

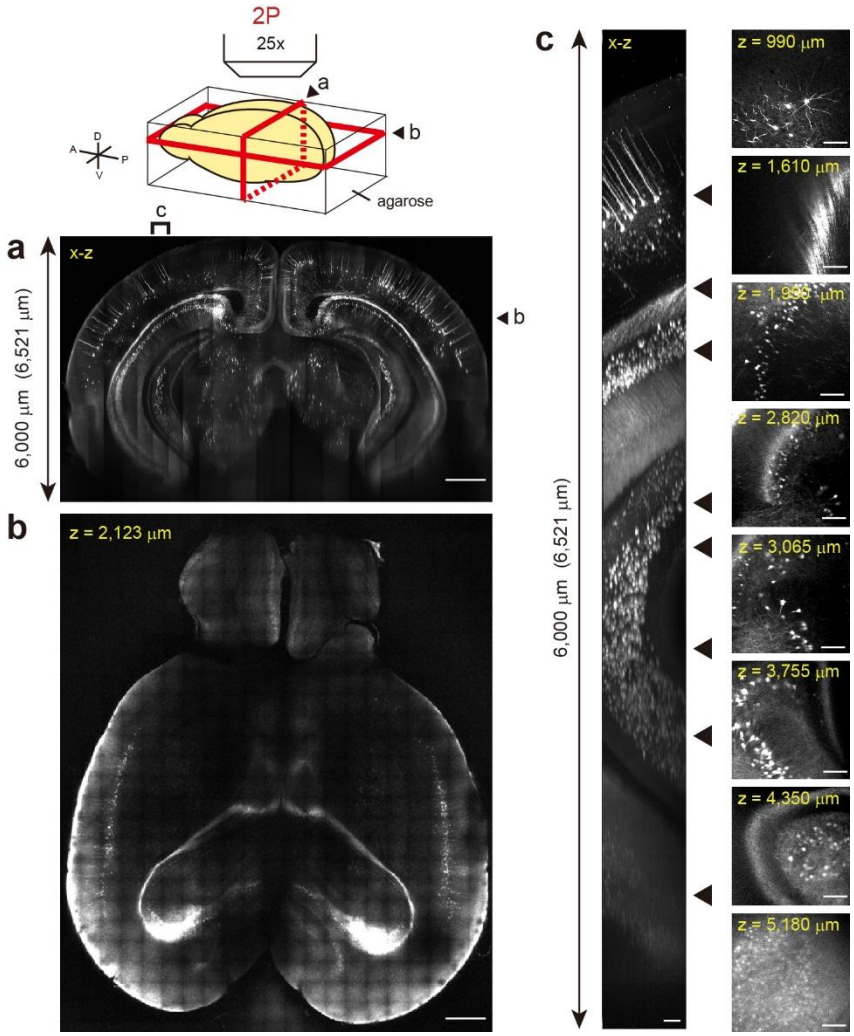

Figure 22. Two-photon imaging of P21 mouse forebrain. *Thy1-YFP-H* mouse was cleared with SeeDB37 and imaged using a commercially available long WD objective lens (Olympus, XLSLPLN25XSVMP, NA = 0.9, WD = 8.0 mm, designed for refractive index 1.38). Scale bars are 1 mm (**a, b**) and 100 µm (**c**). Abbreviations: A, anterior; P, posterior; D, dorsal; V, ventral.

consideration. One of the determinants of image quality in deep-tissue imaging is the type of objective lens used. As mentioned previously, objective lenses used in two-photon microscopy typically have a relatively short working distance of up to 2 mm, which limits the acquisition depth. However, use of a long WD objective lens does not mean images can be obtained as deep as WD permits. Major problem is spherical aberration. Spherical aberration is the failure of the objective lens to focus central and peripheral rays at the same focal point. If there is spherical aberration, the beam will scan with an enlarged, blurred spot (**Figure 23a**). Spherical aberration is also derived from the refractive indices of the immersion medium. Such problems have previously described in oil-immersion objective lenses and biological samples [51]. Mismatch should also be considered for imaging SeeDB-cleared samples. Spherical aberration affects interpretation and measurement of the specimen, thereby decreases image quality and fidelity. Commercial objective lenses designed for water immersion (RI~ 1.33) do not perform optimally with SeeDB-cleared samples (RI~ 1.49). To acquire deeper images at higher resolution, a customized long-WD objective lens (NA = 0.9, WD = 8 mm, RI = 1.48, correction collar covers 1.41-1.51) was ordered for achieving best performances under the high refractive index of SeeDB.

I evaluated the capability of the objective lens for the SeeDB-cleared samples with the point spread function (PSF) analysis. The PSF contains information about the spatial resolution geometry and is used as an indicator to identify problems with the objective lens or an optic system. The PSF is often measured using a fluorescent bead embedded in a gel that approximates an infinitely small point object in a homogeneous medium [33]. When the light travels though the objective lens, the immersion media, and the sample, the PSF provides an estimation for the deviations occurred in the light path from the resulted images. For the measurement, 0.5 μm fluorescent beads were used because in an ideal optical system, the lateral resolution

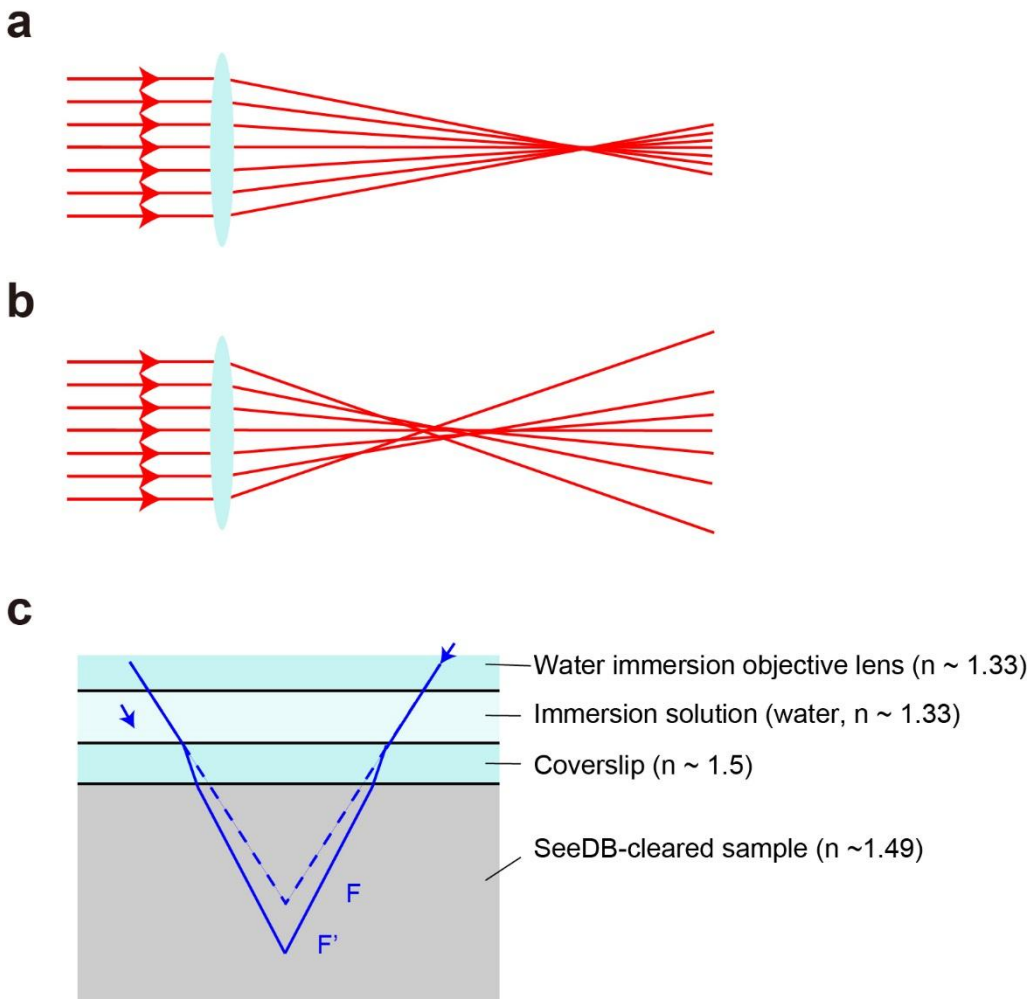

Figure 23. Spherical aberrations in optic system. (**a**) An ideal ray diagram without spherical aberration, all incoming rays focus to a point on the optic axis. (**b**) Ray diagram for spherical aberration. Light suffers from spherical aberration therefore, it does not converge to a clear focal point. (**c**) Spherical aberration originated from refractive index mismatch between objective lens and immersion solution. Dash lines indicate an ideal path for lights in refractive index-matched optic system. Solid lines indicate the light path affected by mismatch between water immersion objective lens (RI ~ 1.33) and SeeDB-cleared sample (RI ~ 1.49).

is given as:

$$\text{Lateral resolution (nm)} = \frac{0.51\,\lambda_{exc}}{\text{NA}}$$

Excitation wavelength used in two-photon microscopy is 920 nm, the NA of the customized objective lens is 0.9, hence the theoretical lateral resolution will be 0.52 μm. Thus, 0.5 μm fluorescent beads is sufficient to examine the PSF in this optic system. Fluorescent beads embedded in 1% agarose were equilibrated in SeeDB and imaged with 25× water-immersion, 25× scaleview-immersion, and our customized objective lenses from Olympus (**Figure 24**). I used 80% 2,2'-thiodiethanol (TDE) – 20% H_2O (v/v; refractive index 1.49) as immersion solution for customized objective lens. The PSF was acquired from the images of the beads at various depth, and then fitted with Gaussian model. The spatial resolution can be specified by the Full-Width-at-Half-Maximum (FWHM) value from the PSF. Figure 24a showed an example form the measurement of 25× water-immersion objective lens (Olympus, XLPLN25XWMP, NA = 1.05, WD = 2.0 mm). Resolutions along x- and z-axes gradually decreased as the depth increased due to spherical aberration. In addition to the water-immersion objective lens, we tested a 25× SCALEVIEW (Olympus, XLPLN25XSVMP, NA = 1.0, WD = 4.0 mm, designed for refractive index 1.38) and our customized 25× objective lens for SeeDB (Olympus, NA = 0.9, WD = 8.0 mm, designed for refractive index 1.48, correction collar covers 1.41-1.51) and summarized the resolution in graphic plot (**Figure 24b**). Resolutions decreased quickly in the deep regions when we used objective lenses designed for water or Sca*l*e immersion. In contrast, resolutions remained relatively constant when I used the customized objective lens designed for SeeDB. The matched refractive index of immersion and sample media makes spherical aberration independent of imaging depth. Hence, choosing a refractive index matched objective lens is important for deep-tissue imaging. It is also important to use the correction collar to minimize the spherical aberrations. Fine-structures were imaged with above objective lenses. At

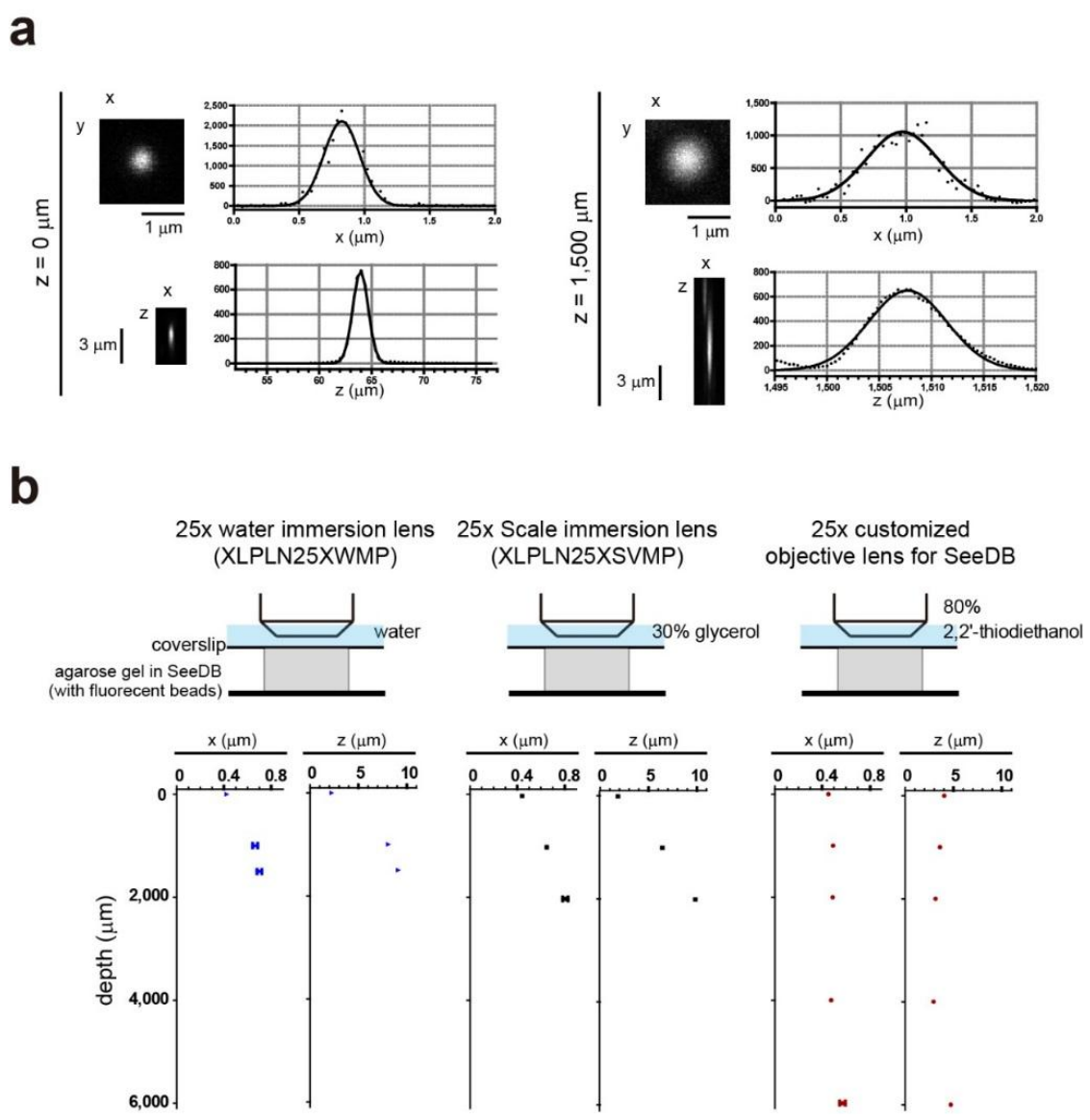
a
z = 0 μm
x
y
1 μm
x (μm)
x
z
3 μm
z (μm)
z = 1,500 μm
x
y
1 μm
x (μm)
x
z
3 μm
z (μm)
b
25x water immersion lens
(XLPLN25XWMP)
25x Scale immersion lens
(XLPLN25XSVMP)
25x customized
objective lens for SeeDB
coverslip
water
agarose gel in SeeDB
(with fluorecent beads)
30% glycerol
80%
2,2'-thiodiethanol
x (μm)
z (μm)
depth (μm)
0
2,000
4,000
6,000

Figure 24. Point-spread-function (PSF) analysis for image resolution in SeeDB-cleared samples. Fluorescent microspheres (diameter = 0.5 μm) embedded in 1% agarose and equilibrated in SeeDB were imaged. (**a**) Graphs show the representative data for a 25× water-immersion objective lens along x- or z- axes. (Olympus, XLPLN25XWMP, NA = 1.05, WD = 2.0 mm). Resolutions along x- and z-axes gradually decreased as the depth increased due to spherical aberration. (**b**) Summary of the results for 25× water-immersion, 25× scaleview (Olympus, XLPLN25XSVMP, NA = 1.0, WD = 4.0 mm, designed for refractive index 1.38), and our 25× customized objective lenses (Olympus, NA = 0.9, WD = 8.0 mm, designed for refractive index 1.48, correction collar covers 1.41-1.51). Immersion solutions were: water (refractive index 1.33) for XLPLN25XWMP, 30% glycerol (v/v, refractive index 1.38) for XLPLN25XSVMP, and 80% 2,2'-thiodiethanol (v/v, refractive index 1.49) for the customized objective lens. Data are full width at half maximum (FWHM). FWHM was given as 2.355 σ after Gaussian fitting. Resolutions decreased in the deep regions when we used objective lenses designed for water or Sca*l*e immersion. In contrast, resolutions remained relatively constant when we used our customized objective lens designed for SeeDB. Data are mean ± s.e.m. (n = 8-10 beads).

superficial area (depth less than 800 μm) 25× SCALEVIEW objective lens was able to image dendritic spines of layer V pyramidal neurons (**Figure 25**).

3.4.3. Brianwide imaging with two-photon microscopy

Using this customized objective lens, I was able to image SeeDB37-treated adult hemi-brain samples from the dorsal surface of the cerebral cortex to the bottom of the brain with two-photon microscopy (**Figure 26**). Images were brighter than that previously acquired with SCALEVIEW objective lens, thus achieved the full dorsalventral axis imaging in adult hemi-brains. Adult whole-brain was not imaged because clearing efficiency was limited. Despite spherical aberration and limited working distance, the commercial water-immersion objective lens still could be used for imaging down to 2 mm depth (**Figure 26a**).

Volumetric imaging of the entire mouse brain takes extremely long time and generates very large data volume. Within reasonable imaging time and data size, I imaged the hemi-brain sample along both coronal (**Figure 27**) and sagittal plane (**Figure 28**) and extended the xy plane to reconstruct the entire cortical network in the Thy1-YFP labeled adult brain. In order to reduce the imaging time, the depth gap was set as 300 μm and 500 μm for sagittal images from dorsal side and medial side, respectively. Images along the horizontal and sagittal plane were reconstructed for the hemi-brain. A representative plane for each data set was selected to demonstrate the efficiency and the fidelity of acquiring comprehensive picture from tiled multiple image blocks (**Figure 27b**, **28b**). Imaging and three-dimensional reconstruction for coronal plane from both dorsal and medial side were also examined. Although these reconstructions used only dozens of image blocks, the step size had been set small (e.g. 10-30 μm) to keep the reconstructed picture continuous along *xz* and *yz* plane (**Figure 27a**, **28a**). Pixels of the images had been minimized to reduce imaging time and the burdens in data processing.

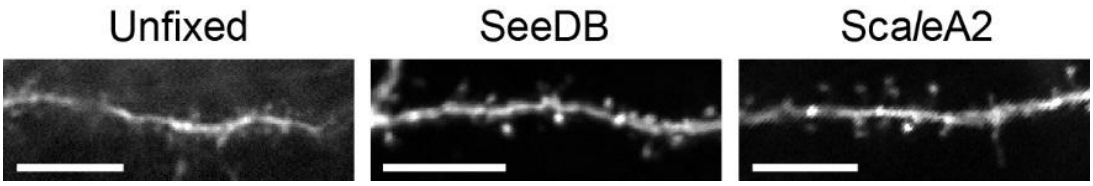

Figure 25. Two-photon images of dendritic spines imaged before and after optical clearing. Basal dendrites of layer V pyramidal neurons of *Thy1-YFP-H* mice were imaged. The mice was perfused with PBS and then imaged as an unfixed sample to present the dendritic morphology before optical clearing. To compare the optical clearing performances in SeeDB and Sca*l*e method, the mice were perfused and fixed with 4% PFA and then cleared with SeeDB (3 days) or Sca*l*eA2 (21 days) before imaging. A 25× objective lens (Olympus, XLPLN25XSVMP, NA = 1.0) was used to image at a depth of 700 μm (*real* depth). Scale bars represent 10 mm.

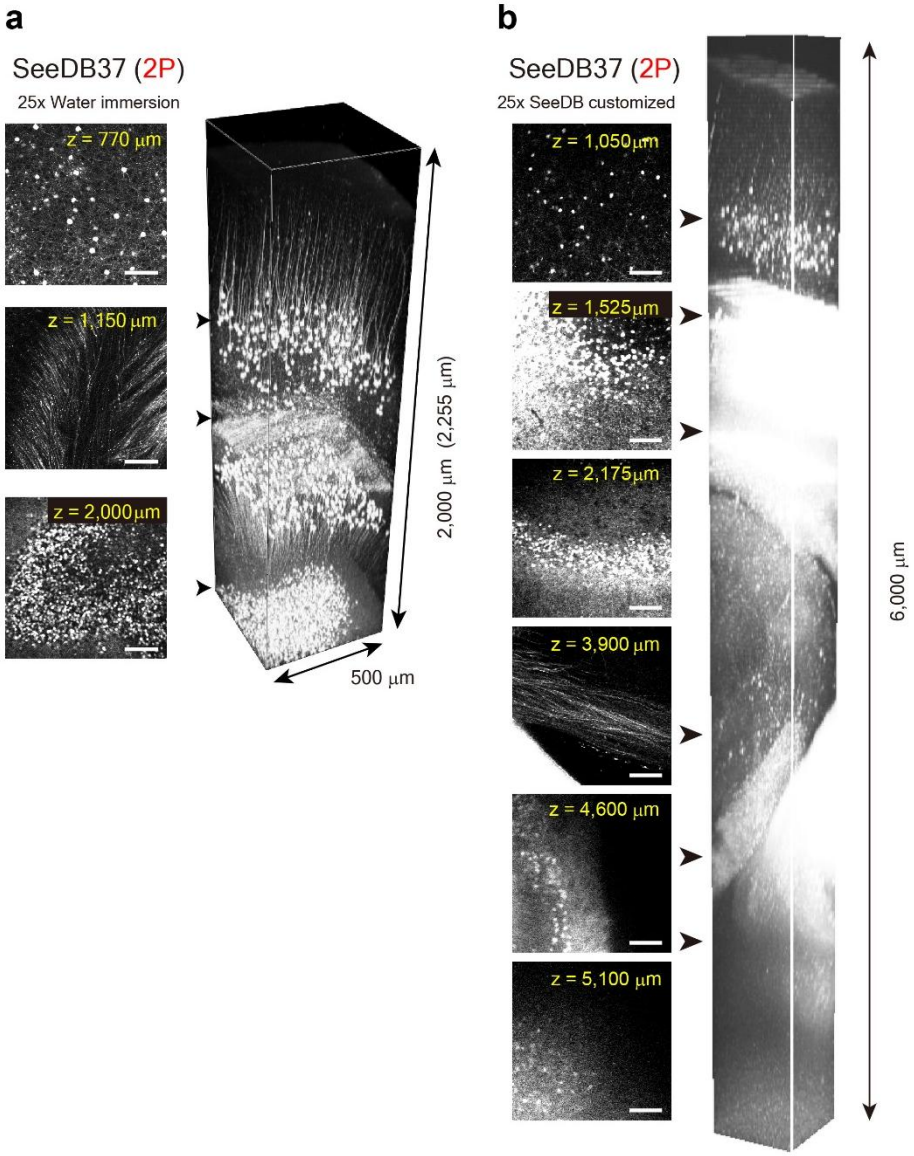

Figure 26. Fluorescence images of adult *Thy1-YFP-H* mouse, taken using two-photon microscopy. A hemi-brain sample is cleared using SeeDB37 protocol, and then imaged by two-photon microscopy with (**a**) 25x water immersion objective lens (Olympus, XLPLN25XWMP, NA = 1.05, WD = 2.0 mm) and (**b**) 25x SeeDB customized lens (Olympus, NA = 0.9, WD = 8.0 mm, designed for refractive index 1.48, correction collar covers 1.41-1.51).

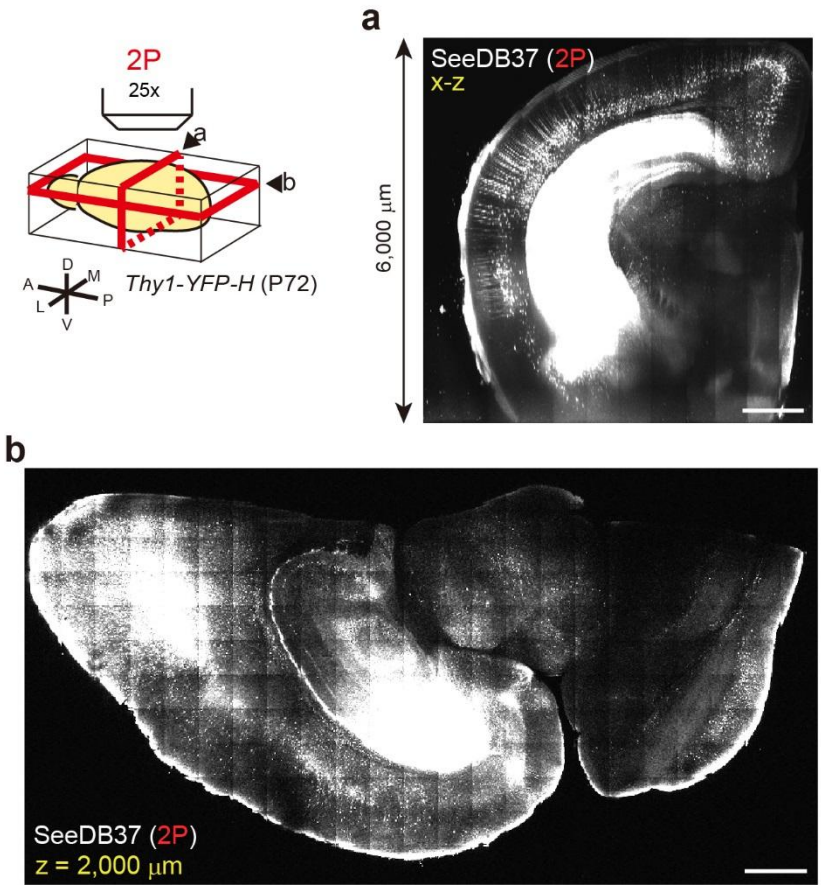

Figure 27. Two-photon images of adult *Thy1-YFP-H* hemi-brain (P72) taken from the dorsal surface. The sample was cleared with SeeDB37. (**a**) An optical section along a coronal plane (indicated in schema) was reconstructed from 12 × 1 blocks. (**b**) Images along a horizontal plane (indicated in schema, z = 2,000 μm from the surface) were tiled and stitched (23 × 12 tiles). Serial *xy* images (320 × 320 pixel) were taken at an interval of 25 μm. Scale bars represent 1 mm

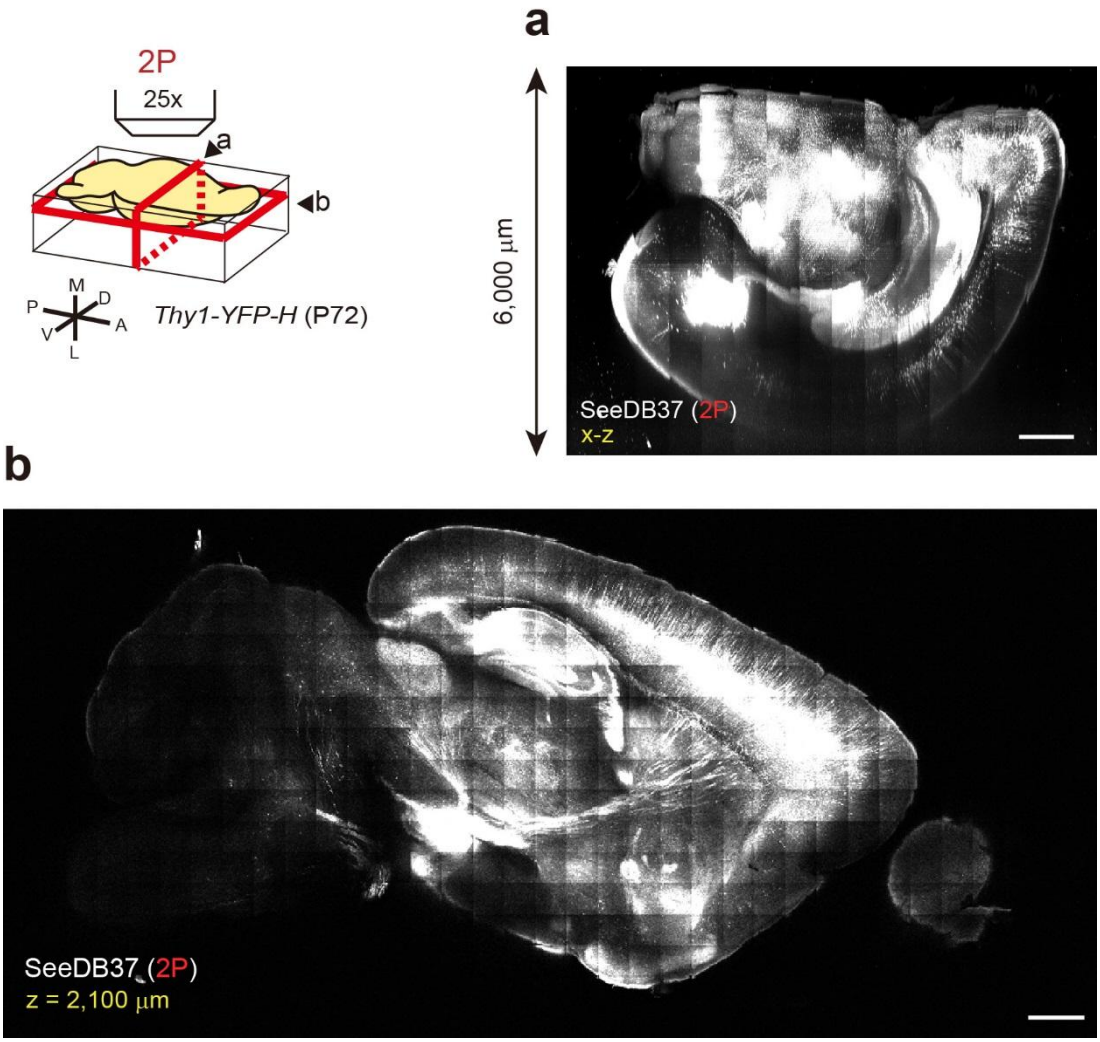

Figure 28. Two-photon images of adult *Thy1-YFP-H* hemi-brain (P72) taken from the medial side. The sample was cleared with SeeDB37. (**a**) An optical section along a coronal plane (indicated in schema) was reconstructed from 16 blocks. (**b**) Images along a sagittal plane (indicated in schema, z = 2,100 µm from the medial surface) were tiled and stitched (16 × 34 tiles). Scale bars represent 1 mm. Abbreviations: A, anterior; P, posterior; D, dorsal; V, ventral; M, medial; L, lateral.

Above imaging examples suggest that it is possible to generate a comprehensive picture for three-dimensional reconstruction from multiple image blocks; however, advanced data analysis and processing technique are also indispensable.

3.5. Reconstructing neuronal networks from whole-mount samples

3.5.1. Callosal projections in neonatal mouse brain

SeeDB can be a powerful tool for developmental studies of embryonic and neonatal brains because of the minimal fragility and morphological damages to tissues. *In utero* electroporation has been used to study developmental studies in the developing brain for a decade. Foreign gene can be introduced with electroporation of plasmid DNA into a mouse embryo [52,53]. It has been used not only for expressing fluorescent proteins, but also useful to overexpress or silence a specific gene [54]. Because genes can be introduced at an early stage in development, it is advantageous to use *in utero* electroporation to study early neural developmental (e.g., neurogenesis and neuronal migration [55]) or late developmental process (e.g., axon targeting and dendrite maturation).

An *in utero* electroporation-mediated gene transfer was used to unilaterally express EGFP in layer II/III cortical neurons (electroporated from the left side of the brain). High expression level of fluorescent proteins is essential for high resolution imaging and reliable neuronal tracing. Thus the fluorescent proteins were driven with CAG promoter to obtain strong fluorescence. Brain samples were fixed at P7 and then cleared with SeeDBp protocol. Images were acquired form whole-mount brains sample, and generated the Z-stack collapsed from 800-1800 μm depth of the sample **(Figure 28a**). Projections of EGFP-labeled callosal axons could be visualized after reconstructing 20 image blocks (5 x 4 tiles), Image stacks of maximum projection was presented in callosal axons extended through the corpus callosum, and project densely to a narrowly restricted region in the contralateral cortex. However, as this sample

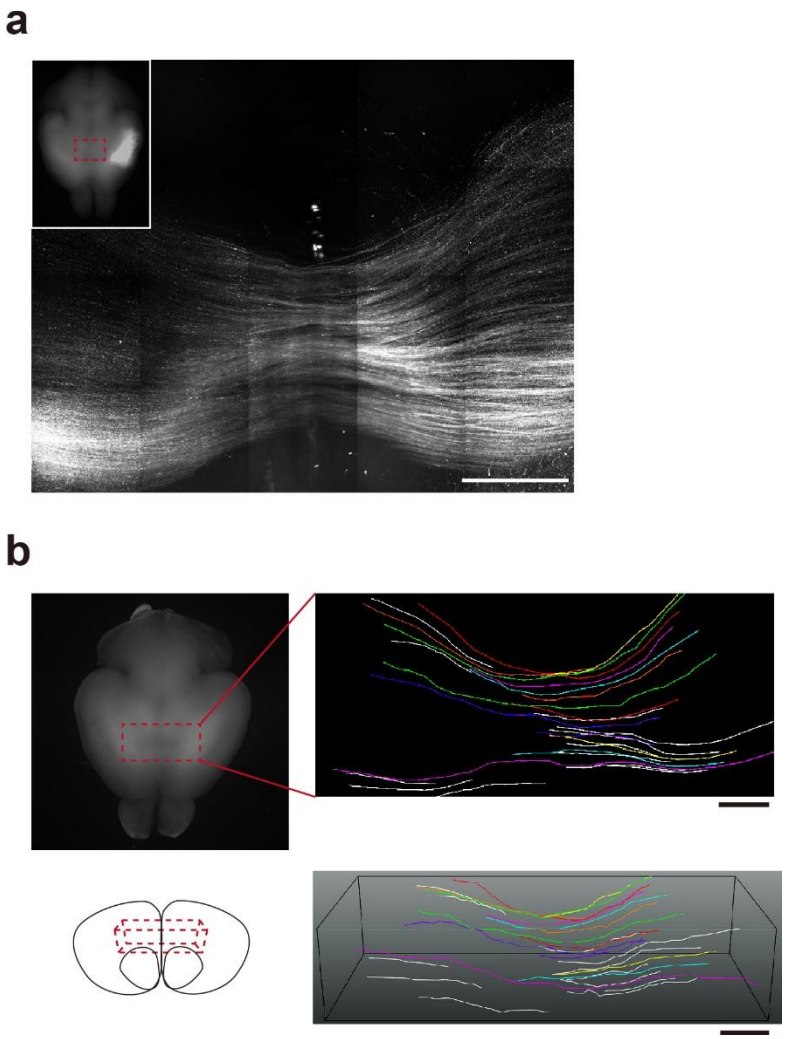

Figure 28. Topographic organization of callosal axon pathways revealed by *in utero* electroporation and optical clearing with SeeDBp protocol. (**a**) EGFP expression vector was electroporated into one hemisphere of the cerebral cortex at E15 and analyzed at P7. Z-stacked two-photon images (1,000 μm-thick, z = 800-1,800 μm from the surface of the cerebral cortex) taken with a 25× objective lens (Olympus, XLPLN25XSVMP) were tiled (5 × 4 tiles). Inset in top left corner shows the epifluorescence image of the brain, and the dashed red box indicates the area imaged. (**b**) Reconstruction of sparsely labeled callosal fibers. To label a small number of neurons, Cre-dependent tdTomato expression vectors were co-electroporated with a small amount of Cre expression vectors at E15. Z-stacked tiled image (9 × 4 tiles, z = 1500-2500 μm) taken with our customized 25× objective lens is shown. A frontal view of the reconstructed callosal fibers is shown on the bottom. Plasmids were electroporated to the left hemisphere of the brain (right in figures). Dashed red boxes indicate the area imaged. Scale bars represent 500 μm.

was densely labeled with a single color, it was difficult to identify individual axon in the three-dimensional reconstruction. To distinguish individual callosal axons, they have to be very sparsely labelled by fluorescent proteins. To sparsely label callosal axons, protein-based neuronal tracing, the Cre-loxP system was incorporated in the next analysis.

I examined the fine topographic organization within axonal pathways by sparsely labeling layer II/III neurons using the Cre-loxP system. With loxP sequences, the expression density of CAG-driven fluorescent proteins can be adjusted based on the amount of plasmids carrying Cre. By mixing the Cre-expressing and Cre-dependent fluorescent protein plasmids at different ratio, sparse labeling of layer II/III neurons could be achieved. Mice were fixed at P7 and subsequently cleared with SeeDBp protocol for two-photon imaging. Images were reconstructed from 36 image blocks (9 × 4 tiles) and manually traced. Single axon tracing revealed that the fine anterior-posterior layout of axons are largely, though not strictly, maintained during the course of axonal extensions across the corpus callosum (**Figure 28b**), consistent with studies in human. This result suggested that topographic callosal axon projection is ensured not only by the target-derived positional cues, but also by pre-target axon sorting [56].

Previously, tracing callosal axon projections needed a large number of sections and it has been difficult to acquire a comprehensive picture from separate sections. Obtaining a three-dimensional image from optically cleared intact brains can help understand the development and maintenance during the axon projection process. In combination with genetic manipulations, our methods should facilitate efforts to understand the molecular mechanisms underlying long-range axonal projection in the brain.

3.5.2. Mouse olfactory system

In the mouse olfactory system, olfactory sensory neurons expressing a given type of odorant receptor converge their axons to a pair of glomeruli in the olfactory bulb. Odor inputs to a single glomerulus are then relayed to 20-50 mitral and tufted cells through their primary dendrites. Each mitral/tufted cell has a single primary dendrite and several lateral dendrites. While primary dendrites of mitral/tufted cells receive inputs from a single glomerulus, lateral dendrites form reciprocal synapses with inhibitory granule cells and receive inputs from other glomerular modules and centrifugal fibers (**Figure 29c**). Sister mitral cells connecting to the same glomerulus receive common excitatory inputs due to electrical coupling and glutamate spill over within the glomerulus [57]; however, the extent of the diversity in the inhibitory modulations via lateral dendrites among sister mitral cells remains unknown [58]. Deciphering odor coding strategy by a single glomerular module is an important ongoing issue in the olfactory system.

SeeDB is ideal for comprehensive and quantitative reconstruction of microcircuits in the brain. To address the questions in mitral cells circuitry, SeeDB optical clearing was applied to acquire comprehensive images from intact mouse olfactory bulb for finding the anatomical bases for odor information processing in a single glomerular module.

To label neurons associated with a single glomerulus, we electroporated fluorescence-labeled dextran tracers into a single glomerulus on the dorsal surface of the olfactory bulb using a glass pipette [34]. *OMP-GFP* knock-in mice and/or *Thy1-YFP line G* transgenic mice were used to visualize glomerular structures and/or mitral cells [59,60]. After the optical clearing with SeeDB, the whole-mount olfactory bulb samples were imaged using confocal microscopy. A subsequent quantitative analysis was performed only when labeled mitral cells in a sample were all found to be associated with a single glomerulus. The distribution of sister mitral cell somata

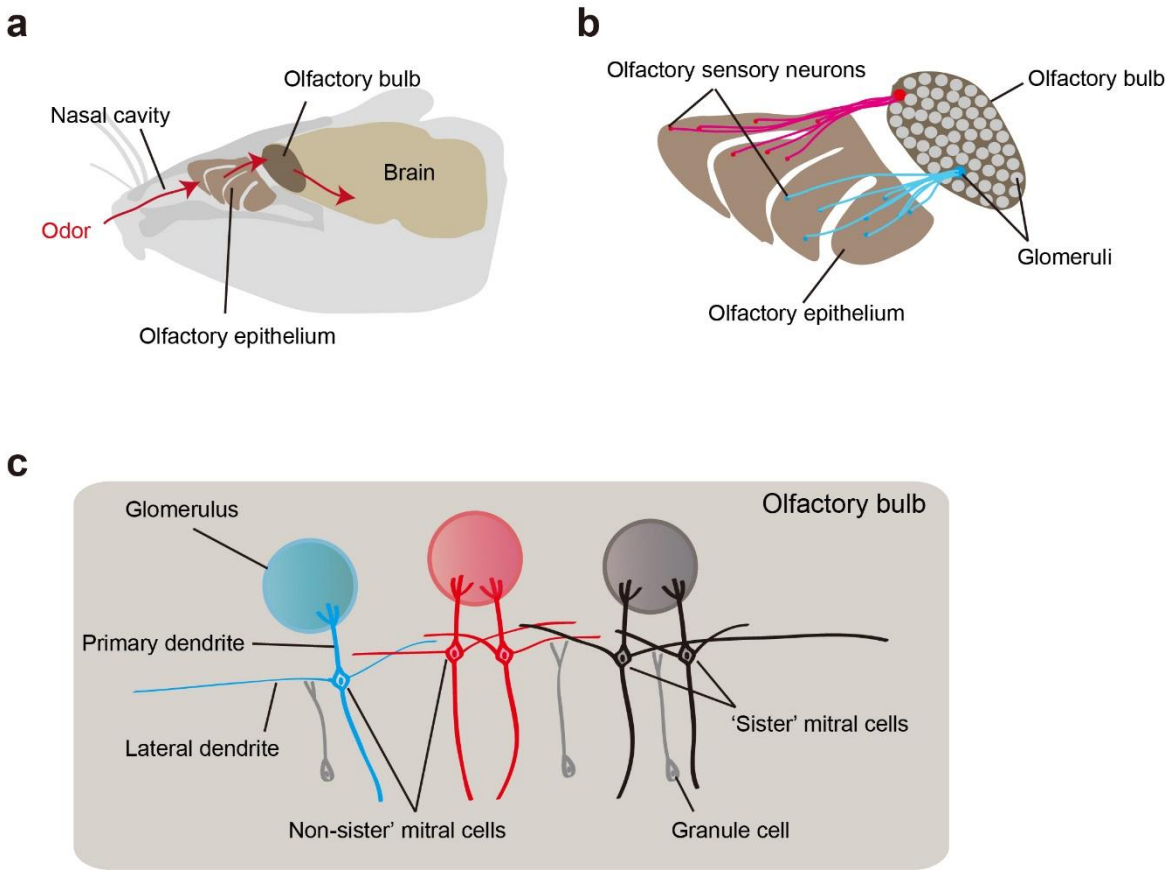

Figure 29. Schematic diagram for mouse olfactory system. (**a**) Relative position of olfactory epithelium, olfactory bulb, and the brain in mice. (**b**) Illustrations for the projection and convergence of olfactory sensory neuron axon terminals to the olfactory bulb. (**c**) Illustration for the cross section of an olfactory bulb. Glomeruli are spread on the surface of the olfactory bulb. Mitral cells are located in mitral cell layer ~ 200 mm beneath the glomerular layer. Specifically, mitral cells that extend their primary dendrite to the same glomerulus and receive the same input are named as 'sister' mitral cells. Granule cells contact with mitral cells mainly on lateral dendrites.

was first analyzed. Various types of neurons were labeled by the tracer, but the mitral cells were identified by the expression of *Thy1-YFP line G* transgene (**Figure 30a**). The tracer-labeled mitral cells were widespread in an area much larger than the size of a single glomerulus: sister mitral cells were distributed to 4-7× larger radius (n = 5 glomeruli) of the average radius of a glomerulus (37 ± 10 μm, mean ± s.d., n = 578 glomeruli from 3 animals at P21-28) (**Figure 29b, c**).

Next, I compared the lateral dendrite patterns among sister mitral cells. Because lateral dendrites are spread over a large area in the olfactory bulb, comprehensive reconstruction has been extremely laborious and difficult using the serial mechanical sectioning approach, even for a single neuron [61,62,63,64]. The whole-mount olfactory bulb sample was too thick even with two-photon microscopy [65,66], but after optical clearing of this sample with SeeDB, I could visualize the near complete wiring diagram of mitral cell dendrites using confocal microscopy (**Figure 31**). *OMP-GFP* mice were used rather than *Thy1-YFP-G* line. Because glomeruli are labeled with GFP *OMP-GFP* mice, which helped the identification of the position of target glomerulus during *in vivo* tracer injection and specified the tracing from single glomerulus. After tracer injection, not restricted in sister mitral cells, cells extend their axons or dendrites (e.g., tufted cells, periglumerular cells) to the injected glomerulus were electroporated with tracer dye. For this reason, mitral cells were identified based on anatomical traits. Neurons that have relatively large somata (diameter = 10-20 μm) and located in the presumptive mitral cell layer were designated as mitral cells. From these criteria, external and middle tufted cells were excluded; however, internal tufted cells located close to the mitral cell layer may be included in the data set. Among the cells designated as mitral cells, only those strongly labeled and allowed for full tracing (e.g., >80% of lateral dendrites that were fully traced, some tracing were interrupted by saturated signals or noise) of lateral dendrites were incorporated into the data set.

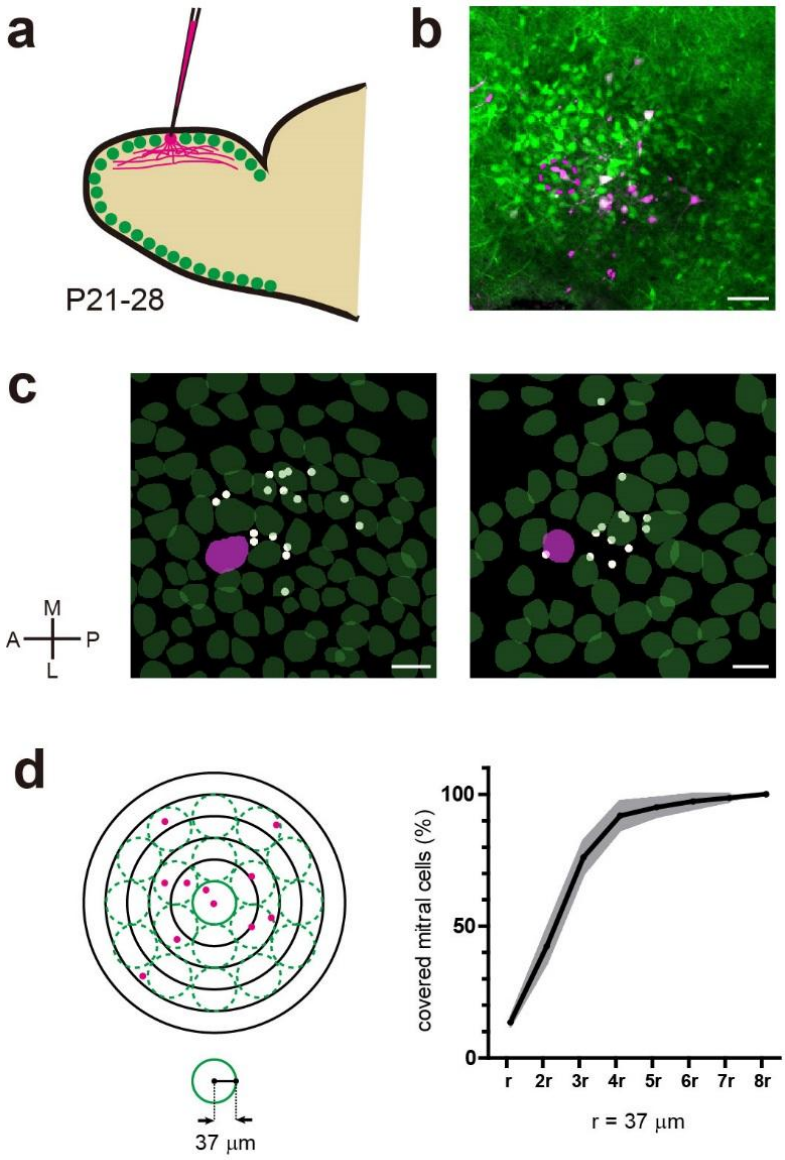
a
P21-28
b
c
M
A
P
L
d
37 μm
covered mitral cells (%)
100
50
0
r
2r
3r
4r
5r
6r
7r
8r
r = 37 μm

Figure 30. Distribution of mitral cell somata labeled from a single glomerulus. Whole-mount olfactory bulbs were imaged from dorsal surface using confocal microscopy. (**a**) Neurons associated with a single glomerulus were labeled by electroporation of Alexa 647-dextran tracer *in vivo*. Location of dye-injected glomerulus is shown by a magenta broken line. Olfactory bulb samples were then dissected and cleared with SeeDB. Confocal images were taken with a 10× air objective lens (Olympus, UPLSAPO10X2). (**b**) EYFP expression in *Thy1-YFP-G* transgenic mice was used to identify mitral cells in the olfactory bulb. In this mouse line, EYFP is expressed in mitral cells, but not in tufted cells. Neurons co-labeled with dextran and EYFP were defined as "sister mitral cells" associated with the targeted glomerulus. A confocal image of the mitral cell layer is shown. (**c**) Distribution of sister mitral cell somata (z-projected images). Glomeruli in the dorsal olfactory bulb were analyzed. Two representative examples out of 5 datasets are shown. Glomeruli are in green. Targeted glomerulus is in magenta and labeled mitral cells are shown as gray dots. (**d**) Cumulative curve of sister mitral cell distribution from the centroid of these neurons (n = 5 glomeruli, number of sister mitral cells were 15.8 ± 4.3, mean ± s.d). Approximately 80% of sister mitral cells were distributed within radius equivalent to 3 times the radius of the glomerulus (37 ± 10 μm, mean ± s.d., n = 578 glomeruli from 3 animals, age P21-28); distribution of 100% of sister mitral cells were found within radius equal to 4-7 times the radius of the glomerulus (n = 5 glomeruli from 5 animals, age P21-28). Thus, mitral cells that belong to a given glomerulus are highly intermingled with those of other glomeruli. Scale bars represent 100 μm. Abbreviations: A, anterior; P, posterior; M, medial; L, lateral.

Based on these tracing data, I quantified various parameters of mitral cell dendrites. The dendrite coverage area of a mitral cell was defined as the distribution area of granule cells (major inhibitory neurons that form synapses with lateral dendrites) that can potentially form synapses with a given mitral cell. Typical granule cells extend their apical dendrites within radius of 25-100 μm in mice [67,68]. Therefore, I defined the coverage area for a mitral cell as the area within 100-μm distance from the mitral cell dendrites. Coverage area of 13 sister mitral cells were determined based on z-projected images (**Figure 31b**), and the overlapping percentage of each pair of sister mitral cells was subsequently calculated from the overlapped area. Representative overlapping of sister mitral cells was given in Figure 31c with #1 and #10 mitral cell. Under this assumption, I found that coverage areas of sister mitral cells only have small overlapping areas (mean± s.d.: 37 ± 30%, n = 144 pairs) (**Figure 31b**, **Table 4**). As these coverage areas are maximum estimates, they are likely overestimated: many granule cells extend dendrites to smaller areas (< 100 μm), not all granule cells form synapses with lateral dendrites passing through this area, and functional synapses seem to be more localized [68,69]. Thus, my results support the idea that synaptic partners are highly diverse among sister mitral cells. (**Figure 32**)

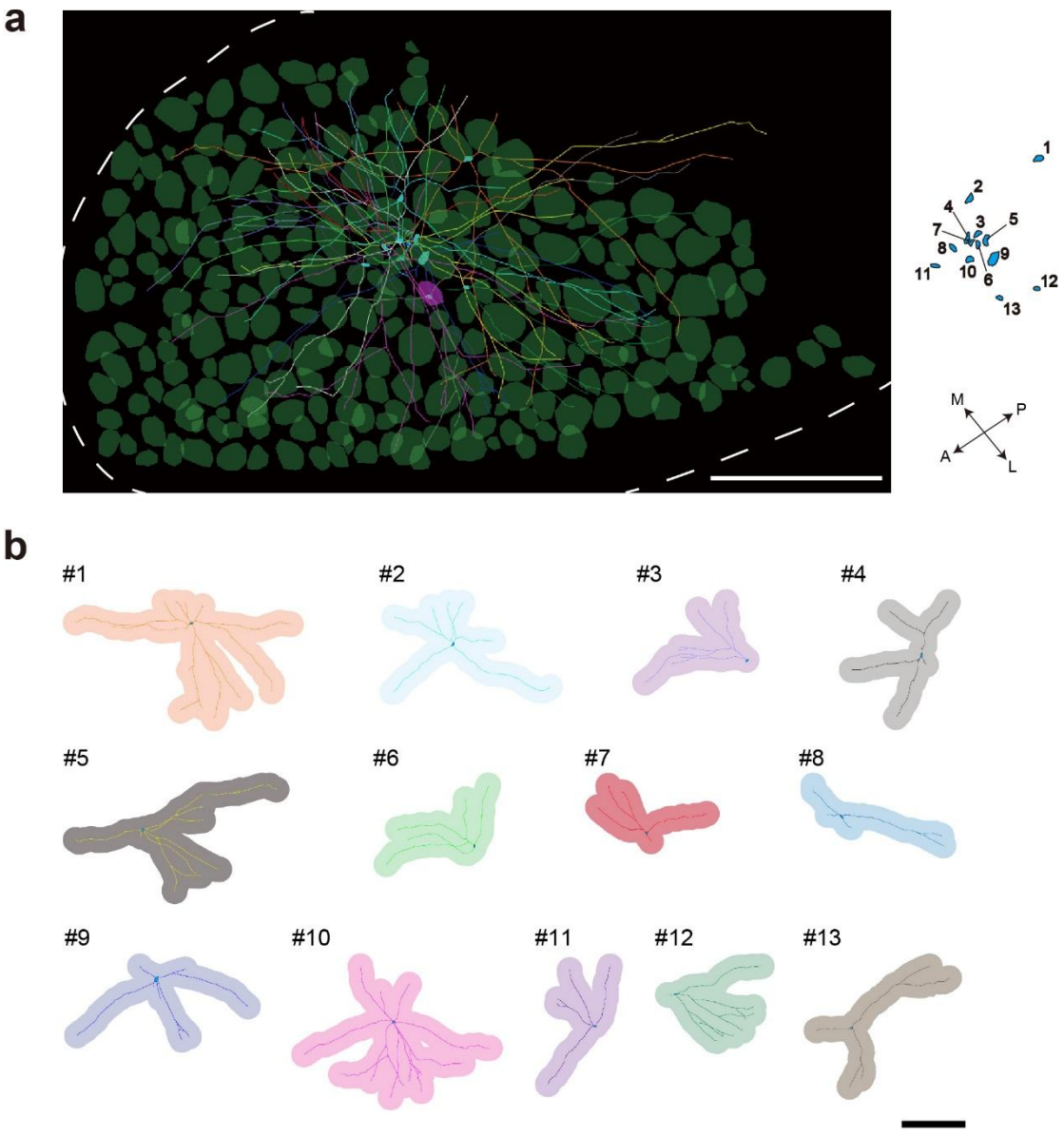
a
1
2
4
3
5
7
8
9
11
10
6
12
13
M
P
A
L
b
#1
#2
#3
#4
#5
#6
#7
#8
#9
#10
#11
#12
#13
c
1
10

Figure 31. Tracing lateral dendrites of sister mitral cells. (**a**) Representative data from Alexa 647 dextran-labeled *OMP-GFP* knock-in mice (P21-28), showing the distribution of lateral dendrites of sister mitral cells (primary dendrites and axons are not shown). Intact mouse olfactory bulb was imaged with confocal microscopy with a 10× air objective lens (Olympus, UPLSAPO10X2). Lateral dendrite reconstruction was based on optical sections spanning a thickness of 400 μm (in *real* sample). All these neurons project primary dendrites to a single glomerulus shown in magenta; other glomeruli were identified by EGFP fluorescence of *OMP-GFP* mice. Cells located their cell bodies close to the mitral cell layer with diameter lager than 10 -20 μm were reconstructed. Total 14 neurons were reconstructed and shown in different colors. (**b**) Coverage areas of 13 mitral cells in (**a**). Estimated overlapping percentages in dendrite coverage areas among sister mitral cells. The major inhibitory neurons that form synapses with lateral dendrites are granule cells. Thus, dendrite coverage area of a mitral cell was defined as the distribution area of granule cells that can potentially form synapses with a given mitral cell. Because typical granule cells extend their apical dendrites within radius of 25-100 μm in mice, the coverage area was defined to be within a 100-μm distance from the traced dendrites of the mitral cells. (**c**) An example showing the overlap in coverage areas of two mitral cells, #1 and #10. Coverage area of mitral cells #1 has a 44% overlap with that of mitral cells #10. The labeled glomerulus is shown by a dotted line. Coverage area of 13 sister mitral cells in were determined based on z-projected images shown in (**b**). Percentages of shared coverage areas were determined for all pairs of sister mitral cells and were 37 ± 20 % (mean ± s.d., n = 144 pairs). Scale bars represent 500 μm. Abbreviations: A, anterior; P, posterior; M, medial; L, lateral.

Table 4. Percentages of overlapping areas of 13 sister mitral cells shown in Figure 31. Overlapping percentage was determined based on z-projected images shown in Figure 31b. Percentages of shared coverage areas were determined for all pairs of sister mitral cells and were 37 ± 20 % (mean ± s.d., n = 144 pairs).

		Overlapping mitral cell (% overlapping area)													
	Mitral cell number		**1**	**2**	**3**	**4**	**5**	**6**	**7**	**8**	**9**	**10**	**11**	**12**	**13**
		1		39	14	17	47	22	23	22	28	44	15	33	30
		2	60		34	36	50	44	40	37	41	71	46	30	21
		3	33	52		45	22	71	53	29	12	44	55	0	0
		4	38	52	42		37	6	39	25	26	81	48	2	16
		5	66	45	13	23		20	25	28	39	55	13	37	41
		6	46	61	64	58	31		45	31	18	52	55	1	6
		7	66	74	63	49	51	60		46	30	61	60	4	29
		8	66	72	37	34	60	43	48		73	82	39	48	24
81-100		**9**	52	50	10	22	51	16	20	45		71	32	39	41
61-80		**10**	45	48	19	37	40	25	22	28	39		28	27	25
41-60		**11**	36	71	55	51	22	61	50	31	41	65		0	11
21-40		**12**	68	40	0	2	55	1	3	33	43	55	0		21
0-20		**13**	65	30	0	15	63	7	22	17	48	53	10	22	

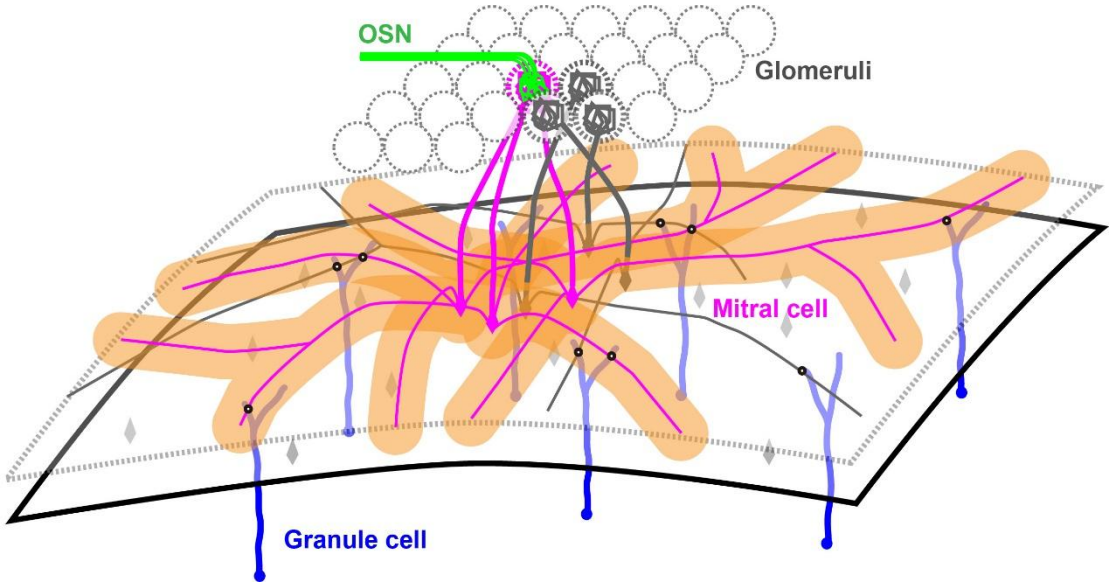

Figure 32. Wiring specificity of sister mitral cells in the olfactory bulb. Somata of 'sister' mitral cells (magenta) are intermingled with non-sister mitral cells (gray). Majority of granule cells (blue) are not shared among sister mitral cells. Thus, sister mitral cells are likely differentially tuned by inhibitory granule cells.

Discussions

4.1. Comparison of SeeDB with other tissue-clearing techniques

Optical clearing techniques have a potential to reduce optical scattering while retaining the spatial resolution in the intact thick samples. Optical clearing agents have been developed and widely used for years with many imaging applications. Factors affecting light scattering in tissues are complicated. One of the solutions to reduce the light scattering in biological tissues is to alter the optical properties by high refractive index agents. Previous experiments have shown that administration of high refractive index solution to the tissue can increase tissue transparency, thereby increasing the ability of light penetration through the tissue. However, factors governing the efficacy of an optical clearing agent are complex, and not simply depend on the refractive index.

Optical clearing of biological samples by organic solvents that matches the refractive index has been a popular strategy for decades, in which biological samples are made transparent by excluding the low-refractive-index interstitial fluids by alcohols then soaking in high refractive index optical clearing agent. Owing to dehydration and organic solvents, samples preparations are permanently changed; for instance, the cell membranes are dissolved and washed out during optical clearing. Besides, dehydration-related morphological changes and the deformations are disadvantages for reliable tracing of the connectivity in neuronal circuits. For this reason, the applications of these organic solvent-based optical clearing agents are limited.

To address this issue, water-based optical clearing agents have been developed. FocusClear was first proposed as a water-based clearing agent, however, the application has been limited to small samples with thickness less than 500 μm. Recently, Sca*l*e method used a mixture of urea, detergent, and glycerol to render the

structure of the biological sample transparent. Although Sca*l*e method preserves more fluorescent signals, myelin-rich white matter regions remain opaque after week-long incubation, and also resulted in irreversible sample expansions (**Figure 9** and **10**). In this thesis, a simple and efficient technique for clearing mammalian brain tissue is proposed. Unlike organic solvent-based immersion solutions, water-based SeeDB allowed preservation of fluorescent proteins. Compared with other aqueous reagents, such as FocusClear, 60% sucrose and Sca*l*e method, SeeDB method not only preserves more fluorescent signal (**Figure 14**), but also retains more constant sample volume. In FocusClear and 60% sucrose, samples subject to ~20% shrinkage. On the other hand, Sca*l*eA2 caused 150% expansion due to chemical rendering in the clearing procedures (**Figure 8**). In SeeDB method, I used serial incubation (e.g., gradually match the refractive index of scatters with that of samples with 20%, 40%, 60%, 80%, 100%, and SeeDB) combined with time control to minimalize tissue expansion/shrinkage problems. Invariant sample volume in SeeDB method also minimized morphological distortions and fragility to tissues while maintaining a comparable level of clarity (Figure **15**).

Another advantage in SeeDB method was its capability in large-scale imaging. Fluorescence imaging of SeeDB-cleared brain samples indicated that SeeDB method is superior to other described clearing agents for performing detailed three-dimensional brain reconstructions at both fine and macro scales (**Figure 25**-**27**). Acquiring volumetric images from intact brain samples takes long time. Sca*l*eA2-treated adult brain samples, the sample's dorsoventral thickness exceeded WD of available objective lenses (8 mm) and therefore could not be imaged in its entirety. However, the dorsoventral thickness of a mouse brain cleared with SeeDB method can be fully covered with 8 mm WD because of no significant swelling.

To broaden the usage of SeeDB, I modified the protocol according to the nature

of the samples (**Figure 13**). For neonatal brain samples, a modified protocol, SeeDBp is developed. PBS is introduced to adjust osmotic pressure of the solutions to preserve tissue volume and integrity. For adult brains with highly myelinated structures, SeeDB37 and SeeDB37ht protocols are proposed. In these alternative protocols, higher temperature condition and a more concentrated fructose solution, SeeDB37 are used in the final step. The penetration of fructose is crucial to equilibriate the refractive index. I took an advantage of the increased fluidity at high temperature condition to clear these difficult samples. However, for better optical clearing efficiency, I found that trimming or slicing the tissue to the minimum size is required. Whole brain can be cleared for mice up to P21. For the adult mouse, a half brain is the maximum size that can be efficiently cleared with SeeDB or SeeDB37. The formula for SeeDB method is simple, cheap, and requires no special instruments, allowing for highly reproducibility for regular laboratory usages.

A drawback of SeeDB is the limited penetration of probes in whole-mount samples, although immunohistochemistry with cryosections could be achieved for samples recovered from SeeDB treatment (**Figure 17**). Even if the tissue were permeabilized with Triton X-100, antibodies could only penetrate to a depth of 100-250 μm in the adult mouse brain (**Figure 18**). Similarly, the penetration of chemical dyes for counterstaining (e.g., DAPI) was also limited in SeeDB. A recently developed clearing technique, CLARITY, is more advantageous for antibody staining of thick samples. CLARITY is a chemical transformation of tissue that creates a stable tissue-hydrogel hybrid. The tissue components (e.g., DNA, proteins) are at their physiological location by the hydrogel network after removal of lipids and exogenous scatters within the tissue. Lipids that cause light scattering are solubilized with ionic detergents and then actively transport out of the tissue by electrophoresis. Because the lipid bilayers are removed for more rigid and porous hydrogel network, the processed samples are easier for biochemical phenotyping, such as *in situ* hybridization and

immunohistochemistry. However, the entire procedure takes approximately 2 weeks and requires complicated preparation, including preparation of custom set-up for electrophoresis, which makes the CLARITY approach difficult to reproduce.

Recent progresses in tissue engineering and advances in light microscopy continuously generate a need for developing new methods to visualize and assess the tissue. Methods for imaging intact tissues rather than thin slices are more desirable. Being a stable and highly reproducible optical clearing method that is compatible with various fluorescent proteins, SeeDB is an ideal strategy for speedy examination of genetically labeled brain samples.

Table 6. Advantages and disadvantages of optical clearing agents, SeeDB, Sca*l*eA2, BABB (or dibenzyl ether), and CLARITY.

	SeeDB	**Sca*l*e**	**BABB, dibenzyl ether (DBE)**	**CLARITY**
Simplicity	+++	+++	+++	- (laborious preparation)
Transparency	++	++	+++	+++
Volume change	Constant	150% expansion	50% shrinkage	expansion
Preservation of morphology	+++	+	+	++ (transient expansion)
Agarose embedding	+++	-	-	+++ (hydrogel)
Sample solidity	soft	fragile	firm	soft
Speed of clearing	3 days	3 weeks (Sca*l*eA2) to 6 months (Sca*l*eU2)	2 to 5 days	2 weeks
Reversibility (for IHC)	+++	+	+	+++
Long-term storage	++	+++	++	++
Confocal microscopy	++	++	+++	++
Two-photon microscopy	+++	+++	+++	+++
Light-sheet microscopy	++	+	+++	+++
Fluorescent proteins	+++	++	+ (quenched within 1 day)	++
Fluorescent dextran dyes	+++	+++	+++	+++
Lipophilic dyes (DiI)	+++	-	-	-

-, impossible; +, difficult; ++, fair; +++, excellent.

4.2. Olfactory information integration in mitral cells

One of the important questions of neuroscience is to understand how neural circuits mediate perception and behavior. However, there is still a gap between circuits and behavior or even perception. In the mouse olfactory system, the precipitation of odor information starts from detection of odors by olfactory sensory neurons. Odor information is transferred from olfactory sensory neurons to mitral/tufted cells in the olfactory bulb. Mitral/tufted cells then send the information to the olfactory cortex.

'Sister' mitral cells get excited by a common glomerulus. Meanwhile, lateral inhibitions, mainly coming from granule cells, take a large part in managing the signal contrast in the olfactory bulb. Lateral inhibition is an important aspect in sensory information processing, where neurons receive inhibitory input from other neurons in the same population. Granule cells are located deep within the olfactory bulb forming reciprocal synapses with mitral/tufted cell and mediating feed forward and feedback inhibition on mitral/tufted cells. These networks can work to shape the sensory input and served as the initial site to integrate information of odor mixtures in the central olfactory system.

I used SeeDB to delineate olfactory bulb circuits at a single fiber resolution. With SeeDB method, I was able to construct a near-complete wiring diagram of mitral cells associated with a single glomerulus (**Figure 30** and **31**). Although odor information in a single glomerulus is relayed to multiple mitral cells, there is controversy regarding the extent to which odor information processing is conserved among the 'sister' mitral cells. In one scenario, 'sister' mitral cells may encode similar and redundant odor information and send parallel and robust outputs. For example, in *Drosophila*, sister projection neurons (equivalent to mammalian mitral cells) receive highly synchronous excitatory inputs and their axonal projection patterns are relatively stereotyped [70]. Similarly, in Xenopus, 'sister' mitral/tufted cells receive highly synchronous odor

inputs. In the rodent olfactory bulb, however, inhibitory neurons outnumber mitral cells by >100-fold [71,72]. Recent studies have demonstrated the variability in odor information coding among sister mitral cells [73,74].

From single glomerular tracer injection, I found that somata of sister mitral cells belonging to a common glomerular module were highly intermingled with those of surrounding glomeruli (**Figure 30**). Long lateral dendrites sparsely covered the olfactory bulb, consistent with reports from earlier tracing experiments and electrophysiological studies [61,62,68]. Furthermore, the pattern of lateral dendrites were not conserved among sister mitral cells (**Figure 31a**). Thus, lateral connectivity is not strictly center-surround, and 'sister' mitral cells are likely differentially tuned by inhibitory neurons, thereby encoding odor information in different temporal kinetics and tuning specificities. In addition, recent studies have shown that axonal projection patterns are also diverse among sister mitral cells, at least in the piriform cortex [64,65,66,75,76]. Thus, 'sister' mitral cells may send divergent odor information to different sets of target neurons in the olfactory cortex.

Deciphering odor coding strategy by a single glomerular module is an important ongoing issue in the olfactory system. Based on these topographical evidence, a non-redundant coding model in 'sister' mitral cells can be proposed (**Figure 32**). Lateral dendrites of 'sister' mitral cells are random and diverse. Each mitral cell receives broad and diverse lateral inhibition from surrounding granule cells. It is thought that lateral inhibition could increase the contrast between similar odors, even when the odors trigger nearly identical glomerular activation patterns, making it possible for animals to discriminate highly similar odors. Recent findings also suggests that in addition to identity or spatial codes, the relative timing of glomerular activation constitutes an important part of an odor code in the olfactory bulb [77,78,79,80].

5. References

1. Tsai PS, Friedman B, Ifarraguerri AI, Thompson BD, Lev-Ram V, et al. (2003) All-optical histology using ultrashort laser pulses. Neuron 39: 27-41.
2. Crosignani V, Dvornikov A, Aguilar JS, Stringari C, Edwards R, et al. (2012) Deep tissue fluorescence imaging and in vivo biological applications. Journal of Biomedical Optics 17: 116023-116023.
3. Helmchen F, Denk W (2005) Deep tissue two-photon microscopy. Nat Meth 2: 932-940.
4. Diaspro A, Bianchini P, Vicidomini G, Faretta M, Ramoino P, et al. (2006) Multi-photon excitation microscopy BioMedical Engineering OnLine 5: 36.
5. So PTC (2001) Two-photon Fluorescence Light Microscopy. eLS: John Wiley & Sons, Ltd.
6. Oheim M, Beaurepaire E, Chaigneau E, Mertz J, Charpak S (2001) Two-photon microscopy in brain tissue: parameters influencing the imaging depth. Journal of Neuroscience Methods 111: 29-37.
7. Tuchin V (2007) Tissue Optics: Light Scattering Methods and Instruments for Medical Diagnosis.
8. Steven LJ (2013) Optical properties of biological tissues: a review. Physics in Medicine and Biology 58: R37.
9. Theer P, Denk W (2006) On the fundamental imaging-depth limit in two-photon microscopy. Journal of the Optical Society of America A 23: 3139-3149.
10. Dingerkus GU, L.D. (1977) Enzyme clearing of alcian blue stained whole small vertebrates for demonstration of cartilage. Stain Technology 52: 4.
11. Klymkowsky MW, Hanken J (1991) Whole-mount staining of Xenopus and other vertebrates. Methods Cell Biol 36: 419-441.
12. Beuthan J, Minet O, Helfmann J, Herrig M, Müller G (1996) The spatial variation of the refractive index in biological cells. Physics in Medicine and Biology 41: 369.
13. Drezek R, Dunn A, Richards-Kortum R (1999) Light Scattering from Cells: Finite-Difference Time-Domain Simulations and Goniometric Measurements. Applied Optics 38: 3651-3661.
14. Johnsen S, Widder EA (1999) The physical basis of transparency in biological tissue: Ultrastructure and the minimization of light scattering. Journal of Theoretical Biology 199: 18.
15. Zhu D, Larin KV, Luo Q, Tuchin VV (2013) Recent progress in tissue optical clearing. Laser & Photonics Reviews 7: 732-757.
16. Genina EA, Bashkatov AN, Tuchin VV (2010) Tissue optical immersion clearing. Expert Review of Medical Devices 7: 825-842.
17. Dodt H-U, Leischner U, Schierloh A, Jahrling N, Mauch CP, et al. (2007)

Ultramicroscopy: three-dimensional visualization of neuronal networks in the whole mouse brain. Nat Meth 4: 331-336.
18. Becker K, Jahrling N, Saghafi S, Weiler R, Dodt HU (2012) Chemical clearing and dehydration of GFP expressing mouse brains. PLoS ONE 7: e33916.
19. Liu Y-C, Chiang A-S (2003) High-resolution confocal imaging and three-dimensional rendering. Methods 30: 86-93.
20. Lee P-C, Chuang C-C, Chiang A-S, Ching Y-T (2012) High-throughput Computer Method for 3D Neuronal Structure Reconstruction from the Image Stack of the Drosophila Brain and Its Applications. PLoS Comput Biol 8: e1002658.
21. Tseng Sj, Lin H-H, Tang S-C, Lin C-Y, Lee Y-H, et al. (2009) Integration of optical clearing and optical sectioning microscopy for three-dimensional imaging of natural biomaterial scaffolds in thin sections. Journal of Biomedical Optics 14: 044004-044004-044009.
22. Moy AJ, Wiersma MP, Choi B (2013) Optical Histology: A Method to Visualize Microvasculature in Thick Tissue Sections of Mouse Brain. PLoS ONE 8: e53753.
23. Hirshburg J, Choi B, Nelson JS, Yeh AT (2007) Correlation between collagen solubility and skin optical clearing using sugars. Lasers in Surgery and Medicine 39: 140-144.
24. Hirshburg JM, Ravikumar KM, Hwang W, Yeh AT (2010) Molecular basis for optical clearing of collagenous tissues. Journal of Biomedical Optics 15: 055002-055002-055008.
25. Wang J, Ma N, Shi R, Zhang Y, Yu T, et al. (2014) Sugar-Induced Skin Optical Clearing: From Molecular Dynamics Simulation to Experimental Demonstration. Selected Topics in Quantum Electronics, IEEE Journal of 20: 1-7.
26. Tsai PS, Kaufhold JP, Blinder P, Friedman B, Drew PJ, et al. (2009) Correlations of Neuronal and Microvascular Densities in Murine Cortex Revealed by Direct Counting and Colocalization of Nuclei and Vessels. The Journal of Neuroscience 29: 14553-14570.
27. Hama H, Kurokawa H, Kawano H, Ando R, Shimogori T, et al. (2011) Scale: a chemical approach for fluorescence imaging and reconstruction of transparent mouse brain. Nat Neurosci 14: 1481-1488.
28. Moulton K, Lay JDC, Jansen D, Willard S, Lovell F, et al. (2006) Use of glycerol as an optical clearing agent for enhancing photonic transference and detection of Salmonella typhimurium through porcine skin. Journal of Biomedical Optics 11: 054027-054027-054028.
29. Staudt T, Lang MC, Medda R, Engelhardt J, Hell SW (2007) 2,2′-Thiodiethanol: A new water soluble mounting medium for high resolution optical microscopy. Microscopy Research and Technique 70: 1-9.
30. Chung K, Deisseroth K (2013) CLARITY for mapping the nervous system. Nat

Meth 10: 508-513.
31. Chung K, Wallace J, Kim S-Y, Kalyanasundaram S, Andalman AS, et al. (2013) Structural and molecular interrogation of intact biological systems. Nature 497: 332-337.
32. Ertürk A, Becker K, Jährling N, Mauch CP, Hojer CD, et al. (2012) Three-dimensional imaging of solvent-cleared organs using 3DISCO. Nat Protocols 7: 1983-1995.
33. Cole RW, Jinadasa T, Brown CM (2011) Measuring and interpreting point spread functions to determine confocal microscope resolution and ensure quality control. Nat Protocols 6: 1929-1941.
34. Nagayama S, Zeng S, Xiong W, Fletcher ML, Masurkar AV, Davis DJ, Pieribone VA, Chen WR (2007) In vivo simultaneous tracing and Ca2+ imaging of local neuronal circuits. Neuron 53: 789-803.
35. Joyner A, Wall N (2008) Immunohistochemistry of Whole-Mount Mouse Embryos. Cold Spring Harbor Protocols 2008: pdb.prot4820.
36. Hendriks F, Aviram A (1982) Use of zinc iodide solutions in flow research. Review of Scientific Instruments 53: 75-78.
37. Mao Z, Zhu, D., Hu, Y., Wen, X., and Han, Z. (2008) Influence of alcohols on the optical clearing effect of skin in vitro. J Biomed Opt 13: 021104.
38. Lowe B (1937) Experimental cookery, from the chemical and physical standpoint. New York: J. Wiley & sons, inc.; London, Chapman & Hall, limited.
39. Maillard L-C (1912) Action des acides aminés sur les sucres: formation des mélanoïdines par voie méthodique. Journal de Physiologie 154: 3.
40. Dills Jr WL (1993) Protein fructosylation: fructose and the Maillard reaction. Am J Clin Nutr 58: 779S-787S.
41. Martins SIFS, Jongen WMF, van Boekel MAJS (2000) A review of Maillard reaction in food and implications to kinetic modelling. Trends in Food Science & Technology 11: 364-373.
42. Billaud C, Maraschin C Fau - Peyrat-Maillard MN, Peyrat-Maillard Mn Fau - Nicolas J, Nicolas J (2005) Maillard reaction products derived from thiol compounds as inhibitors of enzymatic browning of fruits and vegetables: the structure-activity relationship. Annals of the New York Academy of Sciences 6: 10.
43. McWeeny DJ, Biltcliffe DO, Powell RCT, Spark AA (1969) The Maillard Reaction and its Inhibition by Sulfite. Journal of Food Science 34: 641-643.
44. Godement P, Vanselow J, Thanos S, Bonhoeffer F (1987) A study in developing visual systems with a new method of staining neurones and their processes in fixed tissue. Development 101: 697-713.
45. Honig MG, Hume RI (1989) Dil and DiO: versatile fluorescent dyes for neuronal labelling and pathway tracing. Trends in Neurosciences 12: 333-341.
46. Neely MD, Stanwood GD, Deutch AY (2009) Combination of diOlistic labeling

with retrograde tract tracing and immunohistochemistry. Journal of Neuroscience Methods 184: 332-336.
47. Elberger AJ, Honig MG (1990) Double-labeling of tissue containing the carbocyanine dye DiI for immunocytochemistry. Journal of Histochemistry & Cytochemistry 38: 735-739.
48. Lukas J-R, Aigner M, Denk M, Heinzl H, Burian M, et al. (1998) Carbocyanine Postmortem Neuronal Tracing: Influence of Different Parameters on Tracing Distance and Combination with Immunocytochemistry. Journal of Histochemistry & Cytochemistry 46: 901-910.
49. Holmqvist BI, Ostholm T Fau - Ekstrom P, Ekstrom P (1992) DiI tracing in combination with immunocytochemistry for analysis of connectivities and chemoarchitectonics of specific neural systems in a teleost, the Atlantic salmon. J Neurosci Methods 42: 9.
50. Macdonald R (1999) Zebrafish Immunohistochemistry. Molecular Methods in Developmental Biology: Xenopus and Zebrafish, Springer. pp. 77-88.
51. Reihani SNS, Oddershede LB (2007) Optimizing immersion media refractive index improves optical trapping by compensating spherical aberrations. Optics Letters 32: 1998-2000.
52. Saito T (2006) In vivo electroporation in the embryonic mouse central nervous system. Nat Protoc 1: 1552-1558.
53. Tabata H, Nakajima K (2001) Efficient in utero gene transfer system to the developing mouse brain using electroporation: visualization of neuronal migration in the developing cortex. Neuroscience 103: 865-872.
54. Matsuda T, Cepko CL (2007) Controlled expression of transgenes introduced by in vivo electroporation. Proceedings of the National Academy of Sciences 104: 1027-1032.
55. Sanada K, Tsai L-H (2005) G Protein βγ Subunits and AGS3 Control Spindle Orientation and Asymmetric Cell Fate of Cerebral Cortical Progenitors. Cell 122: 119-131.
56. Imai T, Yamazaki T, KobayakawaR, Kobayakawa K, Abe T, Suzuki M, Sakano H (2009) Pre-target axon sorting establishes the neural map topography. Science 325: 585-590.
57. Schoppa NE, Westbrook GL (2001) Glomerulus-specific synchronization of mitral cells in the olfactory bulb. Neuron 31: 639-651.
58. Murthy VN (2011) Olfactory maps in the brain. Annu Rev Neurosci 34: 233-258.
59. Potter SM, Zheng C, Koos DS, Feinstein P, Fraser SE, Mombaerts P (2001) Structure and emergence of specific olfactory glomeruli in the mouse. J Neurosci 21: 9713-9723.
60. Feng G, Mellor RH, Bernstein M, Keller-Peck C, Nguyen QT, Wallace M, Nerbonne JM, Lichtman JW, Sanes JR (2000) Imaging neuronal subsets in transgenic mice expressing multiple spectral variants of GFP. Neuron 28:

41-51.
61. Orona E, Rainer EC, Scott JW (1984) Dendritic and axonal organization of mitral and tufted cells in the rat olfactory bulb. J Comp Neurol 226: 346-356.
62. Mori K, Kishi K, Ojima H (1983) Distribution of dendrites of mitral, displaced mitral, tufted, and granule cells in the rabbit olfactory bulb. J Comp Neurol 219: 339-355.
63. Igarashi KM, Ieki N, An M, Yamaguchi Y, Nagayama S, Kobayakawa K, Kobayakawa R, Tanifuji M, Sakano H, Chen WR, Mori K (2012) Parallel mitral and tufted cell pathways route distinct odor information to different targets in the olfactory cortex. J Neurosci 32: 7970-7985.
64. Ghosh S, Larson SD, Hefzi H, Marnoy Z, Cutforth T, Dokka K, Baldwin KK (2011) Sensory maps in the olfactory cortex defined by long-range viral tracing of single neurons. Nature 472: 217-220.
65. Sosulski DL, Bloom ML, Cutforth T, Axel R, Datta SR (2011) Distinct representations of olfactory information in different cortical centres. Nature 472: 213-216.
66. Nagayama S, Enerva A, Fletcher ML, Masurkar AV, Igarashi KM, Mori K, Chen WR (2010) Differential axonal projection of mitral and tufted cells in the mouse main olfactory system. Front Neural Circuits 4: 120.
67. Orona E, Scott JW, Rainer EC (1983) Different granule cell populations innervate superficial and deep regions of the external plexiform layer in rat olfactory bulb. J Comp Neurol 217: 227-237.
68. Kim DH, Phillips ME, Chang AY, Patel HK, Nguyen KT, Willhite DC (2011) Lateral connectivity in the olfactory bulb is sparse and segregated. Front Neural Circuits 5: 5.
69. Fantana AL, Soucy ER, Meister M (2008) Rat olfactory bulb mitral cells receive sparse glomerular inputs. Neuron 59: 802-814.
70. Kazama H, Wilson RI (2009) Origins of correlated activity in an olfactory circuit. Nat Neurosci 12: 1136-1144.
71. Kaplan MS, McNelly NA, Hinds JW (1985) Population dynamics of adult-formed granule neurons of the rat olfactory bulb. J Comp Neurol 239: 117-125.
72. Hinds JW, McNelly NA (1977) Aging of the rat olfactory bulb: growth and atrophy of constituent layers and changes in size and number of mitral cells. J Comp Neurol 72: 345-367.
73. Dhawale AK, Hagiwara A, Bhalla US, Murthy VN, Albeanu DF (2010) Non-redundant odor coding by sister mitral cells revealed by light addressable glomeruli in the mouse. Nat Neurosci 13: 1404-1412.
74. Kikuta S, Fletcher ML, Homma R, Yamasoba T, Nagayama S (2013) Odorant response properties of individual neurons in an olfactory glomerular module. Neuron 77: 1122-1135.
75. Miyasaka N, Morimoto K, Tsubokawa T, Higashijima S, Okamoto H, Yoshihara Y

(2009) From the olfactory bulb to higher brain centers: genetic visualization of secondary olfactory pathways in zebrafish. J Neurosci 29: 4756-4767.

76. Miyamichi K, Amat F, Moussavi F, Wang C, Wickersham I, Wall NR, Taniguchi H, Tasic B, Huang ZJ, He Z, Callaway EM, Horowitz MA, Luo L (2011) Cortical representations of olfactory input by trans-synaptic tracing. Nature 472: 191-196.
77. Haddad R, Lanjuin A, Madisen L, Zeng H, Murthy VN, et al. (2013) Olfactory cortical neurons read out a relative time code in the olfactory bulb. Nat Neurosci 16: 949-957.
78. Gerkin RC, Tripathy SJ, Urban NN (2013) Origins of correlated spiking in the mammalian olfactory bulb. Proceedings of the National Academy of Sciences 110: 17083-17088.
79. Gire DH, Restrepo D, Sejnowski TJ, Greer C, De Carlos JA, Lopez-Mascaraque L (2013) Temporal Processing in the Olfactory System: Can We See a Smell? Neuron 78: 416-432.
80. Zhou Z, Belluscio L (2012) Coding Odorant Concentration through Activation Timing between the Medial and Lateral Olfactory Bulb. Cell Reports 2: 1143-1150.

6. Acknowledgements

Numerous people over the years have helped me get here. Without them this thesis and my graduate career would not have been possible. My appreciation for everything they have done is immeasurable.

I would like to thank my advisor, Dr. Takeshi Imai, whose advice and support have helped me accomplish my goals in this research. My graduate career would not have been possible without the financial supports form Junior Research Associate (JRA) program in RIKEN. I would like to express the deepest appreciation to Dr. Fumio Matsuzaki for serving on my committee. In my daily work, I have been blessed with a friendly and cheerful group of people who have helped me through this experience. I have to give tremendous thanks to all of my partners. Thanks to Ryo, Satoshi, Eri, Miwako, Shuhei, and Marcus.

My deepest thanks go to my family for their tolerance and understanding.

This thesis is based on the following paper:

Meng-Tsen Ke, Satoshi Fujimoto, and Takeshi Imai
"SeeDB: a simple and morphology-preserving optical clearing agent for neuronal circuit reconstruction"
Nature Neuroscience, Volume 27, Issue 8, Page 1154-1161, 2013

Meng-Tsen Ke and Takeshi Imai
"Optical clearing of fixed brain samples using SeeDB"
Current Protocols in Neuroscience, Supplement 66: Page 2.22.1-2.22.19, 2014